Journal of Computational Physics 537 (2025) 114086

Contents lists available at ScienceDirect

Journal of Computational Physics

journal homepage: www.elsevier.com/locate/jcp

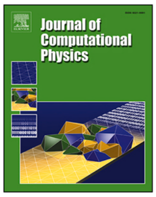

An efficient implicit scheme for the multimaterial Euler equations in Lagrangian coordinates

Simone Chiocchetti [a,b,c,*], Giovanni Russo [d]

[a] Division of Mathematics, University of Cologne, 86–90 Cologne, Weyertal, 50931, Germany
[b] Institute of Aerodynamics and Gasdynamics, University of Stuttgart, Pfaffenwaldring 21, Stuttgart, 70569, Germany
[c] Laboratory of Applied Mathematics, Department of Civil, Environmental and Mechanical Engineering, University of Trento, Via Mesiano 77, Trento, 38123, Italy
[d] Department of Mathematics and Informatics, University of Catania, Viale Andrea Doria, 6, Catania, 95125, Italy

ARTICLE INFO

Keywords:
Multimaterial Euler equations
Lagrangian coordinates
Implicit numerical methods
Multifluids
Stratified fluids

ABSTRACT

Stratified fluids composed of a sequence of alternate layers show interesting macroscopic properties, which may be quite different from those of the individual constituent fluids. On a macroscopic scale, such systems can be considered a sort of fluid metamaterial. In many cases each fluid layer can be described by Euler equations following the stiffened gas equation of state. The computation of detailed numerical solutions of such stratified material poses several challenges, first and foremost the issue of artificial smearing of material parameters across interface boundaries. Lagrangian schemes completely eliminate this issue, but at the cost of rather stringent time step restrictions. In this work we introduce an implicit numerical method for the multimaterial Euler equations in Lagrangian coordinates. The implicit discretization is aimed at bypassing the prohibitive time step restrictions present in flows with stratified media, where one of the materials is particularly dense, or rigid (or both). This is the case for flows of water-air mixtures, air-granular media, or similar high density ratio systems. We will present the novel discretisation approach, which makes extensive use of the remarkable structure of the governing equations in Lagrangian coordinates to find the solution by means of a single implicit discrete wave equation for the pressure field, yielding a symmetric positive definite structure and thus a particularly efficient algorithm. Additionally, we will introduce simple filtering strategies for counteracting the emergence of pressure or density oscillations typically encountered in multimaterial flows, and will present results concerning the robustness, accuracy, and performance of the proposed method, including applications to stratified media with high density and stiffness ratios.

1. Introduction

Motivation. Metamaterials have attracted an enormous attention in science and technology in the last two decades. They are composite materials obtained by assembling a large number of small unit cells, in 1D, 2D or 3D patterns, in such a way that on a length scale much larger than the cell size, they behave as a homogeneous material with properties that are different from the original constituent materials. In most cases, they exhibit properties that cannot be found in nature, and which are not even intermediate between the (mechanical or optical) properties of the constituents.

An enormous literature on metamaterials is available. Here we mention a couple of papers on acoustic metamaterials [1,2], which are a particular type of mechanical metamaterials. In these papers the authors emphasize the remarkable properties and the

---

[*] Corresponding author.
E-mail address: simone.chiocchetti@unitn.it (S. Chiocchetti).

https://doi.org/10.1016/j.jcp.2025.114086
Received 9 October 2024; Received in revised form 30 April 2025; Accepted 12 May 2025

anomalous behaviour of such materials. Among the surprising properties of acoustic metamaterials, we recall the so-called *negative mass*. This means that the system behaves like a peculiar mass-spring system which, if excited with a periodic external forcing term with a suitable frequency, shows a displacement which is in phase with the force, rather than in phase opposition, as one would expect [3]. In [4] it is shown how to create a simple 1D acoustic metamaterial formed by a gas tube, with compartments separated by elastic membranes.

The analysis of the properties of acoustic metamaterials is in general based on linear or linearized equations, so that it is assumed that the displacement, or any type of signal, is sufficiently small so that linear theory can be used, or that non-linear effects can be computed by perturbation methods, still assuming sufficiently small signals. We also point out that fully nonlinear innovative theories of metamaterials are object of current research, see for example [5].

There are several cases in which non-linear effects are crucial and cannot be neglected. In a multilayer system formed by several pairs of layers of two different fluids, for example, the non-linear response of the gases cannot be neglected, and shocks will in general form and propagate in the multilayer medium, unless the initial state or the forcing terms are suitably small, or the periodicity of the system indices an oscillator behaviour of the solutions, as it has been recently observed in several quasilinear hyperbolic systems when the waves propagates over a periodic medium, as in the case of non linear elasticity in 1D [6] and in 2D [7] or shallow water over periodic bathymetry in 1D [8] or in 2D [9]. In all these cases, the amplitude of the wave is large enough to observe non-linear effects, still sufficiently small to avoid formation of shock waves. For large amplitude waves propagating on layered media, shocks will generally form.

In [10], for example, the behaviour of a large number of pairs of layers is studied numerically. Each pair is formed by two different fluids, each one treated as a stiffened gas with its own standard density ρ, adiabatic exponent γ, and a constant Π which determines the stiffness of the fluid, and which is sometimes called attractive pressure[11].

In the paper it is shown that the a simple adiabatic homogeneous model is able to accurately reproduce the behaviour of the multilayer system provided isentropic initial conditions are assigned, and the integration time is short enough (or equivalently the deviation from global equilibrium is small enough) so that no strong shocks form. When shocks form, the predictions of the homogeneous model are no longer reliable, hence the use of a more accurate model is necessary.

Another interesting feature of the multilayer system is that, depending on the fluid parameters, the effective sound speed of the homogenised fluid may be a non monotonic function of the mass fraction of the layers. As a result, the effective sound speed of the layer may be smaller than the sound speed of both gases.

The connection itself of homogenised multiphase flow models to the detailed description of multilayered systems with sharp interfaces coupling two or more fluids governed by the compressible Euler or Navier–Stokes equations is an additional point of interest. For example, Bresch, Burtea and Lagoutière [12,13] discuss the link between such layered systems and multiphase flow models of Baer–Nunziato type. They provide formal proof, starting from a layered two-fluid system governed by the compressible Navier–Stokes equations (which give no-slip coupling conditions between interface velocities), and from a semi-discrete description of the same system, that homogenisation will yield a viscous, compressible, single-velocity, two-pressure multiphase model of the Baer–Nunziato [14] flavour (with single velocity and two pressures as in Richard Saurel et al. [15], Pelanti and Shyue [16]). They also formally recover Kapila's inviscid single-velocity, single-pressure model [17] in the limit of vanishing viscosity. In this regard, in this paper we limit our scope to providing experimental evidence of the latter remark that multilayer systems governed by the compressible Euler equations yield a homogenised behaviour that is captured at a coarse level by Kapila's model. The strategy used here is just incidental: homogenisation effects are observed/captured by the scheme automatically, when space and time are under-resolved with respect to the natural fast/small scales of the detailed Euler–Euler flow. Tackling multiphase flows starting from the detailed description of the underlying two-fluid system was also the strategy adopted by Petrella et al. [18], where the closure problem of multiphase flow models is avoided entirely by carrying out a set of front tracking simulations, embedded in a Monte Carlo loop, which yields solutions of the homogenised model as a result of the accumulated statistics. Like in this paper, the authors adopted a sharp description of material fronts, even if afterwards smoothing is obtained via the Monte Carlo averaging. Similarly, here we capture material interfaces sharply and then we can simply under-resolve the timestepping to compare with the solutions of the homogenised models.

Numerical methodology. In [10] the detailed numerical solution of the multilayer system was obtained by a finite volume methods for solving the Euler equations that describe the fluids expressed in Lagrangian form, where the mass coordinate and time are adopted as independent variables. This choice appears to be a natural one, since it allows to have material boundaries between the two fluids always located at cell edges, so strictly speaking in this configuration there is no need to use a diffuse interface multiphase model, such as for example Kapila's [17] reduced Baer–Nunziato family model [14–16], or [19–24], and each cell completely belongs to either the first or the second fluid. A positive side effect of such a separation is that very sharp material interfaces and contacts are naturally obtained, directly at cell interfaces (which is very convenient in one space dimension) or from a level set function [25] in the more general case. Furthermore, working with "pure" states makes it simpler to perform reconstructions and to design exact or approximate Riemann solvers. As mentioned, versatile diffuse interface treatments for this problem have shown promising results for solid-fluid interfaces [26,27] and the treatment of free surfaces [28–30].

Explicit schemes for the numerical solution of fluid equations suffer from classical Courant-Friedrichs-Lewy time step restriction [31], which can be written as $\Delta t < C\Delta\xi/\lambda$, where λ denotes the maximum characteristic speed of the system in the computational domain, C is a constant of order of magnitude 1, and $\Delta\xi$ denotes the discretization of the independent space coordinate (which is typically space x in Eulerian coordinates and mass coordinate m in the Lagrangian framework). The ability of constructing versatile and efficient high order massively parallel codes [32,33] is however a very attractive feature of such schemes.

Explicit integration also is sensitive, in Lagrangian an arbitrary Lagrangian–Eulerian [34–39], or [40–42], to the formation of small cells that yield very stringent timestep restrictions, though this can be mitigated, for example, by using local timestepping methods [40].

If sound speed in one of the two materials is much larger than in the other, say $\lambda_1 \gg \lambda_2$, then the most severe time restriction on the time step will be due to the waves propagating in fluid 1. On the other hand, we expect that the faster material behaves almost like an incompressible fluid compared to the other, therefore most of the effect of compressibility will be evident in the softer fluid, for which stability and accuracy requirements on the time step will be similar. For such a reason the system becomes *stiff*: stability requirements on the time step in the first fluid are much more restrictive than accuracy requirements.

Some correction strategies for explicit methods, made to deal with inaccuracies encountered by such schemes in the low-Mach regime, are also available [43–45], but it would seem that an implicit or semi-implicit strategy is required to deal with excessive timestep restrictions characteristic of low Mach number flows. In general, the use of some implicitness may mitigate the stiffness problem, thus improving the overall efficiency of the scheme.

An extreme case of multifluid in which the densities and stiffness of the two fluids are very different is a multilayer formed by a sequence of air and water layers. Here the ratio of the densities is close to one thousand, while the ratio in the sound speed, in standard Eulerian coordinates, is approximately four (see Section 2.1). In [10] only explicit schemes with locally uniform spacing in the mass Lagrangian coordinate have been adopted. The ratio of the sound speed between the two fluids in Lagrangian coordinates is equal to the Eulerian one multiplied by the ratio in the density, which causes the ratio of Lagrangian sound speed between water and air to be more than three thousand, making it almost unfeasible to adopt an explicit scheme in Lagrangian coordinates with uniform mesh for the numerical treatment of water-air multilayer systems. For this reason in Phan et al. [10] the authors considered only a moderate density ratio (either 2 or 10 in particular).

A semi-implicit approach would indeed be a very natural choice for an efficient implicit FV scheme: solving convection explicitly and treating acoustic waves implicitly, recovering pressure and momentum, allows to construct very simple and efficient numerical discretizations [46–48]. This approach has been widely adopted in the Eulerian framework to construct the so called all-Mach number solvers for compressible Euler equations (see for example Degond and Tang [49], Cordier et al. [50] for one of the first second order finite volume all Mach solvers for isentropic equations, Boscarino et al. [51] for a second order finite volume all-Mach solver for full Euler equations on staggered grid, or Avgerinos et al. [52] for a second order FV full Euler all-Mach solver on unstaggered grid.) Second order accurate all Mach solvers for full 3D Euler equations have been constructed and tested in Boscheri et al. [53], while third order finite difference all Mach solvers for Euler equations have been developed in Boscarino et al. [54] for isentropic Euler equations, and in Boscarino et al. [55] for full Euler equations. Using staggered grids, similar all-speed methods have been developed also in a hybrid Finite Volume-Finite Element framework [56]. Finally, an all-Mach solver for isentropic two phase flows has been developed in Lukáčová-Medvid'ová et al. [57] (see also Lukáčová-Medvid'ová et al. [58]).

A common feature of all such solvers is that only the fast waves are treated implicitly, and in most cases only linearly implicit, i.e. the implicit solver is applied to a linearization of the equations. High order in time is usually achieved using Implicit-Explicit time solvers, such as Runge-Kutta IMEX (see, for example Ascher et al. [59], or Pareschi and Russo [60]). A general technique to obtain high order accuracy when the system containing stiff and non-stiff terms is not written in additive nor in partitioned for is introduced in Boscarino et al. [61], and adopted, for example, in Boscarino et al. [54] and Boscarino et al. [55]. It is worth noting that the versatility of such non-partitioned IMEX schemes allows their use in complex frameworks like in Boscheri et al. [62], where IMEX integration is used in conjunction with a black box solver derived from Chiocchetti and Müller [63].

Semi-implicit schemes have the advantage of being usually more efficient than fully implicit ones, for the same required accuracy. Nevertheless, very efficient implicit methods like [64] are available, and implicit methods for fluid flow, even of Finite Volume type [65] are currently being actively developed in the literature.

Moreover, semi-implicit schemes tend to be less stable, and have been found to be more prone to spurious oscillations (see, for example, Boscarino et al. [66], where semi-implicit and fully implicit solvers are compared for a class of convection-diffusion problems). Nevertheless, a vast amount of successful schemes for low Mach and all Mach flows have been constructed with this methodology, and in particular [48], which provided the main guidelines for the efficient formulation here introduced.

In this work, we instead aim at constructing a fully-implicit method along the steps of the recent work by Plessier et al. [67] (see also Pino et al. [68]), which is the main motivation for the present paper, with a different discretization strategy that leverages the structure of the governing equations to build an efficient method that resembles a Lagrangian adaptation of the scheme by Dumbser and Casulli [48]. Additionally, here we introduce several strategies for controlling spurious oscillations arising in the solution of two-material compressible flows and apply the new scheme to multi-layer systems following the work by Phan et al. [10], where explicit numerical methods were used.

The system of Euler equations for stiffened gas in Lagrangian coordinates offers a very natural opportunity for distilling a single scalar discrete wave equation for the pressure field, which can be solved iteratively by a sequence of tridiagonal systems (predictor), leading to a preliminary (possibly oscillatory and non conservative) solution which can be made conservative and non-oscillatory with a suitable post-processing (corrector). Once a first order scheme is produced, singly-diagonally-implicit Runge–Kutta (SDIRK) schemes can be adopted to rise time accuracy to second or higher order. An additional advantage of the approach is that it does not require sophisticated Riemann solvers to reproduce sharp contact and material interfaces.

The method naturally generalizes to the treatment of layered multifluid, for which, as we already mentioned, the Lagrangian approach avoids the use of intermediate states. When dealing with material interfaces, the methods blends the use of conservative and primitive variables in the time advancement of the solution, using ideas from Abgrall and Karni [69]. Strict conservation is locally lost, yet, the shock speed is correctly captured up to the accuracy of the method (see Section 5.1).

Last, but not least, a whole section (Section 4) is devoted to the construction of quasi-uniform grids, i.e. grids in the Lagrangian mass variable whose spacing varies smoothly among cells. This avoids the drawbacks of uniform cells when dealing with fluids with large mass density ratio: using uniform cells in the mass variable under-resolve the regions occupied by the low density fluid, or over-resolves the regions occupied by the high density fluid. On the other hand, using grid spacing which is approximately uniform in space causes an abrupt jump in the grid spacing in the mass variable, which may induce oscillations and sometimes unphysical solutions.

The plan of the paper is the following. After the introduction, Section 2 describes the model under consideration, i.e. Euler system for a stiffened gas in Lagrangian coordinates. Section 3 is the core of the paper and describes in detail the construction of the method as outlined in the previous paragraphs (non-conservative, possibly oscillatory, fully implicit predictor, conservative non-oscillatory corrector). Section 4 deals with the construction of mass conservative well-graded Lagrangian meshes. Section 5 is devoted to illustrate the performance of the method on a sequence of classical tests for a single gas and for a multilayer systems.

In particular, Section 5.5 is dedicated to applications to systems with many stratified layers, and compares and contrast the behaviour of the scheme with that obtained from the a homogenized multiphase model. Finally, in Section 6 we draw some conclusions and perspective about applications and extensions of the method.

2. Governing equations

We consider the one-dimensional Euler equations in Lagrangian (mass) coordinates. The spatial mass abscissa m (also referred to as Lagrangian abscissa in this manuscript) is defined at a point x (in this manuscript also called Eulerian coordinate) as the mass of the fluid (per unit area) found between the left boundary ($m = 0$) and the Eulerian coordinate x, or formally

$$m(x) = \int_{x_\mathrm{L}}^{x} \rho(x')\,\mathrm{d}x', \tag{1}$$

where ρ is the mass density of the fluid. Symmetrically, the Eulerian coordinate x can be recovered from the mass coordinate as

$$x(m) = \int_{0}^{m} V(m')\mathrm{d}m', \tag{2}$$

with $V = 1/\rho$ the specific volume of the fluid.

In the Lagrangian mass coordinate system, the conservation laws for mass, momentum, and energy read

$$\partial_t(V) + \partial_m(-u) = 0, \tag{3a}$$

$$\partial_t(u) + \partial_m(p) = 0, \tag{3b}$$

$$\partial_t(E) + \partial_m(u\,p) = 0, \tag{3c}$$

$$\partial_t(c) = 0, \tag{3d}$$

where we define $V = V(t,\ m)$ to be the specific volume of the fluid (the reciprocal of the mass density ρ), the velocity field is $u = u(t,\ m)$, and $E(t,\ m) = e_\mathrm{k} + e$ is the specific total energy density. The system is closed with the definition of the specific kinetic energy $e_\mathrm{k} = u^2/2$ and by providing an equation of state (EOS) that expresses the internal energy e as a function of density (or specific volume) and pressure. In this work we adopt the stiffened gas equation of state in the form

$$e = V\,\frac{p + \gamma\,\Pi}{\gamma - 1}. \tag{4}$$

Note that, since we allow the presence of two separate (immiscible) fluids, the local adiabatic index γ and the stiffness parameter Π may vary between two values γ_1 and γ_2, and Π_1 and Π_2. Owing to the immiscible nature of the modelled fluids (which is maintained also at the discrete level), there is no necessity for mixture rules defining homogenised or averaged parameters at interfaces. Nevertheless, as a piece of notational convenience, we can define a colour function c which helps tracking the presence of one or the other fluid at a given Lagrangian location. The value of c is initially assigned cell-by-cell in as either $c = 1$ (meaning only fluid 1 is present) or $c = 0$ (only fluid 2 is present). This means that the parameters of the equation of state can be locally recovered by computing $\gamma = c\,\gamma_1 + (1-c)\,\gamma_2$ and $\Pi = c\,\Pi_1 + (1-c)\,\Pi_2$. We should emphasize that such a notation is *not* a mixture rule (or at least not a good one) but rather a shorthand which is valid in this context only thanks to the fact that c is allowed only to be valued *exactly* $c = 0$ or *exactly* $c = 1$. Moreover, in Lagrangian coordinates, Eq. (3d) is not discretised at all, since it simply states that the EOS parameters are immutably associated with each discrete cell.

See [69] for a discussion of computationally favourable choices for averaged equation of state parameters.

2.1. Characteristic speeds in Lagrangian coordinates

We briefly discuss the eigenvalues of the hyperbolic system of PDEs (3a)–(3c), in regards to the CFL timestep restriction [31] they obey to when explicit timestepping is adopted. Having defined a vector of conserved variables $\mathbf{Q} = (V,\ u,\ E)^\mathsf{T}$, and a flux vector $\mathbf{F} = (-u,\ p,\ u\,p)^\mathsf{T}$, the system of conservation laws (3a)–(3c) can be cast as

$$\partial_t\mathbf{Q} + \partial_m\mathbf{F} = \mathbf{0}, \tag{5}$$

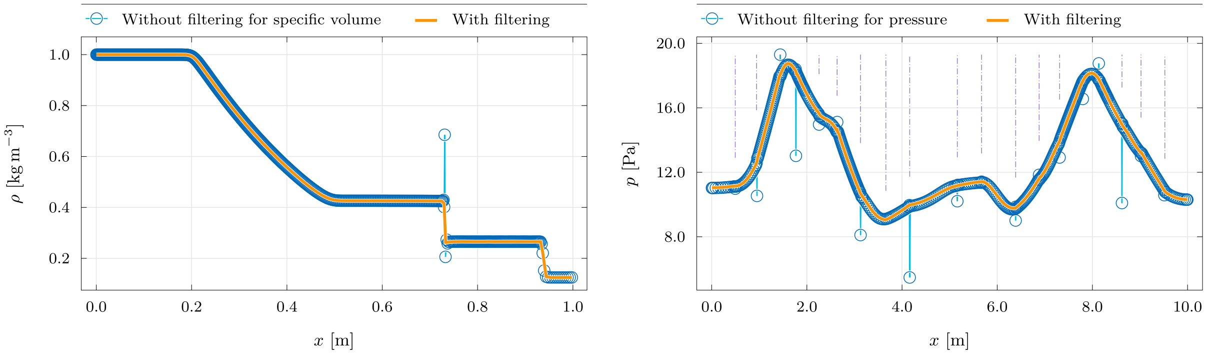

Fig. 1. Motivation for the filtering techniques introduced in this work. On the left: central fluxes for the density update introduce spurious oscillations in correspondence of contact discontinuities. The oscillations are eliminated by numerical diffusion-like filtering (Section 3.2.3). On the right: pressure oscillations appear at material interfaces, across which the parameters of the equation of state are discontinuous (the interface positions are highlighted with dashed lines). The oscillations disappear with filtering (Section 3.2.5). Both simulations were run with SDIRK2 time-stepping and $N = 1000$ cells. For the left panel $k_{\mathrm{CFL}} = 5.0$ and for the right panel $k_{\mathrm{CFL}} = 1000$.

or, in terms of the primitive variables $\mathbf{W} = (V,\ u,\ p)^{\mathsf{T}}$ and in its so-called quasi-linear form

$$\partial_t \mathbf{W} + \mathbf{A}\,\partial_m \mathbf{W} = \mathbf{0}, \quad \text{with} \quad \mathbf{A} = \left(\frac{\partial \mathbf{Q}}{\partial \mathbf{W}}\right)^{-1} \left(\frac{\partial \mathbf{F}}{\partial \mathbf{W}}\right). \tag{6}$$

The system matrix is

$$\mathbf{A} = \begin{pmatrix} 0 & -1 & 0 \\ 0 & 0 & 1 \\ 0 & a^2 & 0 \end{pmatrix}, \quad \text{with} \quad a^2 = \left(\frac{\partial e}{\partial p}\right)^{-1} \left(\frac{\partial e}{\partial V} + p\right) = \frac{\gamma\,(p+\Pi)}{V} = \rho\,\gamma\,(p+\Pi) \tag{7}$$

and has eigenvalues $\boldsymbol{\lambda} = (-a,\ 0,\ a)^{\mathsf{T}}$. Crucially, in mass coordinates, the square of the acoustic eigenvalues of the system are proportional to the mass density ρ. Since for explicit schemes the maximum stable timestep [31] is inversely proportional to the magnitude of the eigenvalues, such a dependence on ρ implies that denser fluids will be more restrictive than lighter ones with regards to the maximum admissible timestep of explicit methods, if we assume a uniform mesh in the mass variable. In contrast, the same analysis, when carried out for the Eulerian variant of the governing equations, would yield $\lambda_{\mathrm{E}} = \left(u - a_{\mathrm{E}},\ u,\ u + a_{\mathrm{E}}\right)^{\mathsf{T}}$, with $a_{\mathrm{E}}^2 = \gamma\,(p+\Pi)/\rho$, meaning that in the Eulerian framework denser fluids admit larger timesteps for a fixed choice of the EOS parameters γ and Π, assuming uniform mesh in the space variable.

Oftentimes, in simulations involving both a non-stiff fluid and a stiff one, (an example might be air and water), the fluid characterised by higher values of γ and Π (that is, the stiff one), is also the denser of the two. In the following paragraphs, we give a practical quantitative illustration of the discrepancy: at standard atmospheric conditions $p = 10^5\,\mathrm{Pa}$, $\gamma_{\mathrm{a}} = 1.4$, $\Pi_{\mathrm{a}} = 0\,\mathrm{Pa}$, $\rho_{\mathrm{a}} = 1.2\,\mathrm{kg\,m^{-3}}$, an estimate for the speed of sound is $a_{\mathrm{E}}^{\mathrm{a}} \simeq 341.6\,\mathrm{m\,s^{-1}}$, while at the same pressure the speed of sound for water can be estimated to be $a_{\mathrm{E}}^{\mathrm{w}} \simeq 1482.3\,\mathrm{m\,s^{-1}}$, with $\gamma_{\mathrm{w}} = 7.3$, $\Pi_{\mathrm{w}} = 3.0 \times 10^8\,\mathrm{Pa}$, $\rho_{\mathrm{a}} = 997\,\mathrm{kg\,m^{-3}}$. The same choice of material parameters, when adopted in the Lagrangian framework, yields $a^{\mathrm{a}} \simeq 409.9\,\mathrm{kg\,m^{-2}\,s^{-1}}$ and $a^{\mathrm{w}} \simeq 1.478 \times 10^6\,\mathrm{kg\,m^{-2}\,s^{-1}}$ (the units change due to the fact that the spatial coordinate x is replaced by the mass coordinate m), meaning that in mass coordinates the water phase imposes a timestep more than 3600 times smaller than the one allowed by the air on the same mesh spacing, as opposed to the ratio being about 4.3 in the Eulerian setting.

Of course the physical speed of sound waves remains the same in both cases, but from the computational standpoint, the timestep size of explicit Lagrangian schemes using mass coordinates is restricted by a much higher numerical signal speed.

3. Numerical method

In this Section we present the scheme here developed and used, which is based on a Lagrangian staggered grid in mass coordinates, and makes use of a predictor step involving a smooth wave-equation discretisation (see Section 3.2.1), with a finite difference type correction step. To manage spurious oscillations that may be generated as a result of these low-dissipation discretisation choices (Lagrangian coordinates, smooth predictor step, central differences), we also introduce ad hoc filtering techniques that have been embedded in the iterative computation of the solution. These target oscillations of specific volume in Section 3.2.3 and oscillations of pressure in Section 3.2.5. Leaving such spurious oscillations unchecked might lead to catastrophic failure of the computations when strong shockwaves are encountered, due to violation of positivity in the pressure and in the specific volume, hence implementation of some form of oscillation control is crucial to the robustness of the scheme. Fig. 1 provides some visual examples of how spurious oscillations might manifest even in mild problems, due to the intrinsic low dissipation at material interfaces given by the Lagrangian framework, as well as due to the presence of non-homogeneous material interfaces. The reader is referred to the paper by Abgrall and Karni [69] for an extensive discussion of these issues in multifluid computation.

3.1. Staggered grid

The scheme developed in this work adopts a staggered grid, mainly with the goal of obtaining a well-behaved and inexpensive discretisation for a wave equation yielding a preliminary solution for the pressure field, whereby the pressure field p_i, the specific volume V_i and the specific total energy E_i can be seen as collocated at cell centers, (the conserved quantities can equivalently be interpreted as cell average values), and the velocity field $u_{i+1/2}$ is collocated at cell interfaces. The left boundary is denoted with the Eulerian coordinate x_{L}, and by definition the corresponding mass coordinate is $m(x_{\mathrm{L}}) = 0$, while the right boundary is x_{R}, and $m(x_{\mathrm{R}}) = m_{\mathrm{tot}}$ is the total mass of the system.

The computational domain is partitioned using a staggered grid. The main grid is composed of N cells of index $i = 1, 2, \ldots, N$, having variable width Δx_i or mass content Δm_i. The cell boundaries are formally denoted $m_{i+1/2}$ regardless of the uniformity of the grid, and define a face-based dual grid, which is used for collocation of the velocity field u. For notational convenience, we define at each cell boundary the mesh spacing for the dual grid as $\Delta m_{i+1/2} = \left(\Delta m_i + \Delta m_{i+1}\right)/2$, which corresponds to the distance between the cell centers of the two adjacent control volumes.

3.2. Discretisation approach

3.2.1. Wave equation

The combination of the governing Eqs. (3a)–(3c) into a single wave equation constitutes the core of the numerical method proposed in this work. Although the derivation of such a wave equation is a trivial exercise, we carry out here the main steps in order to clarify the scope of applicability of the proposed framework.

An important preliminary note is that the employed wave equation relies on the validity of the strong form of the governing equations, implying that density, velocity, and pressure, should be smooth fields, rather than discontinuous as they will instead be in practice. Nonetheless, it will be shown with numerical examples that this fact does not hinder the applicability of the numerical method here presented.

Further corrections to the discretisation scheme, accounting for the restricted validity of this assumption will be detailed in the subsequent paragraphs.

The derivation begins by applying the chain rule to Eq. (3c) to obtain

$$\partial_t\left(e + u^2/2\right) + \partial_m(up) = \frac{\partial e}{\partial p}\,\partial_t p + \frac{\partial e}{\partial V}\,\partial_t V + u\,\partial_t u + u\,\partial_m p + p\,\partial_m u = 0, \tag{8}$$

which, due to the momentum Eq. (3b) simplifies to

$$\frac{\partial e}{\partial p}\,\partial_t p + \frac{\partial e}{\partial V}\,\partial_t V + p\,\partial_m u = 0. \tag{9}$$

Inserting the mass Eq. (3a) into (9), and making use of Eq. (7), after simple algebraic rearrangement, the wave equation reads

$$\partial_t p + a^2\,\partial_m u = 0. \tag{10}$$

In the case of the stiffened gas EOS (4), the explicit expressions of the partial derivatives of the internal energy are

$$\frac{\partial e}{\partial p} = \frac{V}{\gamma - 1}, \qquad \frac{\partial e}{\partial V} = \frac{p + \gamma\,\Pi}{\gamma - 1} \tag{11}$$

and thus the wavespeed is $a = \sqrt{\gamma\,(p + \Pi)/V}$. Thanks to the Lagrangian coordinates, the wave equation assumes the very simple form (10) and, most important, it does not feature any nonlinear convective terms, which would be present in its Eulerian analogue.

3.2.2. Discrete wave equation

The continuous wave Eq. (10) can be used as the basis for the construction of a *discrete* system of algebraic equations which can be solved rather efficiently as a sequence of implicit linear problems for the pressure field only.

Discrete values p_i^n, p_i^{n+1} (cell i, time level $t = t^n$ and $t = t^{n+1}$ respectively) for the pressure field are collocated at the cell centers of the main grid ($m = m_i$). Consequently a rather natural finite-difference discretisation of (10) is

$$\frac{p_i^{n+1} - p_i^n}{\Delta t} + \left(a^2\right)_i^{n+1}\,\frac{u_{i+1/2}^{n+1} - u_{i-1/2}^{n+1}}{\Delta m_i} = 0. \tag{12}$$

We remark that conveniently the computation of the wavespeed $\left(a^2\right)_i^{n+1}$ is required *only* at cell centers, where the discrete pressure field is directly collocated, requiring no interpolation of pressure or internal energy, and guaranteeing that no artificial mixture-states have to be generated, as would be the case if a^2 had to be evaluated at cell interfaces. This is a welcome feature since simple averaging rules might generate non-physical, highly inaccurate, or oscillatory results (see for example Abgrall and Karni [69]).

Following the strategy used for the fully discrete semi-implicit methodology introduced in Dumbser and Casulli [48], we introduce a finite difference discretisation for the velocity field update at the grid interface location

$$u_{i+1/2}^{n+1} = u_{i+1/2}^n - \frac{\Delta t}{\Delta m_{i+1/2}}\left(p_{i+1}^{n+1} - p_{i-1}^{n+1}\right), \tag{13}$$

which can then be inserted in (12) giving

$$\frac{p_i^{n+1}-p_i^n}{\Delta t}+\frac{(a^2)_i^{n+1}}{\Delta m_i}\left[u_{i+1/2}^n-\frac{\Delta t}{\Delta m_{i+1/2}}\left(p_{i+1}^{n+1}-p_i^{n+1}\right)-u_{i-1/2}^n+\frac{\Delta t}{\Delta m_{i-1/2}}\left(p_i^{n+1}-p_{i-1}^{n+1}\right)\right]=0, \tag{14}$$

The nonlinear system of algebraic equations (14) for p^{n+1} is solved via a simple fixed point iteration which generates a sequence of approximations $\widetilde{(a^2)}_i^{n+1,r}=a^2(V_i^{n+1,r-1},\ p_i^{n+1,r-1})$ for the values of the nonlinear function $a^2(V,\ p)$, converging towards the value at the new time level $(a^2)_i^{n+1}=a^2(V_i^{n+1},\ p_i^{n+1})$.

As an initial guess for the first iteration $r=1$, we use the pressure at the previous time level $p_i^{n+1,0}=p_i^n$, while the specific volume is obtained as

$$V_i^{n+1,0}=V_i^n-\frac{\Delta t}{\Delta m_i}\left(f_{i+1/2}^V-f_{i-1/2}^V\right), \tag{15}$$

with the numerical flux $f_{i+1/2}^V$ given by be the simple Rusanov [70] approximate Riemann solver (with mild, flow velocity-based, signal speed estimates) as

$$f_{i+1/2}^V=\frac{1}{2}\left(-u_i-u_{i+1}\right)-\frac{1}{2}\max\left(\rho_i\left|u_i\right|,\ \rho_{i+1}\left|u_{i+1}\right|\right)\left(V_{i+1}-V_i\right). \tag{16}$$

The scheme is not particularly sensitive to this initial guess, as evidenced by the fact that the sharp contact discontinuities typical of Lagrangian schemes employing complete Riemann solvers are recovered by the proposed scheme despite not using such contact-resolving Riemann solvers at all. Simpler initial guesses, such as $V_i^{n+1,0}=V_i^n$ can be considered, with no effect on the accuracy or robustness of the scheme. The one given in (16) is the one used for all tests included in this paper, out of an abundance of caution, but no solid arguments for why it should be preferred to simpler (or trivial) initial guesses have been found in this work.

The linear system presents a tridiagonal structure

$$k_{i-1}\,p_{i-1}^{n+1}+k_i\,p_i^{n+1}+k_{i+1}\,p_{i+1}^{n+1}=b_i \tag{17}$$

with the coefficients being

$$\begin{aligned}
k_{i-1}&=-\widetilde{(a^2)}_i^{n+1}\frac{\Delta t}{\Delta m_i}\frac{\Delta t}{\Delta m_{i-1/2}},\\
k_i&=1+\widetilde{(a^2)}_i^{n+1}\frac{\Delta t}{\Delta m_i}\left(\frac{\Delta t}{\Delta m_{i-1/2}}+\frac{\Delta t}{\Delta m_{i+1/2}}\right),\\
k_{i+1}&=-\widetilde{(a^2)}_i^{n+1}\frac{\Delta t}{\Delta m_i}\frac{\Delta t}{\Delta m_{i+1/2}},
\end{aligned} \tag{18}$$

and the known right hand side

$$b_i=p_i^n-\widetilde{(a^2)}_i^{n+1}\frac{\Delta t}{\Delta m_i}\left(u_{i+1/2}^n-u_{i-1/2}^n\right), \tag{19}$$

where the iteration index r for the pressure $p_i^{n+1,r}$ and the wavespeed $\widetilde{(a^2)}_i^{n+1,r}$ have been omitted for the sake of brevity.

As soon as the discrete pressure field p_i^{n+1} at cell centers is recovered by solving the linear system (17), the velocity at the cell boundary $u_{i+1/2}^{n+1}$ can also immediately be computed using the central difference (13), and subsequently the specific volume is updated in an analogous manner

$$(V_i^{n+1})_{\mathrm{c}}=V_i^n-\frac{\Delta t}{\Delta m_i}\left(-u_{i+1/2}+u_{i-1/2}\right). \tag{20}$$

The quantity given by (20) is denoted $(V_i^{n+1})_{\mathrm{c}}$ to indicate that it is obtained from the direct discretisation of the PDE via a conservative update formula, based on a staggered central difference. The updated value of the specific volume V_i^{n+1} is computed after having found a suitable set of diffusive fluxes, in order to introduce numerical dissipation and control the oscillations generated by the central update formula. The determination of such fluxes is detailed in the next subsection.

Noted that the state variables have to be updated at each iteration in a rather nonlinear manner, inclusive of numerical stabilisation via diffusion and data-dependent filtering. The iteration loop is split into two nested parts: a first one (an inner loop) in which a solution for $(V_i^{n+1})_{\mathrm{c}}$, $u_{i+1/2}^{n+1}$, and p_i^{n+1} is sought, that is, the solution of the discrete wave Eq. (14) *per se*, and a second one (an outer loop) which begins with running to convergence an instance of the inner loop and subsequently applies diffusion and filtering operators to the discrete volume and pressure. The final result of the outer loop consists of the conservative state vector composed of V_i^{n+1}, $u_{i+1/2}^{n+1}$, and E_i^{n+1}. For each of the two loops, the iteration is stopped as soon as the difference between two successive updates falls below a prescribed tolerance.

The discretisation approach presents similarities to the ones proposed in Busto et al. [71] and Dumbser and Casulli [48] for the Eulerian variant of the governing equations: namely the use of a staggered grid is key to obtaining a simple scalar tridiagonal linear system for the predictor wave equation.

3.2.3. *Numerical diffusion for the specific volume*

The update formula (20) for the specific volume is a second order central difference, and does not include any artificial viscosity or Riemann solver dissipation. For this reason, undesirable spurious oscillations can be introduced by it. In order to inhibit the development of such numerical artifacts, we introduce a *stabilisation/filtering procedure* composed of two steps. First, the candidate solution $\left(V_i^{n+1}\right)_{\mathrm{c}}$ given by (20) is filtered in order to detect cells affected by excessive oscillations, and for each cell an alternative non-oscillatory value $V_i^{n+1,*}$ is computed. Second, since simply replacing in each cell the candidate solution $\left(V_i^{n+1}\right)_{\mathrm{c}}$ with $V_i^{n+1,*}$ might lead to unacceptable mass conservation errors, each value of the specific volume $\left(V_i^{n+1}\right)_{\mathrm{c}}$ is updated with a conservative numerical diffusion flux, yielding a corrected discrete volume field V_i^{n+1} satisfying mass conservation. The set of conservative fluxes is determined in such a way that its effect is as close as possible to that of the nonconservative cell-by-cell replacement of $\left(V_i^{n+1}\right)_{\mathrm{c}}$ with $V_i^{n+1,*}$. An important difference of course is that the flux form

$$V_i^{n+1} = \left(V_i^{n+1}\right)_{\mathrm{c}} - \frac{\Delta t}{\Delta m_i}\left(f_{i+1/2}^{V,\mathrm{d}} - f_{i-1/2}^{V,\mathrm{d}}\right) \tag{21}$$

ensures that mass is globally conserved for any choice of the diffusive fluxes $f_{i+1/2}^{V,\mathrm{d}}$, remarking that, in the same way, $\left(V_i^{n+1}\right)_{\mathrm{c}}$ is also computed by a comparable Finite Volume-type formula (20), which satisfies conservation exactly as formula (21). In order to achieve the desired diffusive effect, the fluxes are set to have the form

$$f_{i+1/2}^{V,\mathrm{d}} = -S_{i+1/2}\left[\left(V_{i+1}^{n+1}\right)_{\mathrm{c}} - \left(V_i^{n+1}\right)_{\mathrm{c}}\right], \tag{22}$$

with $S_{i+1/2}$ a non-negative coefficient analogous to the signal speed estimates of the Rusanov or Local Lax Friedrichs approximate fluxes.

Computation of the target filtered volume. The first step of the correction procedure applied to the specific volume consists in the determination of a filtered specific volume $V_i^{n+1,*}$. The quantity can also be termed *target* volume, since it is not used directly to replace $\left(V_i^{n+1}\right)_{\mathrm{c}}$, that is, the volume obtained by the conservative central difference update formula (20), but rather to determine the coefficients $S_{i+1/2}$ of the conservative diffusion fluxes (22), aiming at obtaining a result that approximates the target volume $V_i^{n+1,*}$ as closely as possible, while retaining exact conservation of mass.

Towards this goal, in each cell i, *if and only if the cell is a local extremum of the specific volume*, three candidates are made available: 1. the volume in the adjacent cell on the left $(V_i^{n+1,*})_1 = \left(V_{i-1}^{n+1}\right)_{\mathrm{c}}$, 2. the volume in the right adjacent cell $(V_i^{n+1,*})_2 = \left(V_{i+1}^{n+1}\right)_{\mathrm{c}}$, and 3. a third value obtained by a least-squares reconstruction involving a five cell stencil, of which only four are actually used: the two right neighbours and the two left neighbours of cell i. Contrary to other polynomial reconstruction operators [72–74] used in high order Finite Volume method, the cell average of the central cell $\left(V_i^{n+1}\right)_{\mathrm{c}}$ is completely ignored, since it coincides with the value potentially requiring a replacement. A local extremum is defined operatively as any cell where the left and right slopes switch sign, that is where

$$\left[(V_{i+1}^{n+1})_{\mathrm{c}} - (V_i^{n+1})_{\mathrm{c}}\right]\left[(V_{i-1}^{n+1})_{\mathrm{c}} - (V_i^{n+1})_{\mathrm{c}}\right] > \epsilon, \tag{23}$$

having set $\epsilon = 10^{-14}$, a small tolerance preventing random switching-type behaviour in completely flat regions.

For the reconstruction procedure that has to be carried out at extrema to compute $(V_i^{n+1,*})_3$, formally we define the vector of the stencil data for cell i to be

$$\mathbf{V}_i = \left((V_{i-2}^{n+1})_{\mathrm{c}},\ (V_{i-1}^{n+1})_{\mathrm{c}},\ (V_{i+1}^{n+1})_{\mathrm{c}},\ (V_{i+2}^{n+1})_{\mathrm{c}}\right)^{\mathsf{T}}. \tag{24}$$

The least-square reconstructed candidate value $(V_i^{n+1,*})_3$ can be then computed by solving the normal equations of the overdetermined system given by imposing conservation over each one of the four cells in the stencil with data $\mathbf{V}_i$. The four reconstruction equations are obtained by imposing that the cell average $(V_j^{n+1})_{\mathrm{c}}$ of each cell j in the stencil spanning from cell $i-2$ to cell $i+2$ (cell i excluded) be the same as that of a stencil-supported quadratic polynomial

$$P_i(m) = \sum_{k=0}^{2} \hat{P}_{i,k}\left(m - m_{i-2}\right)^k = \hat{P}_{i,0} + \hat{P}_{i,1}\left(m - m_{i-2}\right) + \hat{P}_{i,2}\left(m - m_{i-2}\right)^2, \tag{25}$$

averaged over the same cell j. The reconstruction equations are formally expressed as

$$\frac{1}{\Delta m_j}\int_{m_j}^{m_j+\Delta m_j} P_i(m)\,\mathrm{d}m = (V_j^{n+1})_{\mathrm{c}}, \qquad j \in \{i-2,\ i-1,\ i+1,\ i+2\} \tag{26}$$

recalling that m_j is the leftmost point of cell j and $\Delta m_j = m_{j+1} - m_j$. Since the four equation system (26) is overdetermined, it is solved in the least squares sense, yielding a vector of three coefficients $\hat{\mathbf{P}}_i$. The polynomial $P_i(m)$ is then integrated over cell i to obtain the reconstructed central cell average $(V_i^{n+1,*})_3$: in practice it is sufficient to take the dot product of the coefficients $\hat{\mathbf{P}}_i$ with an averaging operator $\mathbf{a}_i$, whose three components are the integrals of the three basis monomials 1, $m - m_{i-2}$, and $(m - m_{i-2})^2$ over cell i, divided by its size Δm_i. In our implementation, the solution to the normal equations and the averaging of the polynomial $P_i(m)$ over cell i are computed as

$$(V_i^{n+1,*})_3 = \hat{\mathbf{P}}_i \cdot \mathbf{a}_i = \left[\left(\mathbf{A}_i^\top \mathbf{A}_i \right)^{-1} \mathbf{A}_i^\top \mathbf{V}_i \right] \cdot \mathbf{a}_i \tag{27}$$

with the definitions

$$\mathbf{A}_i = \begin{pmatrix} 1 & \Delta m_{i-2}/2 & \Delta m_{i-2}^2/3 + \Delta m_{i-2}\, m_{i-2} + m_{i-2}^2 \\ 1 & \Delta m_{i-1}/2 & \Delta m_{i-1}^2/3 + \Delta m_{i-1}\, m_{i-1} + m_{i-1}^2 \\ 1 & \Delta m_{i+1}/2 & \Delta m_{i+1}^2/3 + \Delta m_{i+1}\, m_{i+1} + m_{i+1}^2 \\ 1 & \Delta m_{i+2}/2 & \Delta m_{i+2}^2/3 + \Delta m_{i+2}\, m_{i+2} + m_{i+2}^2 \end{pmatrix}, \qquad \mathbf{a}_i = \begin{pmatrix} 1 \\ \Delta m_i/2 + m_i \\ \Delta m_i^2/3 + \Delta m_i\, m_i + m_i^2 \end{pmatrix}. \tag{28}$$

Finally, the filtered specific volume $V_i^{n+1,*}$ is a weighted average of the three candidates

$$V_i^{n+1,*} = \sum_{k=1}^{3} w_k\, (V_i^{n+1,*})_k, \quad \text{with} \quad w_k = \frac{\widetilde{w_k}}{\sum_{k=1}^{3} \widetilde{w_k}}, \qquad \widetilde{w_k} = \left(\frac{1}{d_k + \epsilon} \right)^8, \qquad \epsilon = 10^{-14} \tag{29}$$

where the weights w_k are computed similarly to the classic WENO nonlinear coefficients [75–77], but with a CWENO-type [74,78] approach, using the aggressive choice of parameters given in Dumbser et al. [79,80], and with d_k being a simple indicator proportional to the distance of each of the candidate values for the filtered specific volume and the value to be corrected itself. Formally, for what concerns the expression of the indicator $d_k,\ k \in 1,\ 2,\ 3,$ we set

$$d_1 = (V_i^{n+1,*})_1 - \left(V_i^{n+1}\right)_{\mathrm{c}}, \qquad d_2 = (V_i^{n+1,*})_2 - \left(V_i^{n+1}\right)_{\mathrm{c}}, \qquad d_3 = K \left[(V_i^{n+1,*})_3 - \left(V_i^{n+1}\right)_{\mathrm{c}} \right], \tag{30}$$

which states that the weighted average will be biased towards correcting $\left(V_i^{n+1}\right)_{\mathrm{c}}$ as little as possible: the indicator d_k is simply a measure of the distance between each candidate value $(V_i^{n+1,*})_k$ and the cell average $(V_i^{n+1})_{\mathrm{c}}$ obtained by the conservative update formula (20). Additionally, the least-squares reconstructed value $(V_i^{n+1,*})_3$ is slightly penalised (by a multiplicative factor $K = 4$ in its indicator d_3) with respect to the other two candidates since at discontinuities the other two are clearly more reliable, while in smooth regions, where the data are well approximated by the reconstruction polynomial and the least-squares option is thus more accurate and preferable, the match with $\left(V_i^{n+1}\right)_{\mathrm{c}}$ will be such that $(V_i^{n+1,*})_3$ will have by far the largest weight regardless of the penalisation factor K.

Conservative redistribution of specific volume correction. Expanding on the conservative diffusive update formula given in (21), we set the diffusive flux to be of the form (22), here replicated for the reader's convenience

$$f_{i+1/2}^{V,\mathrm{d}} = -S_{i+1/2} \left[(V_{i+1}^{n+1})_{\mathrm{c}} - (V_i^{n+1})_{\mathrm{c}} \right]. \tag{31}$$

The numerical factor (one half) that would be present in the Rusanov flux is omitted here in (31), since the values of $S_{i+1/2}$ are not derived from some bounding estimates for the signal speeds of the PDE system, but rather computed as the result of an optimisation procedure aiming towards obtaining a close approximation of the (nonconservative) corrected values $V_i^{n+1,*}$, while retaining exact conservation. Hence the conservative diffusive correction for the specific volume reads

$$V_i^{n+1} = \left(V_i^{n+1}\right)_{\mathrm{c}} + \frac{\Delta t}{\Delta m_i}\, S_{i-1/2} \left[\left(V_{i-1}^{n+1}\right)_{\mathrm{c}} - \left(V_i^{n+1}\right)_{\mathrm{c}} \right] + \frac{\Delta t}{\Delta m_i}\, S_{i+1/2} \left[\left(V_{i+1}^{n+1}\right)_{\mathrm{c}} - \left(V_i^{n+1}\right)_{\mathrm{c}} \right]. \tag{32}$$

In the following paragraphs, we outline the procedure by which a set of coefficients $S_{i+1/2}$ can be assigned to each interface, so to mimic the output of the nonconservative filtering procedure given in the beginning of Section 3.2.3 by means of a strictly conservative formulation.

In each cell, we would like that the corrected specific volume V_i^{n+1} obtained from the conservative formula (32) be as close as possible to the non-conservative filtered value $V_i^{n+1,*}$. Finding the cell boundary coefficients $S_{i+1/2}$ that allow the best approximation of the target $V_i^{n+1} \to V_i^{n+1,*}$ over the N cells of the computational domain constitutes a rather large optimisation problem in the $N+1$ unknowns $S_{i+1/2}$.

On the contrary, within each cell, if the effect of the conservative diffusion flux on the two neighbours is ignored, the target can be can be trivially imposed as an exact constraint $V_i^{n+1} = V_i^{n+1,*}$ leading to

$$\left(V_i^{n+1}\right)_{\mathrm{c}} + A_{i,\mathrm{L}}\, S_{i,\mathrm{L}} + A_{i,\mathrm{R}}\, S_{i,\mathrm{R}} = V_i^{n+1,*}, \tag{33}$$

with

$$A_{i,\mathrm{L}} = \frac{\Delta t}{\Delta m_i} \left[\left(V_{i-1}^{n+1}\right)_{\mathrm{c}} - \left(V_i^{n+1}\right)_{\mathrm{c}} \right], \quad A_{i,\mathrm{R}} = \frac{\Delta t}{\Delta m_i} \left[\left(V_{i+1}^{n+1}\right)_{\mathrm{c}} - \left(V_i^{n+1}\right)_{\mathrm{c}} \right]. \tag{34}$$

Note that (33) has multiple solutions and in order to obtain a unique pair $S_{i,\mathrm{L}}, S_{i,\mathrm{R}}$, an additional constraint has to be imposed, specifically we choose to select the solution that has minimum square norm $\|\mathbf{S}_i\|^2 = S_{i,\mathrm{L}}^2 + S_{i,\mathrm{R}}^2$, as explained in (38). The definition of a unique intercell face value

$$S_{i+1/2} = \frac{1}{2} \left(S_{i,\mathrm{L}} + S_{i,\mathrm{R}} \right) \tag{35}$$

guarantees that the resulting update (32) due to artificial diffusion will be conservative.

Below we explain in detail the procedure adopted to compute $S_{i,\mathrm{L}}$ and $A_{i,\mathrm{L}}$. In order to enforce equality (33), one one only has to express either $S_{i,\mathrm{L}}$ or $S_{i,\mathrm{R}}$ as a linear function of the other. For example, if the coefficient $A_{i,\mathrm{L}}$ is not zero (meaning that there is a jump in the specific volume V between cell i and cell $i-1$), then one can set

$$S_{i,\mathrm{L}} = \frac{V_i^{n+1,*} - V_i^{n+1}}{A_{i,\mathrm{L}}} - \frac{A_{i,\mathrm{R}}}{A_{i,\mathrm{L}}}\, S_{i,\mathrm{R}}, \tag{36}$$

or equivalently, if $A_{i,\mathrm{R}} > 0$, i.e. when a nonzero jump is present at the interface $i+1/2$, one can impose

$$S_{i,\mathrm{R}} = \frac{V_i^{n+1,*} - V_i^{n+1}}{A_{i,\mathrm{R}}} - \frac{A_{i,\mathrm{L}}}{A_{i,\mathrm{R}}}\, S_{i,\mathrm{L}}. \tag{37}$$

Within cell i, a local optimality condition can be then formulated by finding the two component vector $\mathbf{S}_i = (S_{i,\mathrm{L}},\ S_{i,\mathrm{R}})^\top$ which has minimum norm. This is immediately obtained starting for example from (36), computing the norm of $\mathbf{S}_i$

$$\|\mathbf{S}_i\|^2 = S_{i,\mathrm{L}}^2 + S_{i,\mathrm{R}}^2 = B_0^2 - 2\,B_0\,B_1\,S_{i,\mathrm{R}} + \left(1 + B_0^2\right) S_{i,\mathrm{R}}, \tag{38}$$

and setting its derivative with respect to $S_{i,\mathrm{R}}$ to zero, obtaining

$$S_{i,\mathrm{R}} = \frac{B_0\,B_1}{1 + B_1^2}, \qquad S_{i,\mathrm{L}} = B_0 - B_1\,S_{i,\mathrm{R}}, \tag{39}$$

with the definitions (omitting the index i for the sake of notational compactness)

$$B_0 = \frac{V_i^{n+1,*} - \left(V_i^{n+1}\right)_{\mathrm{c}}}{A_{i,\mathrm{L}}}, \qquad B_1 = \frac{A_{i,\mathrm{R}}}{A_{i,\mathrm{L}}}. \tag{40}$$

Provided that Eq. (37) is valid, the same procedure can be carried out starting from it instead of (36), leading to the same results. In order to avoid division by zero and minimize roundoff errors, in practice we choose (36) if $|A_{i,\mathrm{L}}| \geq |A_{i,\mathrm{R}}|$ and (37) otherwise. If (37) is chosen, then the sought coefficients are

$$S_{i,\mathrm{L}} = \frac{C_0\,C_1}{1 + C_1^2}, \qquad S_{i,\mathrm{R}} = C_0 - C_1\,S_{i,\mathrm{L}}, \tag{41}$$

having defined (again omitting the implied index i)

$$C_0 = \frac{V_i^{n+1,*} - \left(V_i^{n+1}\right)_{\mathrm{c}}}{A_{i,\mathrm{R}}}, \qquad C_1 = \frac{A_{i,\mathrm{L}}}{A_{i,\mathrm{R}}}. \tag{42}$$

In our implementation, towards the goal of preventing symmetry-breaking effects from floating point roundoff errors as much as possible, whenever both $A_{i,\mathrm{L}}$ and $A_{i,\mathrm{R}}$ are strictly positive (in practice greater than 10^{-8}) and differ from each other by less than the same threshold of 10^{-8}, then both (36) and (37) are used to generate two values of $S_{i,\mathrm{L}}$ and $S_{i,\mathrm{R}}$ in cell i, which are then arithmetically averaged.

If both $A_{i,\mathrm{L}}$ and $A_{i,\mathrm{R}}$ fall below the 10^{-8} threshold, then $S_{i,\mathrm{L}} = 0$, and $S_{i,\mathrm{R}} = 0$ for cell i, which corresponds to no diffusion. Note that in principle there is no guarantee that the conservative redistribution of these diffusive terms will preserve the non oscillatory character of the (non-conservative) corrected values of the specific volume, but in practice, due to the iterative nature of the scheme, the correction tends to behave well and does not introduce the oscillations back.

3.2.4. Update of the velocity field

The velocity field $u_{i+1/2}^{n+1}$ is updated at the edge locations according to (13), and the auxiliary cell-center values u_i^{n+1} are computed immediately after by interpolation, that is by defining an interpolated cell center velocity

$$u_i^{n+1} = \frac{\Delta m_{i+1/2}\,u_{i-1/2} + \Delta m_{i-1/2}\,u_{i+1/2}}{\Delta m_{i-1/2} + \Delta m_{i+1/2}}. \tag{43}$$

It should be stressed that u_i^{n+1} is used just for the computation of specific total energy whenever the quasi-conservative pressure corrections detailed in Section 3.2.5 are applied, and the quantity to be integrated in time is $u_{i+1/2}$, since interpolating backwards from cell centers to edge values would introduce Lax-Friedrichs-like dissipation terms [81], quickly degrading the accuracy of the method. If more aggressive numerical diffusion is required, as we found to be necessary for the two of the shock tube problems of Toro shown in Section 5.1, we refer the reader to the procedure detailed in Appendix A.

3.2.5. *Conservative update of energy, numerical diffusion and filtering*

Conservative update of total energy. A candidate specific energy updated value is which is based on a conservative flux form and thus works also in presence of shockwaves

$$(E_i^{n+1})_{\mathrm{c}} = E_i^n - \frac{\Delta t}{\Delta m_i}\left((F_E)_{i+1/2}^{n+1} - (F_E)_{i-1/2}^{n+1}\right), \tag{44}$$

with the fluxes being

$$\begin{aligned} (F_E)_{i-1/2}^{n+1} &= u_{i-1/2}^{n+1}\, p_{i-1/2}^{n+1} - \frac{1}{2}\,(s_E)_{i-1/2}\left(p_{i-1/2,+}^{n+1} - p_{i-1/2,-}^{n+1}\right),\\ (F_E)_{i+1/2}^{n+1} &= u_{i+1/2}^{n+1}\, p_{i+1/2}^{n+1} - \frac{1}{2}\,(s_E)_{i+1/2}\left(p_{i+1/2,+}^{n+1} - p_{i+1/2,-}^{n+1}\right). \end{aligned} \tag{45}$$

The energy fluxes (45) are the sum of a central part and a diffusive part, just like the Rusanov (or local Lax–Friedrichs) [70] and Ducros [82] fluxes. Note however that the jumps $p_{i-1/2,+}^{n+1} - p_{i-1/2,-}^{n+1}$ are not the jumps of the conserved variables (the specific energy E) but rather they are pressure jumps. This is motivated by the fact that diffusive part of (45) is intended to introduce as little numerical diffusion as possible and in particular at material interfaces we can expect the pressure field to be smooth. On the other hand, even in complete absence of shock waves, the specific energy E might jump from one cell to another in a discontinuous manner, for example at material interfaces where the parameters of the equation of state change. The central part simply requires the computation of a cell-edge interpolated pressure

$$p_{i+1/2}^{n+1} = \frac{\Delta m_{i+1}\, p_i^{n+1} + \Delta m_i\, p_{i+1}^{n+1}}{\Delta m_i + \Delta m_{i+1}}, \tag{46}$$

and the diffusive part is a function of the minmod-reconstructed pressure jumps $p_{i+1/2}^{+} - p_{i+1/2}^{-}$ at each cell interface, also computed starting from the discrete wave equation solution p_i^{n+1}. The boundary extrapolated values $p_{i+1/2}^{-}$ and $p_{i+1/2}^{+}$ are defined as

$$p_{i+1/2,-}^{n+1} = p_i^{n+1} + \delta p_i/2, \qquad p_{i+1/2,+}^{n+1} = p_{i+1}^{n+1} - \delta p_{i+1}/2, \tag{47}$$

and the pressure increments due to the reconstruction procedure are

$$\delta p_i = \Delta m_i \,\mathrm{minmod}\left(\frac{p_i - p_{i-1}}{\Delta m_{i-1/2}},\ \frac{p_{i+1} - p_i}{\Delta m_{i+1/2}}\right), \tag{48}$$

with the minmod function defined by

$$\mathrm{minmod}\big(\delta_{\mathrm{L}},\ \delta_{\mathrm{R}}\big) = \frac{1}{2}\left(\mathrm{sign}\big(\delta_{\mathrm{L}}\big) + \mathrm{sign}\big(\delta_{\mathrm{R}}\big)\right)\ \min\left(\big|\delta_{\mathrm{L}}\big|,\ \big|\delta_{\mathrm{R}}\big|\right) \tag{49}$$

The coefficients $(s_E)_{i-1/2}$ and $(s_E)_{i+1/2}$ are Rusanov-type signal speed estimates computed as

$$(s_E)_{i+1/2} = \max\left(\frac{V_i^{n+1}}{\gamma_i - 1},\ \frac{V_{i+1}^{n+1}}{\gamma_{i+1} - 1}\right)\ \max\left(\frac{u_i^{n+1}}{V_i^{n+1}},\ \frac{u_{i+1}^{n+1}}{V_{i+1}^{n+1}}\right), \tag{50}$$

where the first scaling coefficient, proportional to $V/(\gamma - 1)$, is intended to convert pressure jumps into jumps of specific internal energy E. Since such scaling factor introduces a dimensional constant proprtional to V, the correct dimensionality of $(s_E)_{i+1/2}$ (a velocity) is restored by taking the maximum of the momenta in the cells i and $i+1$. If the two fluids have similar densities and equation of state and the velocity is continuous across an interface, the factor $(s_E)_{i+1/2}$ is approximately $(s_E)_{i+1/2} \sim u_{i+1/2}^{n+1}/(\gamma_{i+1/2} - 1)$, whereas if a significant jump in density is present, the coefficient $(s_E)_{i+1/2}$ incorporates a scaling factor proportional to the ratio between the maximum and the minimum density, effectively increasing the dissipation at shocks and material interfaces.

It should be remarked that such estimates, in order to introduce as little numerical dissipation as possible, are based on the flow velocity and not on the speed of sound or the eigenvalues of the governing hyperbolic system, as they would be for a standard explicit scheme. Moreover, due to the use of pressure jumps in lieu of specific energy jumps, the signal speeds $(s_E)_{i+1/2}$ include a dimensional scaling coefficient, based on the derivative of specific energy E with respect to pressure, so that dimensionality and scaling of the involved quantities are accounted for.

Removal of pressure oscillations/merging different candidates for the pressure field. With reference to the second panel of Fig. 1, and taking into account for the observations given in Abgrall and Karni [69], we introduce a quasi-conservative correction which is intended to eliminate the pressure spikes that arise at material interfaces, where the parameters of the equation of state jump between different values. We point out that such small non-conservative corrections, as discussed in Gaburro et al. [83], do not lead to highly undesirable effects like shockwaves propagating with the wrong speed, precisely due to their small pointwise nature. This statement is tested in the paper by applying the method to a variety of classic benchmarks featuring strong shocks. Towards this goal, we simply compute the specific energy E_i^{n+1} in a cell by cell fashion as a convex combination of its conservative updated value $(E_i^{n+1})_{\mathrm{c}}$ and a second value $(E_i^{n+1})_{\mathrm{p}}$ obtained solely based on predictor information, which is nonconservative in principle.

$$E_i^{n+1} = \big(1 - w_i\big)\,(E_i^{n+1})_{\mathrm{c}} + w_i\,(E_i^{n+1})_{\mathrm{p}} \tag{51}$$

with $(E_i^{n+1})_\mathrm{p}$ denoting the specific total energy that can be computed as a pointwise function

$$(E_i^{n+1})_\mathrm{p} = (E_i^{n+1})_\mathrm{p}\left(p_i^{n+1},\ u_{i-1/2}^{n+1},\ u_{i+1/2}^{n+1},\ V_i^{n+1}\right) = V_i^{n+1}\,\frac{p_i^{n+1} + \gamma_i\,\Pi_i}{\gamma_i - 1} + \frac{(u_i^{n+1})^2}{2}. \tag{52}$$

The blending weight w_i is computed as

$$w_i = \min\left(1,\ \frac{1}{D}\left|(p_i^{n+1})_\mathrm{c} - \frac{\Delta m_{i+1/2}\,(p_{i-1}^{n+1})_\mathrm{c} + \Delta m_{i-1/2}\,(p_{i+1}^{n+1})_\mathrm{c}}{\Delta m_{i-1/2} + \Delta m_{i+1/2}}\right|\right)^r. \tag{53}$$

The motivation for this choice of blending weight is given in the following paragraphs. Here, $(p_i^{n+1})_\mathrm{c}$ denotes the pressure field induced by the conservative energy update, that is

$$(p_i^{n+1})_\mathrm{c} = \frac{\gamma_i - 1}{V_i^{n+1}}\left[\left(E_i^{n+1}\right)_\mathrm{c} - \frac{(u_i^{n+1})^2}{2}\right] - \gamma_i\,\Pi_i, \tag{54}$$

and D being a scaling factor defined as

$$D = \max\left(p_{i-2}^{n+1},\ p_{i-1}^{n+1},\ p_{i+1}^{n+1},\ p_{i+2}^{n+1}\right) - \min\left(p_{i-2}^{n+1},\ p_{i-1}^{n+1},\ p_{i+1}^{n+1},\ p_{i+2}^{n+1}\right) + \epsilon. \tag{55}$$

Finally we set the exponent $r = 8$ in (53) to be a fixed parameter used to smoothly approximate a binary switch between $w_i = 0$ and $w_i = 1$, and set $\epsilon = 10^{-14}$, a small constant aimed at avoiding division by zero. The purpose of (53) is to compare the pressure $(p_i^{n+1})_\mathrm{c}$ given by the conservative update of energy (44) in cell i with the pressure obtained by linearly interpolating the two neighbouring values, thus measuring the deviation from a simple linear distribution. Wherever such discrepancy is high, relative to the scaling factor D based on the pressure field p_i (the one derived solely from the wave equation), a pressure spike has been detected and the weighting factor w_i will tend towards unity, while in smooth regions of the pressure field the correction is essentially null, since the match between the pressure $(p_i^{n+1})_\mathrm{c}$ and the neighbour-interpolated value will be much smaller than the feature size indicated by D, thereby driving w_i towards zero, due to the high exponent $r = 8$, approximating a rather sharp switch. This means that the heuristic (53) is designed in such a way that the pressure field is replaced by the smooth predictor solution whenever quantified as oscillatory, while safeguarding the conservativity of the method as much as possible since in most flow regions the nonconservative contribution is negligible.

3.3. *Time integration*

The time integration approach adopted in this work is very simple and leverages the Stiffly-accurate Diagonally implicit Runge–Kutta schemes originally introduced by Crouzeix [84], Alexander [85] (see also Ascher et al. [59], Pareschi and Russo [60] and the Review by Kennedy and Carpenter [86]). Formally, we define an implicit solution operator $\mathcal{H}_\mathrm{I}(\mathbf{Q},\ \Delta t)$ that maps an initial state vector $\mathbf{Q} = \left(V_i,\ u_{i+1/2},\ E_i\right)$, with $i = 1,\ 2,\ \ldots,\ N$ (and including $i = 0$ for the left boundary value of the velocity field), to an updated vector $\mathcal{H}_\mathrm{I}(\mathbf{Q}^n,\ \Delta t)$, given by our implicit discretisation scheme. With reference to the notation adopted in the above sub-sections, the updated values for a timestep of size Δt will be

$$\mathcal{H}_\mathrm{I}(\mathbf{Q}^n,\ \Delta t) = \left(V_i^{n+1},\ u_{i+1/2}^{n+1},\ E_i^{n+1}\right). \tag{56}$$

The approach proposed in this paper is tested with two time integration schemes, one of second order (labelled SDIRK2) with two stages, defined by the Butcher array

$$\begin{array}{c|cc} \gamma & \gamma & 0 \\ 1 & a_{21} & \gamma \\ \hline & a_{21} & \gamma \end{array} \qquad \text{with} \qquad \begin{aligned} \gamma &= 1 - 1/\sqrt{2}, \\ a_{21} &= 1 - \gamma, \end{aligned} \tag{57}$$

and implemented in practice as a sequence of two Euler steps

$$\begin{aligned} \mathbf{Q}_1 &= \mathcal{H}_\mathrm{I}\big(\mathbf{Q}_1^*,\ \gamma\,\Delta t\big), \\ \mathbf{Q}^{n+1} &= \mathcal{H}_\mathrm{I}\big(\mathbf{Q}_2^*,\ \gamma\,\Delta t\big), \end{aligned} \qquad \text{with} \qquad \begin{aligned} \mathbf{Q}_1^* &= \mathbf{Q}^n, \\ \mathbf{Q}_2^* &= c_{20}\,\mathbf{Q}^n + c_{21}\,\mathbf{Q}_1. \end{aligned} \tag{58}$$

The coefficients c_{20} and c_{21} are $c_{20} = 1 - a_{21}/\gamma$ and $c_{21} = a_{21}/\gamma$.

A second time integration scheme is the three-stage, third order scheme defined by

$$\begin{array}{c|ccc} \gamma & \gamma & 0 & 0 \\ k_c & a_{21} & \gamma & 0 \\ 1 & a_{31} & a_{32} & \gamma \\ \hline & a_{31} & a_{32} & \gamma \end{array} \qquad \text{with} \qquad \begin{aligned} \gamma &= 0.435866521508459, \\ a_{21} &= k_c - \gamma, \\ a_{31} &= 1 - k_d - \gamma, \\ a_{32} &= k_d, \end{aligned} \qquad \begin{aligned} k_a &= 1 - 4\,\gamma + 2\,\gamma^2, \\ k_b &= 3\,\gamma\,\left(2 - 3\,\gamma + \gamma^2\right) - 1, \\ k_c &= (2/3 - 3\,\gamma + 2\,\gamma^2)/k_a, \\ k_d &= -3\,k_a^2/(4\,k_b), \end{aligned} \tag{59}$$

for which the implementation reads

$$\begin{aligned} \mathbf{Q}_1 &= \mathcal{H}_\mathrm{I}\big(\mathbf{Q}_1^*,\ \gamma\,\Delta t\big), \\ \mathbf{Q}_2 &= \mathcal{H}_\mathrm{I}\big(\mathbf{Q}_2^*,\ \gamma\,\Delta t\big), \\ \mathbf{Q}^{n+1} &= \mathcal{H}_\mathrm{I}\big(\mathbf{Q}_3^*,\ \gamma\,\Delta t\big), \end{aligned} \qquad \text{with} \qquad \begin{aligned} \mathbf{Q}_1^* &= \mathbf{Q}^n, \\ \mathbf{Q}_2^* &= c_{20}\,\mathbf{Q}^n + c_{21}\,\mathbf{Q}_1, \\ \mathbf{Q}_3^* &= c_{30}\,\mathbf{Q}^n + c_{31}\,\mathbf{Q}_1 + c_{32}\,\mathbf{Q}_2, \end{aligned} \tag{60}$$

The variation (60) is provided so that in practice one can conveniently implement the Runge–Kutta integrator purely as a sequence of implicit Euler steps. The coefficients c_{ij} are

$$c_{21} = a_{21}/\gamma, \qquad c_{20} = 1 - c_{21}, \qquad c_{32} = a_{32}/\gamma, \qquad c_{31} = (a_{31} - c_{32}\, a_{21})/\gamma, \qquad c_{30} = 1 - c_{31} - c_{32}. \tag{61}$$

3.4. *Explicit reference schemes*

The explicit Lagrangian schemes used for reference in the convergence and efficiency studies are the based on the well-known method of Munz [87], with the addition of an exact two-material Riemann solver two Strong-Stability-Preserving Runge–Kutta time-stepping schemes [88]. In the notation adopted in this paper, the scheme of Munz, including a low-dissipation TVD reconstruction operator (see van Leer [89], Kurganov and Tadmor [90]), mapping an initial condition $\mathbf{Q}^n$ to its evolved state $\mathbf{Q}^{n+1}$ over a time interval Δt. With notation, the first one of the two explicit time-stepping schemes is the two stage method [88] (labelled SSPRK2) having Butcher table

$$\begin{array}{c|cc} 0 & 0 & 0 \\ 1 & a_{21} & 0 \\ \hline & b_1 & b_2 \end{array} \qquad \text{with} \qquad \begin{array}{l} a_{21} = 1, \\ b_1 = b_2 = 1/2, \end{array} \tag{62}$$

which has a very simple implementation given by

$$\begin{array}{l} \mathbf{Q}_1 = \mathcal{H}_{\mathrm{E}}(\mathbf{Q}^n,\ \Delta t), \\ \mathbf{Q}^{n+1} = (1 - c_1)\,\mathbf{Q}^n + c_1\, \mathcal{H}_{\mathrm{E}}\big(\mathbf{Q}_2,\ \Delta t\big), \end{array} \qquad \text{with} \qquad c_1 = 1/2. \tag{63}$$

Furthermore, we compared our results with those produced by the same second-order TVD spatial reconstruction and exact Riemann solver, but with a three-stage third order SSP Runge–Kutta scheme [88], labelled in this paper SSPRK3, defined by the Butcher table

$$\begin{array}{c|ccc} 0 & 0 & 0 & 0 \\ 1 & a_{21} & 0 & 0 \\ 1/2 & a_{31} & a_{32} & 0 \\ \hline & b_1 & b_2 & b_3 \end{array} \qquad \text{with} \qquad \begin{array}{l} a_{21} = 1, \\ a_{31} = a_{32} = 1/4, \\ b_1 = b_2 = 1/6, \\ b_3 = 2/3, \end{array} \tag{64}$$

which in practice is implemented as

$$\begin{array}{l} \mathbf{Q}_1 = \mathcal{H}_{\mathrm{E}}(\mathbf{Q}^n,\ \Delta t), \\ \mathbf{Q}_2 = (1 - c_1)\,\mathbf{Q}^n + c_1\, \mathcal{H}_{\mathrm{E}}\big(\mathbf{Q}_1,\ \Delta t\big), \\ \mathbf{Q}^{n+1} = (1 - c_2)\,\mathbf{Q}^n + c_2\, \mathcal{H}_{\mathrm{E}}\big(\mathbf{Q}_2,\ \Delta t\big), \end{array} \qquad \text{with} \qquad \begin{array}{l} c_1 = 1/4, \\ c_2 = 2/3. \end{array} \tag{65}$$

4. Generating mass-constrained meshes with smoothly variable non-uniform spacing in mass coordinates

We discuss the task of generating a computational mesh (in our simple one-dimensional context, this means a sequence of mesh spacing values Δm_i), with the aim of applying the implicit Lagrangian scheme to flows in stratified systems, characterized by several layers, alternating regions of constant width having two different densities ρ_1 and ρ_2.

A first natural choice consists in selecting a uniform fixed spacing Δm, and a second one specifies two values for the mesh spacing Δm_1 and Δm_2, for example computed in such a way that $\Delta m_1 = \rho_1\, \Delta x$ and $\Delta m_2 = \rho_2\, \Delta x$ corresponding to the same step Δx in Eulerian coordinates.

The first choice, a uniform spacing Δm, when used in stratified media with alternating densities, suffers from two significant drawbacks. First, when the constant width layers have very different densities, the resolution in the lighter regions can be much lower, meaning that either excessively fine grids will be required for the denser fluid layers, or that the flow in lighter layers will be severely under-resolved.

In the canonical example of water-air-like density ratio $\rho_2/\rho_1 = 1000$, if a single grid point is associated with each one of 10 air-like layers (which is totally inadequate for any flow condition), then 10,000 additional cells will be required for keeping the uniform spacing in the 10 water-like layers.

The main issue with the second type of mesh, having two mass-spacing values Δm_1 and Δm_2 jumping across layer boundaries where the density switches from ρ_1 to ρ_2, is that the artificial diffusion of the numerical scheme (and in general the modified equation associated with it), will change discontinuously at boundaries, potentially giving rise to spurious oscillations and in general deteriorating the quality of the solution.

Hence it is clear that some strategy for defining a smoothly varying mesh is required for applications involving stratified multilayer media.

A simple enough strategy for computing the Lagrangian mass-coordinate spacing values Δm_i is given in the next paragraphs.

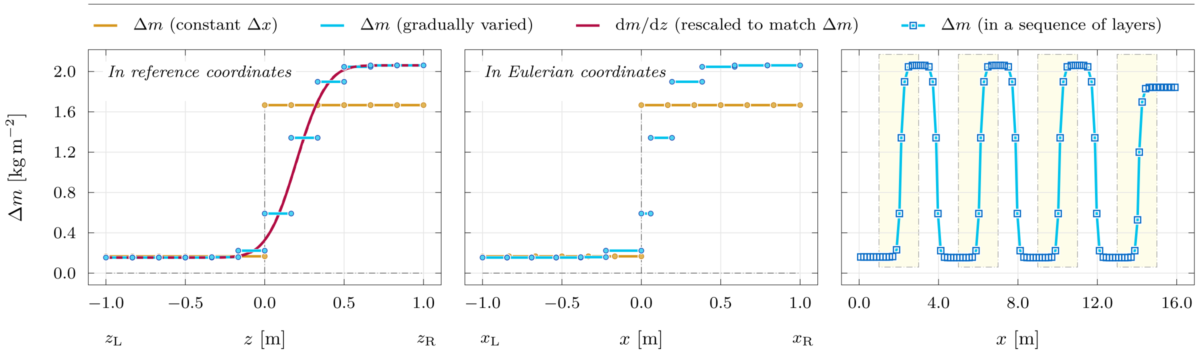

Fig. 2. Illustration of the graded mesh generation procedure. In the left panel, we show the cell mass content Δm as a function of the auxiliary (reference) coordinate z, along with the mesh spacing that would be induced by fixed uniform value of Δx, and the mass density function $\mathrm{d}m/\mathrm{d}z$ from which Δm is integrated (graphically rescaled to match the plot of Δm). In the central panel, we show how the smooth transient in reference coordinates translates to Eulerian coordinates (that is, as a function of x). In the right panel we show how several copies of the half-layer-couples are connected in a sequence of four layer couples. The regions corresponding to the central panel are highlighted. Note the presence of a boundary effect on the mesh spacing due to the fact that the first and last half-layer of the domain has a constant mesh spacing, unlike the internal ones.

4.1. Mesh for a step density distribution

In this section, we outline the procedure adopted for constructing a well graded Lagrangian mesh for a sub-domain composed of two regions of constant density. We refer to this sub-system as a half-layer pair, since it can be obtained by splitting each constant density layer of a stratified medium in two halves and focusing on a given interface between two layers. Since the final mesh for the multilayer system will be composed of a series of such half-layer couples, suitably mirrored in an alternated sequence, studying this simple configuration of two half-layers will be sufficient to define the final mesh in full. In particular, it will be enough to define n values Δm_i in each layer pair to specify the mesh in full.

With reference to Fig. 2, consider a pair of half-layers having density ρ_{L} and ρ_{R} in the left layer and in the right layer respectively. An auxiliary coordinate system z (which can be thought of as an “enumerating” space where distance varies by a fixed amount per cell) is constructed, such that $z = 0$ at the interface between the two layers, $z = z_{\mathrm{L}} = x_{\mathrm{L}}$ at the center of the left layer (corresponding by definition to the left extremum of left half-layer) and $z = z_{\mathrm{R}} = x_{\mathrm{R}}$ at the center of the right layer (corresponding by definition to the right extremum of right half-layer). Note that, while the x and z coordinates match at the interface between the two layers ($x = z = 0$), and at the boundaries of the half-layer pair (-1 m and $+1$ m in this example), z does not coincide at all with x within each layer: in Fig. 2 it is clear that z increases exactly by the constant Δz in each cell, while in the Eulerian reference frame each cell has a different width.

Within each half-layer pair, we will obtain a sequence of discrete mesh spacing values Δm_i by defining and integrating a smooth *mesh density function* $\mathrm{d}m/\mathrm{d}z(z)$, which will be constructed in such a way that the width and mass content of each layer are described exactly, which is the main nontrivial constraint in generating Lagrangian mass-coordinate meshes for two-density systems if such grids are not simply taken to have layer-wise constant spacing as in Phan et al. [10]. Smoothness of the mesh at the junction points (where mirrored half-layer couples are glued together) is ensured by the fact that the mesh spacing is almost constant near both boundaries of a half-layer pair, that is, the mesh density assumes a sigmoid shape. In the example of Fig. 2, the reference frame runs from $z_{\mathrm{L}} = -1$ m to $z_{\mathrm{R}} = 1$ m. In this reference frame we define each one of the n mesh spacing as the integral of a density-like function, or formally

$$\Delta m_i = \int_{z_1^i}^{z_2^i} \frac{\mathrm{d}m}{\mathrm{d}z}(z)\,\mathrm{d}z, \qquad \text{with } z_1^i = z_i - \Delta z/2,\ z_2^i = z_i + \Delta z/2, \qquad i = 1,\ 2,\ \dots,\ n \tag{66}$$

and with Δz specified as $\Delta z = (z_{\mathrm{R}} - z_{\mathrm{L}})/n$. The number n of cells of the half-layer pair can be chosen arbitrarily, and the procedure will automatically generate a density-like function δm which satisfies two mandatory requirements for any choice of n: first, the total mass contained in the left half-layer must be equal to $M_{\mathrm{L}} = \rho_{\mathrm{L}}\left(-z_{\mathrm{L}}\right)$, and likewise in the right half layer $M_{\mathrm{R}} = \rho_{\mathrm{R}}\, z_{\mathrm{R}}$. Second, at the same time, the Eulerian mesh spacing values Δx_i will sum to $-z_{\mathrm{L}}$ on the left half-layer and sum to z_{R} on the right half layer. This means that the smoothly varying mesh is constructed in such a way that both the Eulerian coordinate x and the Lagrangian mass coordinate m of each material interface are the ones initially specified by the problem setup, meaning that the mesh is forced to preserve at the same time the width and mass content of each layer. Formally the mass conservation constraints are imposed by requiring that

$$\int_{z_{\mathrm{L}}}^{0} \frac{\mathrm{d}m}{\mathrm{d}z}(z)\,\mathrm{d}z = M_{\mathrm{L}} = -\rho_{\mathrm{L}}\, z_{\mathrm{L}}, \qquad \int_{0}^{z_{\mathrm{R}}} \frac{\mathrm{d}m}{\mathrm{d}z}(z)\,\mathrm{d}z = M_{\mathrm{R}} = \rho_{\mathrm{R}}\, z_{\mathrm{R}}, \tag{67}$$

meaning, the density function integrated over each half-layer must equal the total mass expected for that segment, so to ensure that both mass conservation and the positions of material interfaces are strictly maintained.

The density-like function is chosen so that it will smoothly interpolate the discrete mesh spacing Δm_i between a left value Δm_L and a right value Δm_R. Specifically, the following form is adopted

$$\frac{\mathrm{d}m}{\mathrm{d}z}(z) = \Delta m_\mathrm{L} + \frac{1}{2}\left(\Delta m_\mathrm{R} - \Delta m_\mathrm{L}\right)\left[1 + \operatorname{erf}\left(\frac{z - z_0}{L_\beta}\right)\right]. \tag{68}$$

As a clarification note, we recall that $\operatorname{erf}(x) = \left(2/\sqrt{\pi}\right)\int_0^x \exp\left(-t^2\right)\mathrm{d}t$, which gives a function normalized between -1 and 1. The formula is parametrised by z_0 (a coordinate shift) and L_β, a characteristic length controlling the width of the transition zone between two constant regions in which the mesh spacing will be Δm_L and Δm_R. In practice the length L_β is computed as $L_\beta = \beta\,\min(-z_\mathrm{L},\ z_\mathrm{R})$, so the parameter to be fixed is a nondimensional value β.

For any fixed choice of z_0 and β, the mesh spacing at the left and right Δm_L and Δm_R will be determined by imposing the mass conservation constraint (67) on (68), which yields

$$\begin{pmatrix}\Delta m_\mathrm{L}\\ \Delta m_\mathrm{R}\end{pmatrix} = \begin{pmatrix}-z_\mathrm{L} + k_\mathrm{L} & -z_\mathrm{L} - k_\mathrm{L}\\ z_\mathrm{R} - k_\mathrm{L} & z_\mathrm{R} + k_\mathrm{R}\end{pmatrix}^{-1}\begin{pmatrix}-\rho_\mathrm{L}\, z_\mathrm{L}\\ \rho_\mathrm{R}\, z_\mathrm{R}\end{pmatrix}, \tag{69}$$

having defined the auxiliary constants

$$\begin{aligned}
k_\mathrm{L} &= \frac{L_\beta}{\sqrt{\pi}}\left\{\exp\left[-\left(\frac{-z_\mathrm{L} + z_0}{L_\beta}\right)^2\right] - \exp\left[-\left(\frac{z_0}{L_\beta}\right)^2\right]\right\} + \left(-z_\mathrm{L} + z_0\right)\operatorname{erf}\left(\frac{-z_\mathrm{L} + z_0}{L_\beta}\right) - z_0\operatorname{erf}\left(\frac{z_0}{L_\beta}\right),\\
k_\mathrm{R} &= \frac{L_\beta}{\sqrt{\pi}}\left\{\exp\left[-\left(\frac{z_\mathrm{R} - z_0}{L_\beta}\right)^2\right] - \exp\left[-\left(\frac{z_0}{L_\beta}\right)^2\right]\right\} + \left(z_\mathrm{R} - z_0\right)\operatorname{erf}\left(\frac{z_\mathrm{R} - z_0}{L_\beta}\right) - z_0\operatorname{erf}\left(\frac{z_0}{L_\beta}\right).
\end{aligned} \tag{70}$$

The mass content $\mathcal{M}(z_1,\ z_2)$ associated with a generic interval delimited by z_1 and z_2 is

$$\begin{aligned}
\mathcal{M}(z_1,\ z_2) = {}& \frac{L_\beta\left(\Delta m_\mathrm{R} - \Delta m_\mathrm{L}\right)}{2\sqrt{\pi}}\left[\exp\left(-\zeta_2^2\right) - \exp\left(-\zeta_1^2\right)\right] + \frac{1}{2}\left(\Delta m_\mathrm{R} + \Delta m_\mathrm{L}\right)\left(z_2 - z_1\right) + \\
& + \frac{1}{2}\left(\Delta m_\mathrm{R} - \Delta m_\mathrm{L}\right)\left[\left(z_2 - z_0\right)\operatorname{erf}\left(\zeta_2\right) - \left(z_1 - z_0\right)\operatorname{erf}\left(\zeta_1\right)\right],
\end{aligned} \tag{71}$$

with $\zeta_1 = (z_1 - z_0)/L_\beta$ and $\zeta_2 = (z_2 - z_0)/L_\beta$. Then the mesh spacing for each cell i is directly computed by evaluating $\Delta m_i = \mathcal{M}(z_i - \Delta z/2,\ z_i + \Delta z/2)$. Since the values of β and z_0 which yield well graded meshes, or the range of selectable values itself, are not immediately apparent, a simple procedure to compute these parameters automatically is discussed in Appendix B.

5. Numerical results

This section collects several numerical experiments aimed at validating the novel elements of the numerical solver proposed in this paper, and discussing their stability and convergence characteristics from an experimental point of view, as well as applications of the designed scheme to multi-layered, finely stratified two-fluid systems. The reader interested in the application results for two-fluid multi-layered systems may jump directly to Section 5.5, where these problems are considered, skipping Sections 5.1–5.4.

In Sections 5.1–5.4, we aim to demonstrate that the proposed numerical scheme is robust and accurate, and experimentally assess its convergence properties. It also demonstrates the degree to which the scheme can handle sharp material interfaces and strong shockwaves and generates or does not generate oscillations as a result of their presence. Such experimental validation is necessary due to the fact that the scheme makes extensive use of a predictor stage based on a smooth wave equation, hence its behaviour in the presence of shockwaves cannot be taken for granted, and the filtering techniques for oscillations (Sections 3.2.3 and 3.2.5) require validation due to their critical importance in preventing spurious oscillations and potential crashes.

5.1. Single material Riemann problems

We begin the validation of the proposed numerical methodology by showing the behaviour of the method with varying mesh sizes and CFL values. To this purpose we select the simple Sod shock tube problem.

The method is then benchmarked against a much more stringent battery of tests, consisting of the Lax shock tube and the six problems given in the Toro's 2009 book [91]. These Riemann problems are designed to assess the accuracy and robustness of a numerical method with respect to shockwaves (both fast and slow moving) and strong rarefactions.

The general form of the initial condition is composed of two constant states separated by a sharp discontinuity located at the spatial coordinate x_d

$$\rho(t = 0,\ x),\ u(t = 0,\ x),\ p(t = 0,\ x) = \begin{cases}\rho_\mathrm{L},\ u_\mathrm{L},\ p_\mathrm{L} & \text{if } x \le x_\mathrm{d},\\ \rho_\mathrm{R},\ u_\mathrm{R},\ p_\mathrm{R} & \text{if } x > x_\mathrm{d},\end{cases} \tag{72}$$

where the parametric quantities $\rho_\mathrm{L},\ u_\mathrm{L},\ p_\mathrm{L},\ \rho_\mathrm{R},\ u_\mathrm{R},\ p_\mathrm{R}$ are listed in Table 1, together with the final simulation times t_end.

In Fig. 3 we show how the implicit Lagrangian method here proposed behaves on the simple Sod shock tube problem at different mesh resolutions ranging from $N = 250$ to $N = 16,000$ cells of equal mass. The Courant number is fixed by setting $k_\mathrm{CFL} = 10.0$. The main observations are that the contact is correctly captured without smearing (as expected from a Lagrangian scheme) and that

Table 1

Initial conditions for the single material Riemann problems. The table lists the left and right states, the domain extrema x_L and x_R, the initial position of the discontinuity x_d, and the final time t_{end}. In all cases, the material parameters are $\gamma_L = \gamma_R = 1.4$ and $\Pi_L = \Pi_R = 0.0$. As the rest of the paper, the table uses SI units.

	Sod	Lax	Toro1	Toro2	Toro3	Toro4	Toro5	Toro6
ρ_L	1.0	0.445	1.0	1.0	1.0	5.99924	1.0	1.0
u_L	0.0	0.698	0.75	−2.0	0.0	19.5975	−19.59745	2.0
p_L	1.0	3.528	1.0	0.4	1000.0	460.894	1000.0	0.1
ρ_R	0.125	0.5	0.125	1.0	1.0	5.99242	1.0	1.0
u_R	0.0	0.0	0.0	2.0	0.0	−6.19633	−19.59745	−2.0
p_R	0.1	0.571	0.1	0.4	0.01	46.095	0.01	0.1
x_L	0.0	0.0	0.0	0.0	0.0	−0.2	0.0	−2.1
x_d	0.5	0.5	0.4	0.5	0.5	0.5	0.6	0.0
x_R	1.0	1.0	1.0	1.0	1.0	1.2	1.0	2.1
t_{end}	0.25	0.1	0.2	0.15	0.012	0.035	0.012	0.8

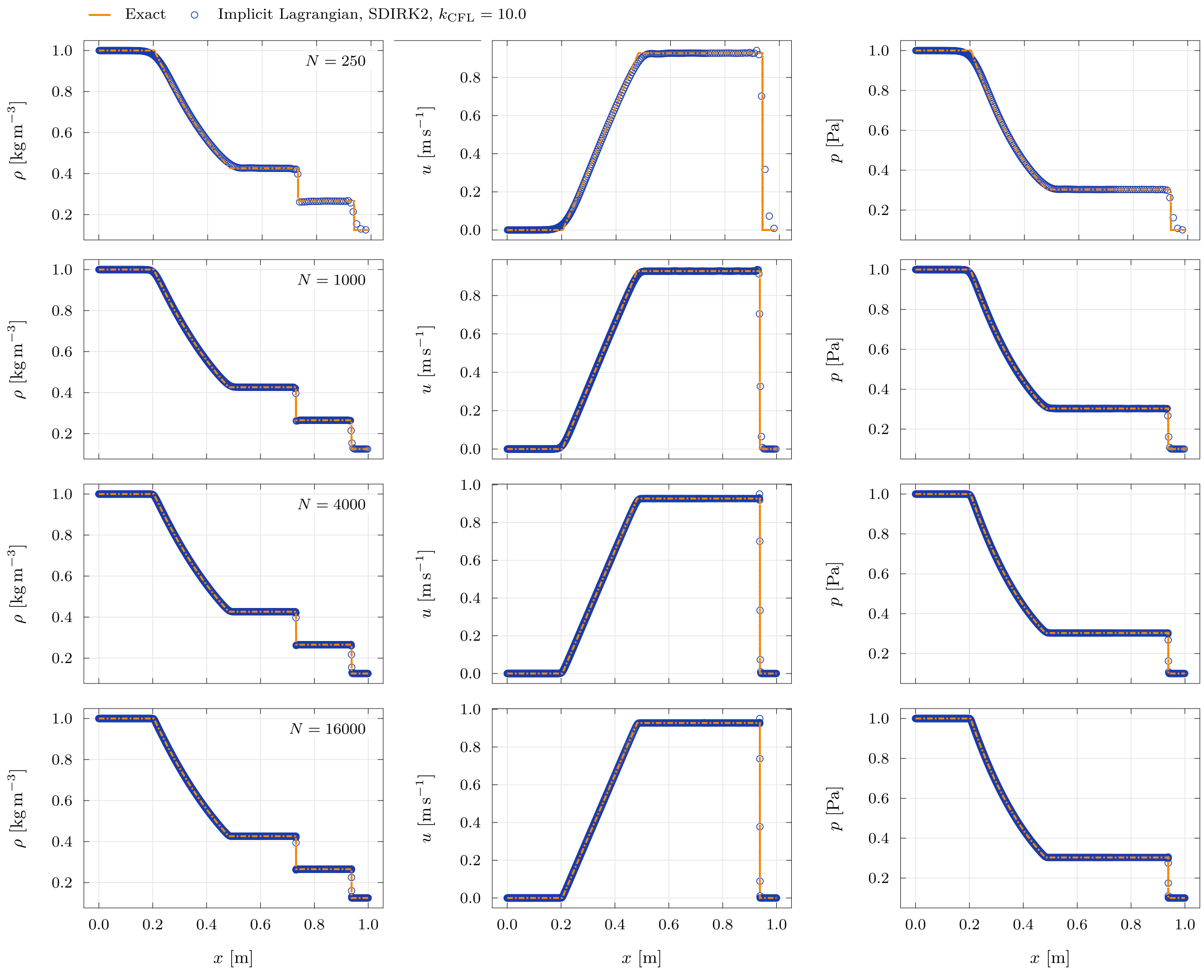

Fig. 3. Behaviour of the proposed implicit Lagrangian numerical method at different uniform mesh sizes, from $N = 250$ to $N = 16,000$ cells. The number of points found at contact (0 to 1) and at shocks (2–3) is largely independent of mesh resolution, like it would be for an explicit Lagrangian scheme. Major oscillations are absent, despite the relatively large CFL number ($k_{CFL} = 10.0$) and the presence of mild shockwaves. The simulations employ a second order diagonally implicit Runge–Kutta time integrator (SDIRK2).

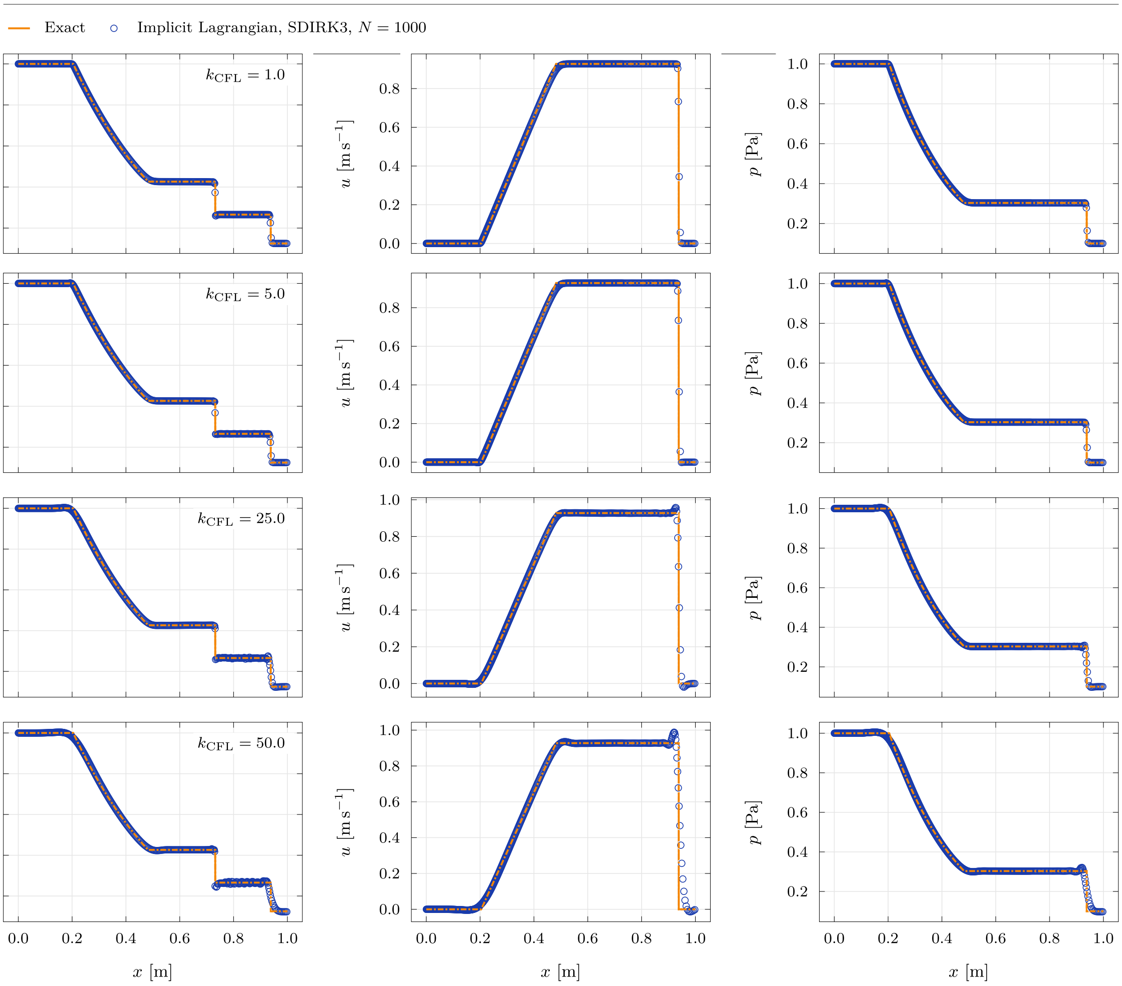

Fig. 4. Behaviour of the proposed implicit Lagrangian numerical method at different CFL values, ranging from $k_{\mathrm{CFL}} = 1.0$ to $k_{\mathrm{CFL}} = 50.0$. The first timestep of the simulations at $k_{\mathrm{CFL}} = 25.0$ and $k_{\mathrm{CFL}} = 50.0$ uses $k^0_{\mathrm{CFL}} = k_{\mathrm{CFL}}/10$. Some oscillations and additional artificial diffusion appear for the higher CFL numbers but the overall structure of the solution is well preserved. The simulations employ a third order diagonally implicit Runge–Kutta time integrator (SDIRK3) and a constant-mass mesh of $N = 1000$ cells. The run at $k_{\mathrm{CFL}} = 50.0$ is carried out in 16 timesteps.

the shockwave is always spread over two mesh points despite the increased Courant number with respect to what standard explicit time-‘stepping would prescribe.

Analogously, in Fig. 4 we fix the mesh size to $N = 1000$ uniform mass cells and let the Courant number vary between $k_{\mathrm{CFL}} = 1.0$ and $k_{\mathrm{CFL}} = 50.0$. For the tests at $k_{\mathrm{CFL}} = 25.0$ and $k_{\mathrm{CFL}} = 50.0$, we ramp up the timestep starting from $k^0_{\mathrm{CFL}} = k_{\mathrm{CFL}}/10$ and increasing linearly over ten timesteps. This means that the computation of Sod's problem in the last row of Fig. 4 has been carried out over 16 timesteps, for a mesh size of $N = 1000$ uniform mass cells. This is a slight variation on the practical recommendation given in Toro's book [91] about the choice of step size for the early stages of a numerical simulation involving discountinuous initial data. In this case, instead of choosing a reduced size for the first, say, five timesteps, we gradually increase the timestep from a small initial value k^0_{CFL} to the full value k_{CFL} in a linear fashion, so that the time integrator does not see abrupt jumps in the step size. As the timestep size increases, we see that both nonlinear waves are subject to additional numerical diffusion, with the contact remaining sharp and some oscillations can be observed especially for what concerns the velocity of the fluid at the shock front. Nonetheless, the computations did not fail due to positivity violations.

Next, we carry out Lax's problem and the battery of benchmarks that can be found in Toro's 2009 book [91]. These test problems are aimed at assessing the robustness and accuracy of numerical methods for the compressible Euler equations in a variety of scenarios. The problems are labelled Toro1 to Toro6. Toro1 is a modified version of Sod's problem, where a sonic point is present in the left moving rarefaction. In Fig. 5 we report the results of the classic Lax problem and of the Toro1 sonic rarefaction problem, using the proposed implicit Lagrangian scheme with SDIRK2 time integration over a mesh of 1000 constant mass cells. Contacts are sharp and no sonic glitch or other spurious artifacts are observed, with the Courant numbers ($k_{\mathrm{CFL}} = 2.0$ and $k_{\mathrm{CFL}} = 4.0$ respectively) exceeding those prescribed by explicit schemes, despite the presence of shockwaves.

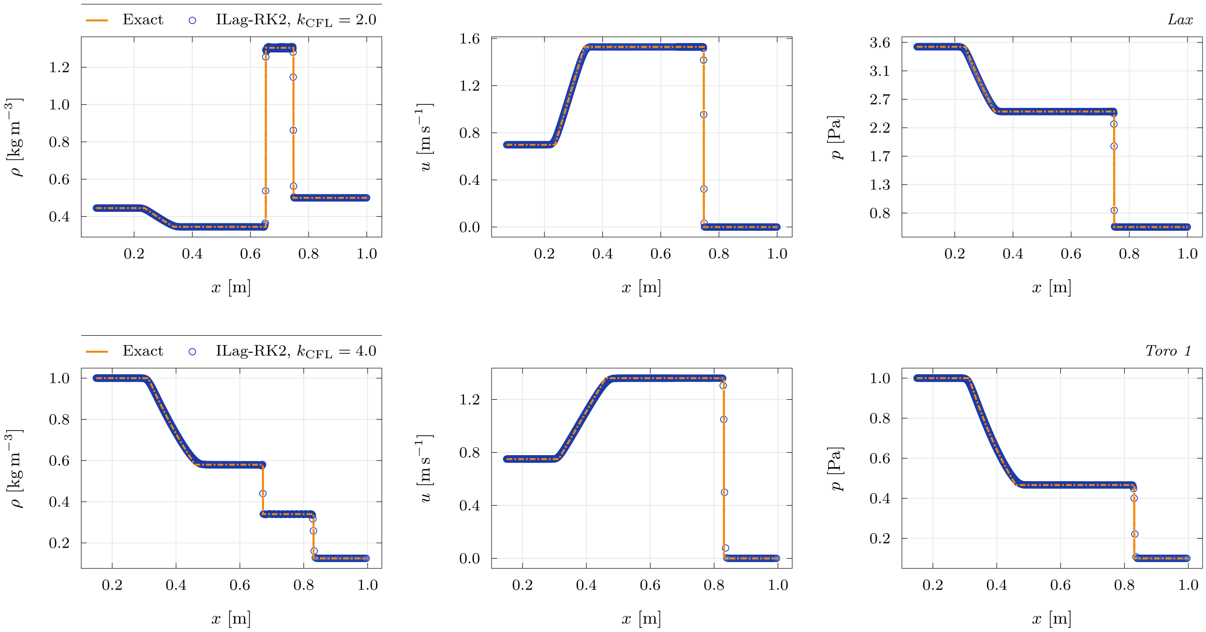

Fig. 5. Numerical results for the Lax shock tube problem and for the modified Sod problem with transsonic rarefaction (Toro 1). The simulations employ a second order diagonally implicit Runge–Kutta time integrator (SDIRK2) and a constant-mass mesh of $N = 1000$ cells.

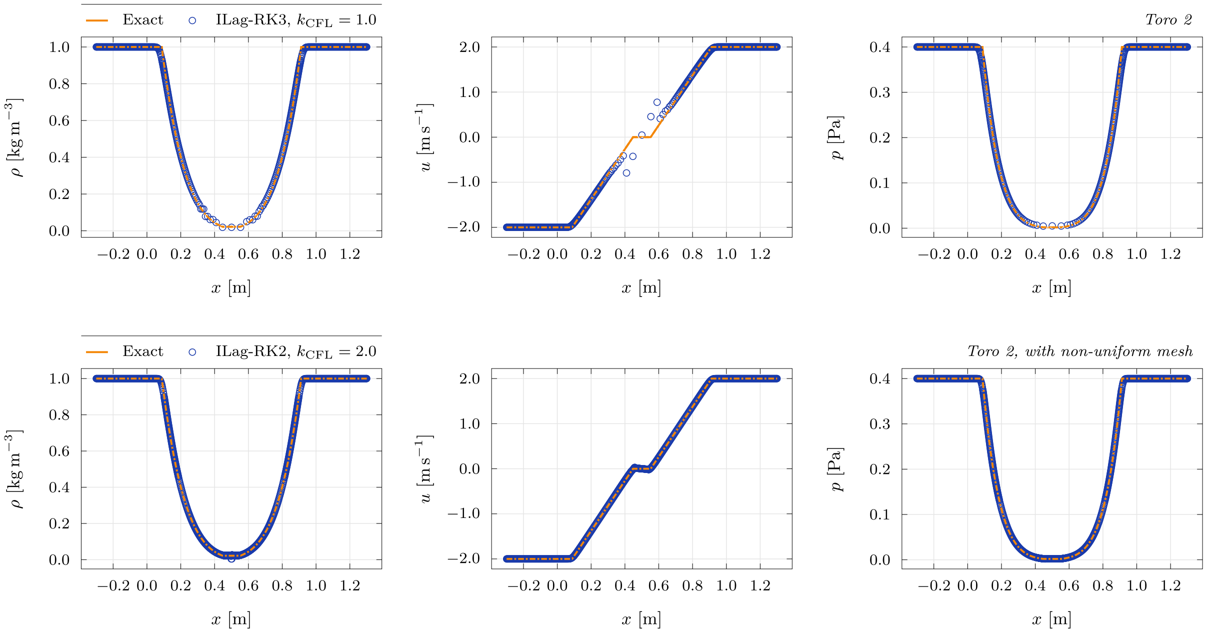

Fig. 6. Numerical results for the second problem of Toro (also known as 123 problem) involving two strong rarefactions generating a near-vacuum central state. The uniform mesh of $N = 1000$ cells is expands with the rarefactions, causing inaccurate results in the central portion of the domain. In the bottom panels, we show the results obtained using a finer non-uniform mesh of $N = 2000$ cells, which accommodates the expansion effect. The simulations employ a second order diagonally implicit Runge–Kutta time integrator (SDIRK2).

In Fig. 6, we plot the numerical results obtained for the so-called 123-problem (labelled Toro2 here). The problem features two strong symmetrical rarefaction waves giving rise to a very low density central state. In the upper panels we present the numerical results obtained with a uniform mesh in the mass coordinate with 1000 cells. It appears that the low density central region is poorly resolved, therefore the numerical solution is not accurate there. The lower panels are obtained adopting a slightly finer grid of 2000 elements which are initially denser towards the center of the computational domain, thus providing a much more accurate solution.

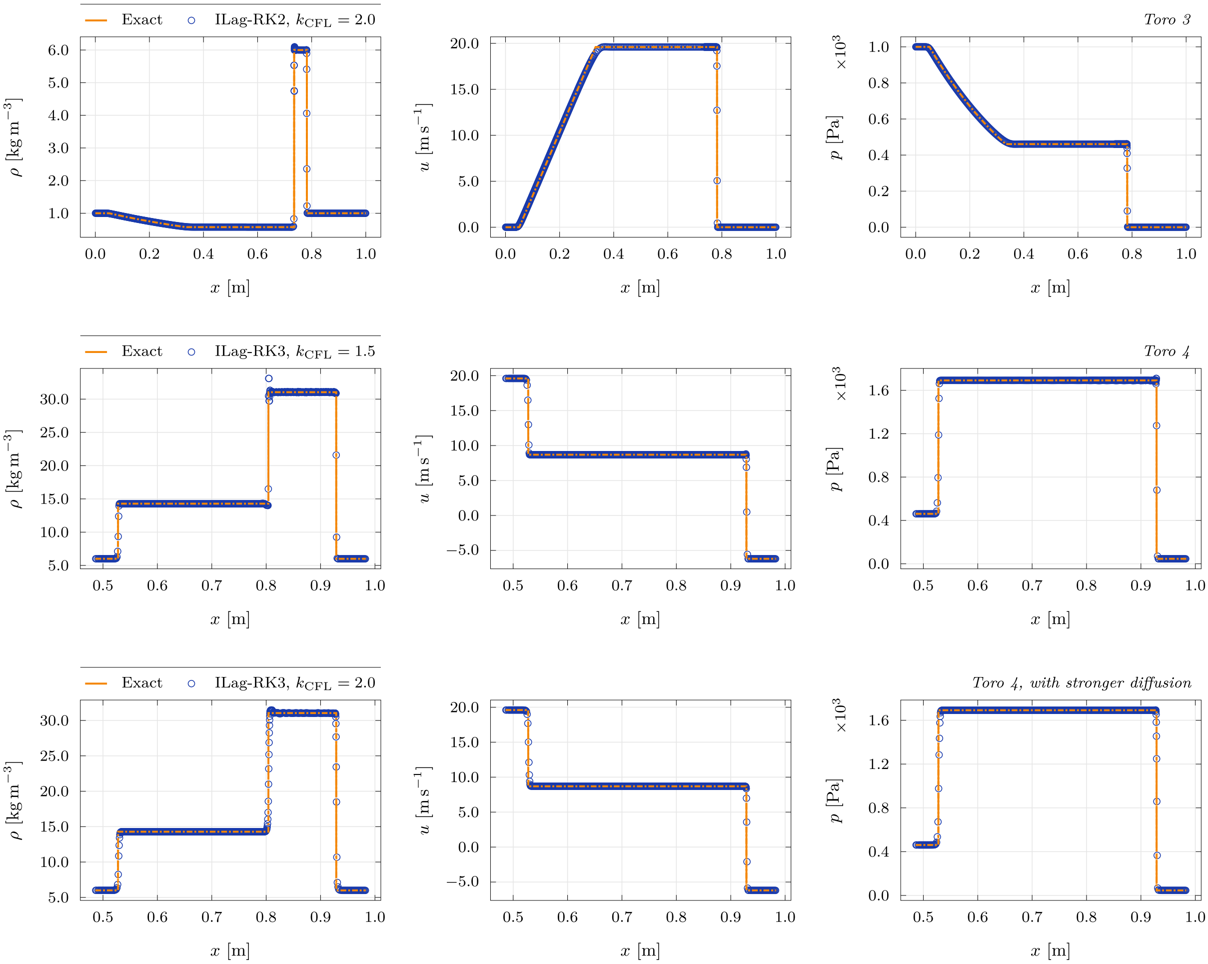

Fig. 7. Numerical results for the third (first row) and fourth (second and third row) problems of Toro, obtained via the proposed implicit Lagrangian method with second or third order diagonally implicit Runge–Kutta time integration (SDIRK2 or SDIRK3), labelled ILag-RK2 and ILag-RK3 respectively. All simulations use a constant-mass mesh of $N = 1000$ cells. For the Toro4 problem, the contact discontinuity presents some spurious oscillations and in the bottom panels we show the results obtained with a much more diffusive variant of the regularisation operator for specific volume.

The robustness of the proposed discretization is then tested on the Toro3 and Toro4 Riemann problems. In the first row of Fig. 7 we can observe that the contact wave of the Toro3 problem is affected by some small spurious oscillations at $k_{\rm CFL} = 2$, and even more so in the second row for what concerns the Toro4 problem at $k_{\rm CFL} = 1.5$. In this latter test, the oscillations are pronounced enough to warrant the use of stronger numerical dissipation on the density/specific volume, which successfully controls the size of the oscillations, but at the price of losing exactly sharp contact discontinuities, as can be observed in the third row of Fig. 7.

Similar observations can be given with regards to the results of the Toro5 and Toro6 tests shown in Fig. 8: at $k_{\rm CFL} = 2.5$, some mild oscillations are deteriorating the contact wave and the base of the rarefaction in the Toro5 problem, and strong density artifacts can be observed in the center of Toro6 problem at $k_{\rm CFL} = 3.0$, which is nothing but two colliding shocks, where usually wall heating effects are observed. In [48], a semi-implicit scheme running at $k_{\rm CFL} = 0.5$ was shown to produce a wall cooling effect instead. As done for the Toro4 problem, additional numerical diffusion in the density, and a reduction of the Courant number to $k_{\rm CFL} = 1.5$ can reduce these oscillations, while of course at the same time smearing all waves a little bit more.

5.2. Convergence results

We validate the convergence properties and order of accuracy of the proposed method by comparing its results with those of a reference solution obtained on a very fine grid by means of a standard explicit Finite Volume method. The test problem is chosen in such a way that the solution can be considered smooth until the final time, but also making sure that the effects of the nonlinearity of the governing equations are highlighted by the test, hence making sure that the presented convergence results are not only valid for small amplitude waves.

$$\rho(t=0,\ x) = \rho_0, \qquad u(t=0,\ x) = u_0, \qquad p(t=0,\ x) = p_0\left\{1 + 10\,\exp\left[-(x-x_0)^2/\ell^2\right]\right\}, \tag{73}$$

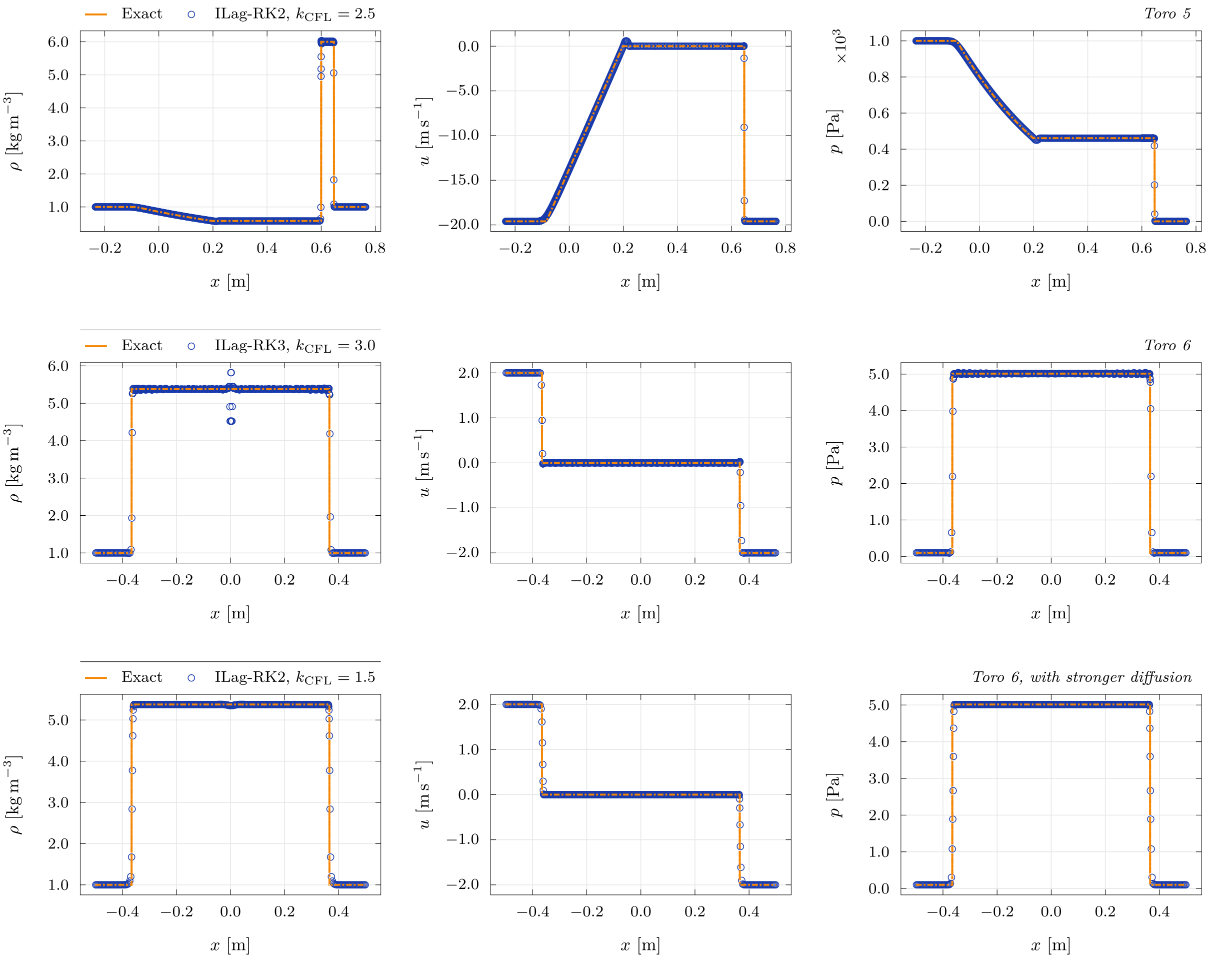

Fig. 8. Numerical results for the fifth (first row) and sixth (second and third row) problems of Toro, obtained via the proposed implicit Lagrangian method with second or third order diagonally implicit Runge–Kutta time integration (SDIRK2 or SDIRK3), labelled ILag-RK2 and ILag-RK3 respectively. All simulations use a constant-mass mesh of $N = 1000$ cells. For the Toro6 problem, oscillations due to well known wall heating/cooling effecs are present. The issue can be mitigated by adopting a more aggressive numerical diffusion for the specific volume, as shown in the bottom panels.

with $\rho_0 = 2.0\,\mathrm{kg\,m^{-3}}$, $u_0 = 0.0\,\mathrm{m\,s^{-1}}$, $p_0 = 0.1\,\mathrm{Pa}$, $\ell = 0.075\,\mathrm{m}$, constant (single-material) parameters for the stiffened gas equation of state $\gamma_1 = \gamma_2 = \gamma = 1.4$, $\Pi_1 = \Pi_2 = \Pi = 0.5\,\mathrm{Pa}$. Note that, while we express these quantities with SI units, the parameters and reference states for this problem have been chosen in such a way to highlight the nonlinear behaviour of the PDE system, in particular, obtaining significant deviations from the quasi-linear regime of small perturbations and obtain nonlinear wave steepening.

The simulation domain is $x \in [0,\ 1]$ and the final time $t_{\mathrm{end}} = 0.2\,\mathrm{s}$ is chosen such that the data can be seen as smooth when sampled at the considered mesh resolutions (ranging between $N = 100$ and $N = 204,800$ cells), while at the same time significant wave steepening effects are observed.

The results of Fig. 9 can be used to quantify the wave steepening effects and how the solution is captured at $k_{\mathrm{CFL}} = 1.0$ with $N = 100$ cells and at $k_{\mathrm{CFL}} = 200.0$ with $N = 10,000$ cells, in which case the solution is marched to the final time $t_{\mathrm{end}} = 0.2\,\mathrm{s}$ in 10 timesteps. We also report the corresponding error norms and experimental orders of convergence in Table 2, where no piecewise linear reconstruction was used, yielding a scheme of first order spatial accuracy, and in Table 3, where a minmod-limited piecewise linear reconstruction is employed in order to compute the artificial diffusion for energy. A graphical rendition of the same data can be found in Fig. 10. When the piecewise linear reconstruction is used for the computation of artificial diffusion on energy, second order of convergence is experimentally verified, given sufficiently fine meshes that allow to resolve all the features of the flow as smooth. If the data reconstruction is not used, one would expect to achieve only first order of accuracy, and indeed at $k_{\mathrm{CFL}} = 1$, this is what we find. When using very large timesteps ($k_{\mathrm{CFL}} = 20$, $k_{\mathrm{CFL}} = 100$) however, convergence slopes closer to 2 are found. Note that in Table 2 and Fig. 10, at sufficiently high CFL numbers, the scheme converges with accuracy higher than 1, despite the fact that the spatial discretization in these cases is only first order accurate. This is simply due to the fact that with large timesteps, the temporal discretization error has become the dominant one in this test problem. Moreover, it is often the case that application to systems with

Table 2

Convergence results for the proposed implicit method, using the first order diffusion operator for the total energy. In the table are shown the L^1, L^2, and L^∞ norms of the error on the specific total energy E and the corresponding convergence rates, for two different implicit time integration schemes (SDIRK2 and SDIRK3) and with varying choices of k_{CFL}. Note that the convergence rates for the higher CFL numbers approach 2, despite the underlying spatial discretization being of first order, since at high CFL numbers the temporal discretisation error was found to be the dominant one in this case.

	N	$\mathcal{E}_{L^1}$	$\mathcal{E}_{L^2}$	$\mathcal{E}_{L^\infty}$	$\mathcal{O}_{L^1}$	$\mathcal{O}_{L^2}$	$\mathcal{O}_{L^\infty}$
SDIRK3	100	4.32×10^{-3}	6.06×10^{-3}	2.26×10^{-2}	–	–	–
$k_{\mathrm{CFL}} = 1.0$	400	9.62×10^{-4}	1.70×10^{-3}	8.52×10^{-3}	1.08	0.92	0.70
	1600	2.34×10^{-4}	4.44×10^{-4}	2.59×10^{-3}	1.02	0.97	0.86
	6400	5.80×10^{-5}	1.13×10^{-4}	6.79×10^{-4}	1.01	0.99	0.96
	25,600	1.45×10^{-5}	2.83×10^{-5}	1.72×10^{-4}	1.00	1.00	0.99
SDIRK2	100	4.03×10^{-3}	5.44×10^{-3}	1.95×10^{-2}	–	–	–
$k_{\mathrm{CFL}} = 1.0$	400	9.34×10^{-4}	1.62×10^{-3}	7.91×10^{-3}	1.05	0.88	0.65
	1600	2.32×10^{-4}	4.38×10^{-4}	2.53×10^{-3}	1.01	0.94	0.82
	6400	5.79×10^{-5}	1.12×10^{-4}	6.75×10^{-4}	1.00	0.98	0.95
	25,600	1.45×10^{-5}	2.82×10^{-5}	1.72×10^{-4}	1.00	1.00	0.99
SDIRK2	100	2.30×10^{-2}	2.55×10^{-2}	4.92×10^{-2}	–	–	–
$k_{\mathrm{CFL}} = 20.0$	400	7.21×10^{-3}	9.94×10^{-3}	2.94×10^{-2}	0.84	0.68	0.37
	1600	8.29×10^{-4}	1.68×10^{-3}	8.73×10^{-3}	1.56	1.28	0.88
	6400	6.10×10^{-5}	1.50×10^{-4}	9.77×10^{-4}	1.88	1.75	1.58
	25,600	1.17×10^{-5}	2.25×10^{-5}	1.43×10^{-4}	1.19	1.36	1.39
	102,400	3.44×10^{-6}	6.59×10^{-6}	3.95×10^{-5}	0.88	0.89	0.93
SDIRK2	800	1.69×10^{-2}	2.08×10^{-2}	4.58×10^{-2}	–	–	–
$k_{\mathrm{CFL}} = 100.0$	3200	3.87×10^{-3}	6.11×10^{-3}	2.25×10^{-2}	1.06	0.88	0.51
	12,800	3.87×10^{-4}	9.08×10^{-4}	5.54×10^{-3}	1.66	1.38	1.01
	51,200	2.55×10^{-5}	7.45×10^{-5}	6.03×10^{-4}	1.96	1.80	1.60
	204,800	1.66×10^{-6}	4.15×10^{-6}	2.75×10^{-5}	1.97	2.08	2.23

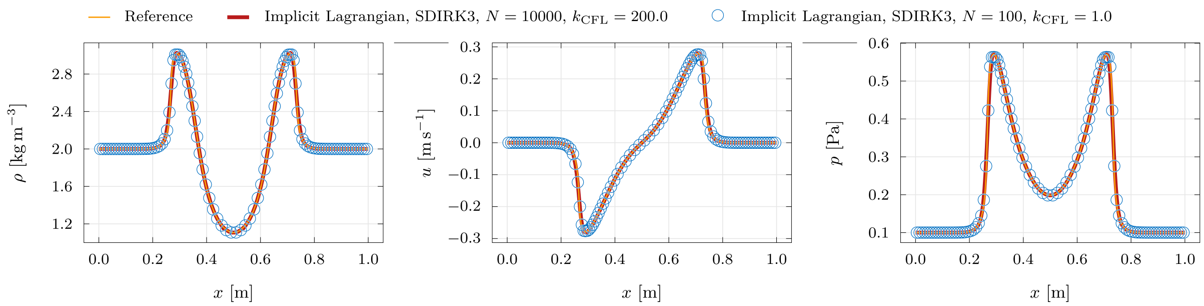

Fig. 9. Numerical solutions at time $t = 0.2$ s for the smooth convergence benchmark. In the three panels are shown the profiles of density, velocity, and pressure computed by the proposed implicit Lagrangian method using two different choices of mesh and timestep size, compared with a reference solution obtained with an Eulerian MUSCL–Hancock scheme on a fine mesh of 200,000 uniform cells. The reference solution is accurately reproduced with $N = 100$ uniform mass cells, and on finer grids with high CFL number ($N = 10,000$ cells, $k_{\mathrm{CFL}} = k^0_{\mathrm{CFL}} = 200$, 10 timesteps total).

many layers end up using very large cell counts simply to represent with some detail the layered structure of the medium, precisely leading to situations in which a significant benefit can be gained from the use of higher order temporal integrators.

Based on the results of this study, we also carried out an efficiency study to estimate the computational expense of the proposed method. Generally, when using implicit schemes, one expects to spend more computational time per Runge–Kutta stage with respect to an explicit method, but such higher per-stage cost is offset by the fact that the implicit scheme can carry out much larger timesteps. In our case, we compare the proposed implicit Lagrangian method with a reference explicit Lagrangian method, which makes use of low dissipation reconstruction (a low-diffusion generalized MinMod limiter, see Kurganov and Tadmor [90]), together with the exact Riemann solver, in order to match the resolution of the proposed scheme. In our naive Fortran implementation, which does *not* explicitly make use of vector instructions, the implicit method requires less computational time than the explicit one even when the timestep size is matched. This is due to the fact that the explicit method relies on the rather expensive exact Riemann solver, while the implicit scheme is indeed iterative but its implicit part is solved by means of the Thomas algorithm and for this reason does not carry the same cost usually associated with implicit methods. Extension to (nonlinear) equations of state more complex than the stiffened gas EOS can be carried out with the aid of the method by Casulli and Zanolli [92]. The use of the exact Riemann solver as a comparison is justified by the fact that for this smooth test problem, the reference explicit scheme at $k_{\mathrm{CFL}} = 0.8$ yields numerical errors which are still slightly higher than those obtained with the Implicit Lagrangian method in the Courant range between $k_{\mathrm{CFL}} = 0.5$ and $k_{\mathrm{CFL}} = 2.0$. The result shows that the method can achieve minimum error not only at $k_{\mathrm{CFL}} = 1$ but in a range around it, and more

Table 3

Convergence results for the proposed implicit method, using the second order diffusion operator for the total energy. In the table are shown the L^1, L^2, and L^∞ norms of the error on the specific total energy E and the corresponding convergence rates, for two different implicit time integration schemes (SDIRK2 and SDIRK3) and with varying choices of k_{CFL}. The error norms relative to standard explicit Lagrangian scheme with exact Riemann solver and second order generalized minmod reconstruction and SSPRK2 or SSPRK3 time integration ($k_{\mathrm{CFL}} = 0.8$) are shown for comparison.

	N	$\mathcal{E}_{L^1}$	$\mathcal{E}_{L^2}$	$\mathcal{E}_{L^\infty}$	$\mathcal{O}_{L^1}$	$\mathcal{O}_{L^2}$	$\mathcal{O}_{L^\infty}$
SDIRK3	100	1.12×10^{-3}	1.62×10^{-3}	5.49×10^{-3}	–	–	–
$k_{\mathrm{CFL}} = 1.0$	400	8.19×10^{-5}	1.43×10^{-4}	6.57×10^{-4}	1.89	1.75	1.53
	1600	5.94×10^{-6}	1.26×10^{-5}	1.02×10^{-4}	1.89	1.75	1.34
	6400	3.88×10^{-7}	9.34×10^{-7}	9.08×10^{-6}	1.97	1.88	1.74
	25,600	2.42×10^{-8}	6.25×10^{-8}	6.94×10^{-7}	2.00	1.95	1.85
Ref. Explicit SSPRK3	25,600	3.25×10^{-8}	9.32×10^{-8}	8.20×10^{-7}	–	–	–
SDIRK2	100	1.13×10^{-3}	1.48×10^{-3}	3.34×10^{-3}	–	–	–
$k_{\mathrm{CFL}} = 1.0$	400	9.52×10^{-5}	1.99×10^{-4}	1.30×10^{-3}	1.79	1.45	0.68
	1600	6.61×10^{-6}	1.77×10^{-5}	1.67×10^{-4}	1.92	1.75	1.48
	6400	4.32×10^{-7}	1.22×10^{-6}	1.31×10^{-5}	1.97	1.93	1.84
	25,600	2.71×10^{-8}	8.04×10^{-8}	9.06×10^{-7}	2.00	1.96	1.93
Ref. Explicit SSPRK2	25,600	5.95×10^{-8}	1.81×10^{-7}	1.59×10^{-6}	–	–	–
SDIRK2	100	2.52×10^{-2}	2.85×10^{-2}	5.36×10^{-2}	–	–	–
$k_{\mathrm{CFL}} = 20.0$	400	8.02×10^{-3}	1.11×10^{-2}	3.23×10^{-2}	0.83	0.68	0.36
	1600	9.65×10^{-4}	2.01×10^{-3}	1.04×10^{-2}	1.53	1.23	0.82
	6400	7.10×10^{-5}	2.01×10^{-4}	1.53×10^{-3}	1.88	1.66	1.38
	25,600	4.47×10^{-6}	1.36×10^{-5}	1.16×10^{-4}	1.99	1.94	1.86
	102,400	2.81×10^{-7}	8.56×10^{-7}	7.32×10^{-6}	2.00	2.00	1.99
SDIRK2	800	1.74×10^{-2}	2.13×10^{-2}	4.66×10^{-2}	–	–	–
$k_{\mathrm{CFL}} = 100.0$	3200	3.97×10^{-3}	6.28×10^{-3}	2.30×10^{-2}	1.07	0.88	0.51
	12,800	4.03×10^{-4}	9.51×10^{-4}	5.79×10^{-3}	1.65	1.36	0.99
	51,200	2.79×10^{-5}	8.31×10^{-5}	6.75×10^{-4}	1.93	1.76	1.55
	204,800	1.75×10^{-6}	5.32×10^{-6}	4.55×10^{-5}	2.00	1.98	1.95

over such minimum error is lower than that given by the reference scheme using a little-dissipative reconstruction limiter and the exact Riemann solver.

The implicit scheme is then favorable as a practical alternative to the explicit one, given that no extra computational cost is associated with its use, and at the same time the user can choose to use much larger timesteps if as needed. In light of the results of Section 5.1, we can however see that an explicit method might still be preferable for problems involving very strong shockwaves.

5.3. Two material Riemann problems

A series of classic two-material Riemann problems are used to evaluate the performance of the proposed implicit Lagrangian method. The results here shown extend the validation of the proposed scheme to systems where the material properties are allowed to jump across cell interfaces. To this purpose we reproduce the results of Abgrall and Karni, which involve material interfaces with significant differences in density and compressibility between adjacent layers.

The initial conditions are simply given by

$$\rho(t=0,\ x),\ u(t=0,\ x),\ p(t=0,\ x),\ \gamma(x),\ \Pi(x) = \begin{cases} \rho_{\mathrm{L}},\ u_{\mathrm{L}},\ p_{\mathrm{L}},\ \gamma_{\mathrm{L}},\ \Pi_{\mathrm{L}} & \text{if } x \le x_{\mathrm{d}}, \\ \rho_{\mathrm{R}},\ u_{\mathrm{R}},\ p_{\mathrm{R}},\ \gamma_{\mathrm{R}},\ \Pi_{\mathrm{R}} & \text{if } x > x_{\mathrm{d}}, \end{cases} \tag{74}$$

for three separate choices of initial data and material parameters, as listed in Table 4. The first test, labelled AK1, is a variant of Sod's problem and is tested at $k_{\mathrm{CFL}} = 10.0$, while the second (AK2) is a more violent shock tube, for which we ran the simulation at $k_{\mathrm{CFL}} = 2.0$. The third test (AK3) features a strong pressure jump and the CFL number was set to $k_{\mathrm{CFL}} = 4.0$.

The results of the tests labelled AK1 and AK2 use a uniform mesh of $N = 1000$ cells (in mass space) are reported in Fig. 12, which also contains the results of test AK3, where a quasi-uniform mesh of $N = 1000$ cells (in physical space) is used. This choice was made to provide a better distribution of the resolution of the scheme, since the density ratio of the test would yield a mesh with very few cells in the lighter right side, if a mass-uniform mesh were employed.

The results match the analytical solutions of the two-material Riemann problems and show limited spurious oscillations, despite the fact that the used CFL numbers always exceed unity, and in particular the density and pressure oscillations (shown in log-scale in the third row of Fig. 12) have acceptable amplitudes. In the last row of Fig. 12, a magnification square has been added to better show small discontinous contact feature of the density profile in the vicinity of the shock front. The comparison with the analytical solutions does not show particularly severe issues.

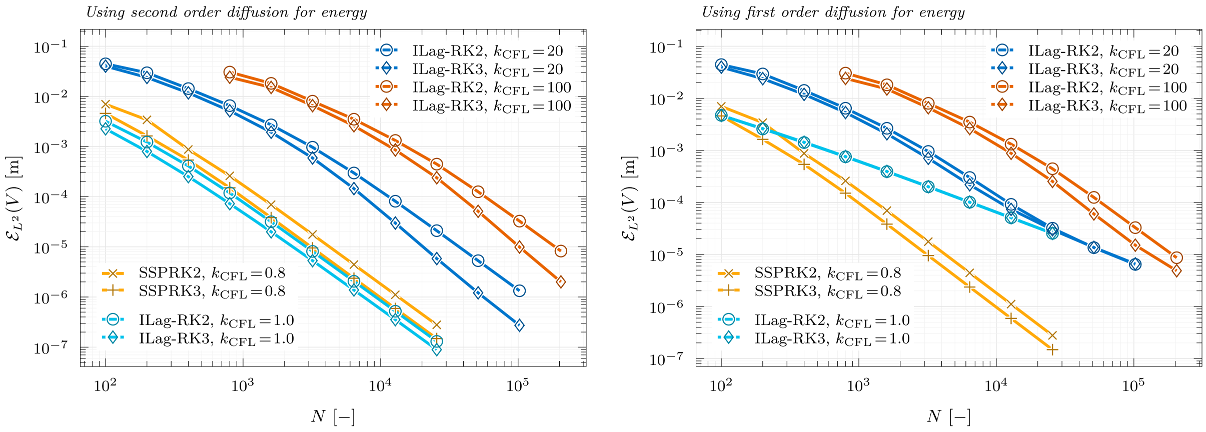

Fig. 10. Bilogarithmic plots of the L^2 error norms given by the proposed implicit Lagrangian method for the specific volume variable V using different time integration schemes (second and third order SDIRK, labelled ILag-RK2 and ILag-RK3 respectively) and different timestep sizes (from $k_{\mathrm{CFL}} = k^0_{\mathrm{CFL}} = 1$ to $k_{\mathrm{CFL}} = k^0_{\mathrm{CFL}} = 100$). The error norms given by a standard explicit second order Lagrangian scheme using SSP Runge–Kutta time integration (SSPRK2 and SSPRK3) are included for comparison. On the left, the implicit schemes use the second order energy diffusion operator and second order convergence rates are obtained at all CFL numbers for sufficiently fine meshes. On coarse meshes with high CFL number, lower convergence rates are observed because the simulations are completed in too few timesteps: for example at $k_{\mathrm{CFL}} = 100$ the simulation with 800 grid points consists of two timesteps. At unit CFL, the errors of the implicit Lagrangian method are lower than those of the explicit reference scheme. In the right panel, we show the results obtained without the low-diffusion correction on energy: at low CFL, or for very coarse meshes the order of convergence degenerates to 1 (as expected), but for higher CFL numbers such an effect is negligible and observed errors are similar to those obtained with the second order numerical diffusion operator.

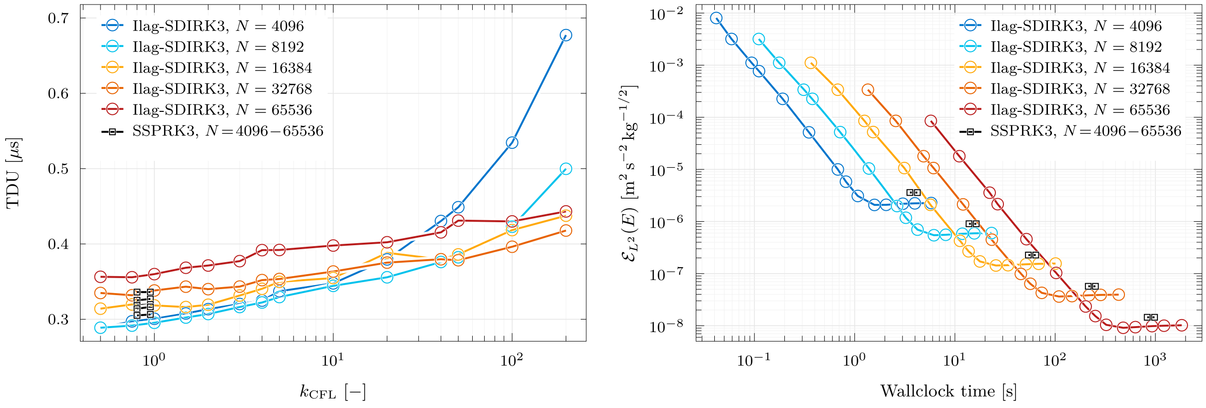

Fig. 11. Performance measurements. In the left panel, computational times per degree of freedom update per Runge–Kutta stage (TDU) as a function of the CFL number, for mesh sizes ranging from $N = 4096$ to $N = 65,536$, compared with the corresponding timing of the explicit scheme. While the CFL number ranges more than two orders of magnitude, the time per stage grows at most by a factor of 3, and is almost constant for sufficiently fine meshes. In the right panel, the L^2 error norms for the total energy are plotted as a function of the wallclock time, which depends on k_{CFL}, ranging here between $k_{\mathrm{CFL}} = 0.5$ (more timestep, longer wallclock time) and $k_{\mathrm{CFL}} = 200$ (fewer timeteps, shorter computations). For all mesh sizes, the proposed method achieves better results than the explicit reference scheme using an exact Riemann solver (at $k_{\mathrm{CFL}} = 0.8$ and $k_{\mathrm{CFL}} = 0.95$). The plots also show that the same error norms can be obtained with significantly shorter computational times, selecting for example $k_{\mathrm{CFL}} = 2.0$.

Table 4
Initial conditions for the two-material Riemann problems. The table lists the left and right states, the material parameters for the two regions and the final time t_{end}. In all cases, the domain extrema are $x_{\mathrm{L}} = 0.0$ and $x_{\mathrm{R}} = 1.0$ and the initial position of the discontinuity is $x_{\mathrm{d}} = 0.5$. As the rest of the paper, the table uses SI units.

	ρ_{L}	u_{L}	p_{L}	ρ_{R}	u_{R}	p_{R}	γ_{L}	Π_{L}	γ_{R}	Π_{R}	t_{end}
AK1	1.0	0.0	1.0	0.125	0.0	0.1	1.6	0.0	1.2	0.0	0.25
AK2	1.0	0.0	500.0	1.0	0.0	0.2	1.4	0.0	1.6	0.0	0.015
AK3	1000.0	0.0	10^9	50.0	0.0	10^5	4.4	6×10^8	1.4	0.0	1.5×10^{-4}

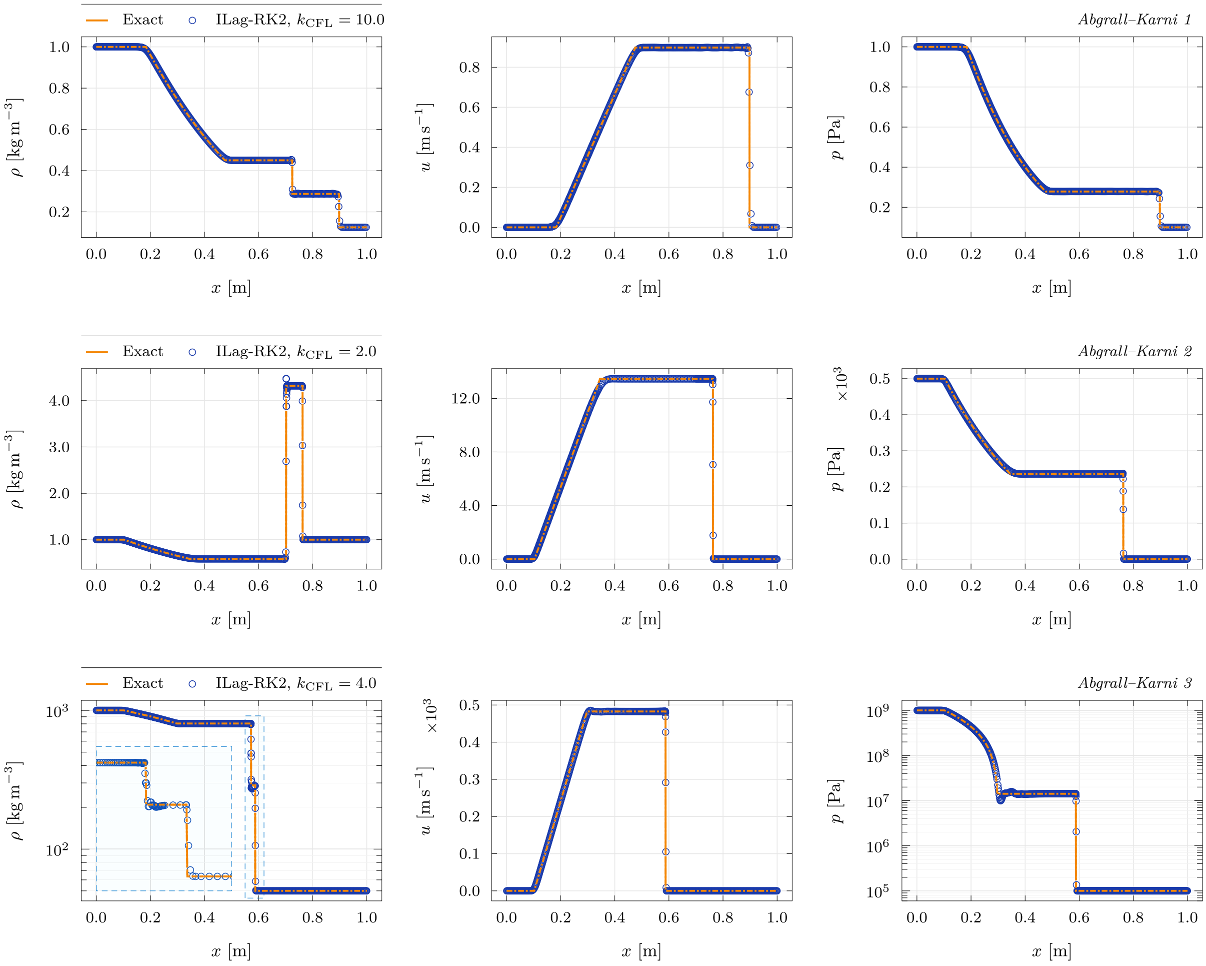

Fig. 12. Numerical results for the multi-material Riemann problems of Abgrall and Karni, obtained using the proposed implicit Lagrangian method with second order diagonally implicit Runge–Kutta time integration (SDIRK2). The first two problems use a uniform-mass mesh of $N = 1000$ cells, while the third, due to the large density ratio, adopts a smoothed quasi-uniform mesh in Δx, also composed of $N = 1000$ cells. In the leftmost panel of the third row, a magnification window has been added to better display the behaviour of the contact discontinuity found in the immediate vicinity of the shock front.

5.4. *One-dimensional shock–bubble interaction*

Further testing of the implicit Lagrangian scheme has been carried out by reproducing the results of Quirk and Karni [93] on a one-dimensional shock–bubble interaction problem (Fig. 13). The solution obtained with the proposed implicit Lagrangian scheme and third order diagonally implicit Runge–Kutta time-stepping, using the second-order energy diffusion operator, on $N = 2000$ uniformly spaced mesh points (i.e. with non-uniform mass Δm) at $k_{\mathrm{CFL}} = 5.0$, visually overlaps the reference given by an explicit Eulerian MUSCL–Hancock method with 50,000 uniform cells. No significant artifacts are visible in the under-resolved solution using $N = 100$ points at $k_{\mathrm{CFL}} = 10$, while adequately capturing all flow features.

$$\rho(t=0,\ x),\ u(t=0,\ x),\ p(t=0,\ x), \gamma(x) = \begin{cases} \rho_{\mathrm{L}},\ u_{\mathrm{L}},\ p_{\mathrm{L}},\ \gamma_1 & \text{if } x \leq x_0, \\ \rho_{\mathrm{R}},\ u_{\mathrm{R}},\ p_{\mathrm{R}},\ \gamma_1 & \text{if } x > x_0 \text{ and } x \leq x_1, \\ \rho_{\mathrm{B}},\ u_{\mathrm{B}},\ p_{\mathrm{B}},\ \gamma_2 & \text{if } x > x_1 \text{ and } x \leq x_2, \\ \rho_{\mathrm{R}},\ u_{\mathrm{R}},\ p_{\mathrm{R}},\ \gamma_1 & \text{if } x > x_2, \end{cases} \tag{75}$$

The states are specified by $\rho_{\mathrm{L}} = 1.3765\,\mathrm{kg\,m^{-3}}$, $\rho_{\mathrm{R}} = 1.0\,\mathrm{kg\,m^{-3}}$, $\rho_{\mathrm{B}} = 0.138\,\mathrm{kg\,m^{-3}}$, $u_{\mathrm{L}} = 0.2948\,\mathrm{m\,s^{-1}}$, $u_{\mathrm{R}} = u_{\mathrm{B}} = 0.0\,\mathrm{m\,s^{-1}}$, $p_{\mathrm{L}} = 1.57\,\mathrm{Pa}$, and $p_{\mathrm{R}} = p_{\mathrm{B}} = 1.0\,\mathrm{Pa}$. The computational domain is delimited by $x_{\mathrm{L}} = 0.0\,\mathrm{m}$ and $x_{\mathrm{R}} = 1.0\,\mathrm{m}$. The initial shock position is $x_0 = 0.25\,\mathrm{m}$ and the initial position of the one-dimensional bubble is delimited by $x_1 = 0.4\,\mathrm{m}$ and $x_2 = 0.6\,\mathrm{m}$. The test adopts the ideal gas law with $\gamma_1 = 1.4$ and $\gamma_2 = 1.67$, hence in practice we also set $\Pi_1 = \Pi_2 = 0.0\,\mathrm{Pa}$.

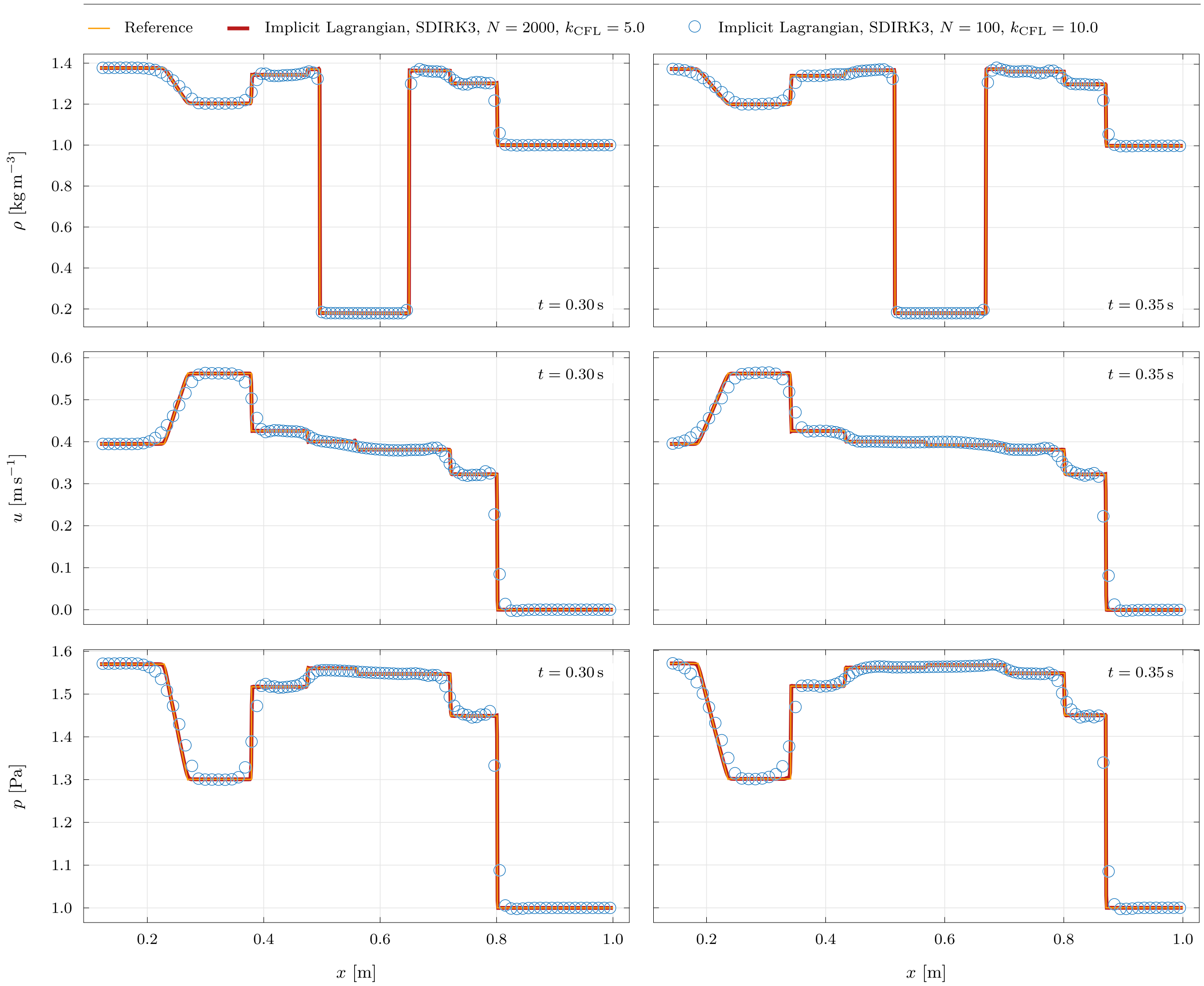

Fig. 13. One-dimensional shock–bubble interaction problem of Quirk and Karni [93] at time $t = 0.30$ s and $t = 0.35$ s. The solution obtained with the proposed implicit Lagrangian scheme and third order diagonally implicit Runge–Kutta time-‘stepping, using the second-order energy diffusion operator, on $N = 2000$ uniformly spaced mesh points (i.e. with non-uniform mass Δm) at $k_{\mathrm{CFL}} = 5.0$, visually overlaps the reference given by an explicit Eulerian MUSCL–Hancock method with 50,000 uniform cells. No significant artefacts are visible in the under-resolved solution using $N = 100$ points at $k_{\mathrm{CFL}} = 10$, while adequately capturing all flow features.

In Fig. 13 we show the solutions given by the proposed scheme with third order SDIRK time-‘stepping, at times $t = 0.30$ s and $t = 0.35$ s. The test is run on two meshes, composed of $N = 2000$ or $N = 100$ cells with constant $\Delta x = (x_{\mathrm{R}} - x_{\mathrm{L}})/N$ (and consequently discontinuous Δm), using $k_{\mathrm{CFL}} = 5.0$ and $k_{\mathrm{CFL}} = 10.0$ respectively. The results match the reference solution given by an explicit, Eulerian, second order, path-conservative [94,95] Finite Volume MUSCL–Hancock method applied to the Kapila system, on a uniform mesh composed of 50,000 control volumes.

5.5. Application to stratified systems

The battery of tests is concluded by solving a series of applicative problems on multilayer systems, like in the paper by Phan et al. [10], from which we derive the setup consisting of a set of alternating layers of different density and material parameters, upon which an initially smooth pressure perturbation is allowed to propagate.

The alternating layers of different materials (characterized by different initial density and parameters of the equation of state), have constant length $L_{\mathrm{l}} = (x_{\mathrm{R}} - x_{\mathrm{L}})/N_{\mathrm{l}}$. The leftmost layer will be assigned initial density ρ_1 and parameters of the equation of state γ_1 and Π_1, with the following layer switching to density ρ_2 and parameters γ_2 and Π_2, then back to ρ_1, γ_1 and Π_1, and so on.

Formally, we can set $c(x) = \mathrm{mod}_2\big(1 + \lfloor x/L_{\mathrm{l}} \rfloor\big)$, with mod_2 denoting the remainder operator for integer division by 2, and then define the initial data as

$$\rho(t = 0, x) = c\,\rho_1 + (1 - c)\,\rho_2, \quad \gamma(x) = c\,\gamma_1 + (1 - c)\,\gamma_2, \quad \Pi(x) = c\,\Pi_1 + (1 - c)\,\Pi_2. \tag{76}$$

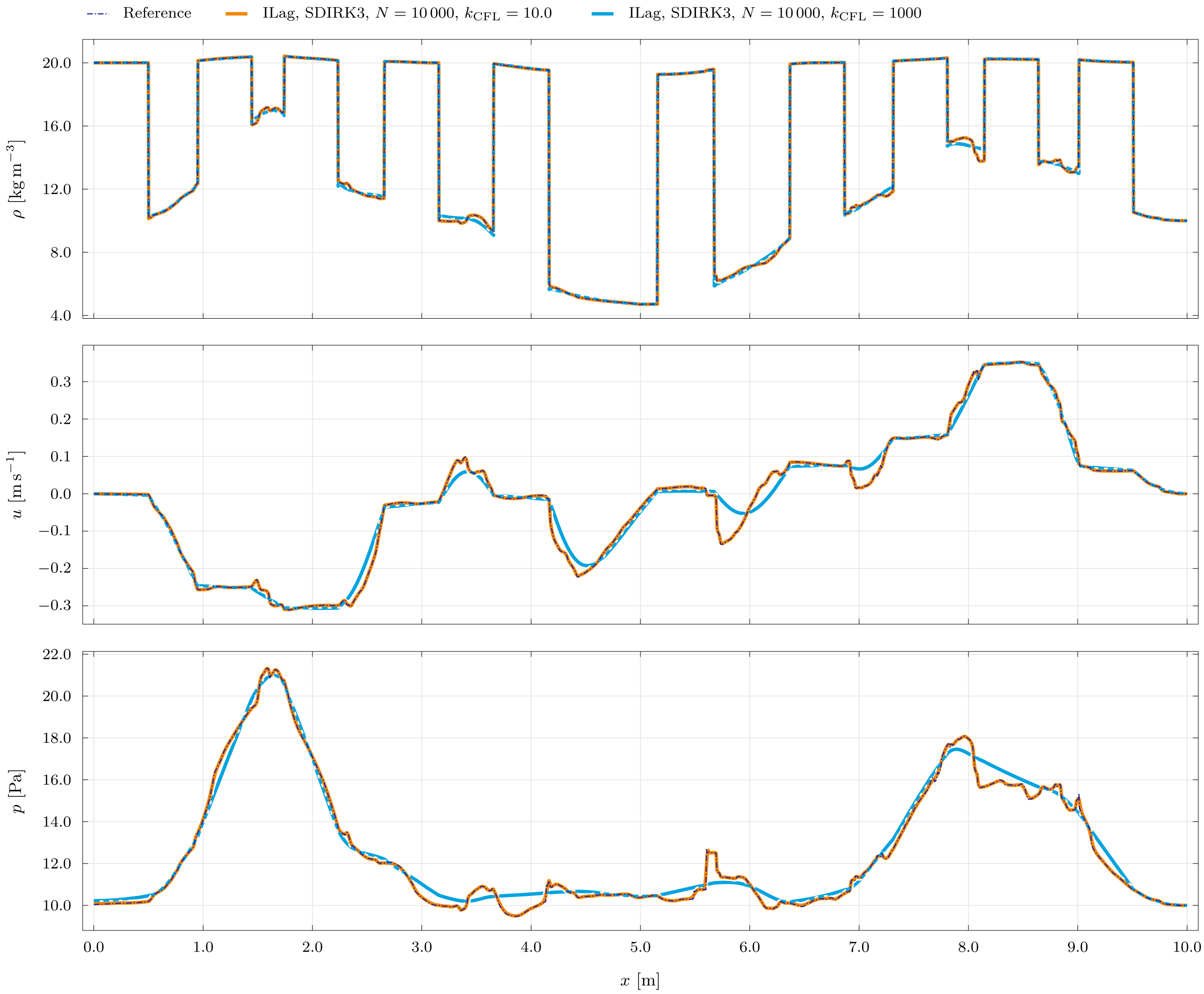

Fig. 14. Numerical results for the stratified medium problem SM1. For each flow variable, we show the solutions given by the proposed implicit Lagrangian method on a grid of $N = 10,000$ cells (500 cells per layer) at $k_{\mathrm{CFL}} = 10.0$ and $k_{\mathrm{CFL}} = 1000$. The first solution visually coincides with the reference, and with higher CFL the main structures are captured, while high frequency details are filtered out by the coarse time-stepping. The reference solution has been obtained by solving the Kapila two-phase flow model model with an explicit Eulerian method, on a fine grid of half a million cells.

Note that $c(x)$ can evaluate only to $c = 0$ or to $c = 1$, and thus no mixed states are produced in (76). The fluid is initially at rest, that is, $u(t = 0,\ x) = u_0 = 0.0\,\mathrm{m\,s^{-1}}$, and the pressure field is given by

$$p(t = 0,\ x) = \begin{cases} \left\{1 + 10\cos\left[2\,\pi\left(x - x_0\right)/\ell\right]\right\} p_0 & \text{if } \left|x - x_0\right| < \ell/2, \\ p_0 & \text{if } \left|x - x_0\right| \geq \ell/2, \end{cases} \tag{77}$$

with $\ell = 2.5\,\mathrm{m}$. In this work we present several variants of this problem, differing from each other by the choice of initial densities ρ_1 and ρ_2, material parameters γ_1, γ_2, Π_1, Π_2 and number of layers N_1. Table 5 reports the specific parameters defining each one of the variants, labelled SM1, SM2, SM3, and SM4 .

Table 5
Initial conditions and material parameters for the stratified medium problems. The number of layer pairs N_1 and the final solution times t_{end} are also reported.

	ρ_1	ρ_2	γ_1	γ_2	Π_1	Π_2	N_1	t_{end}
SM1	20.0	10.0	4.4	1.4	100.0	0.0	20	2.0
SM2	10^4	10.0	4.4	1.4	100.0	0.0	20	2.5
SM3	10^4	10.0	4.4	1.4	10^8	0.0	20	1.0
SM4	20.0	10.0	4.4	1.4	10^4	0.0	200	2.0

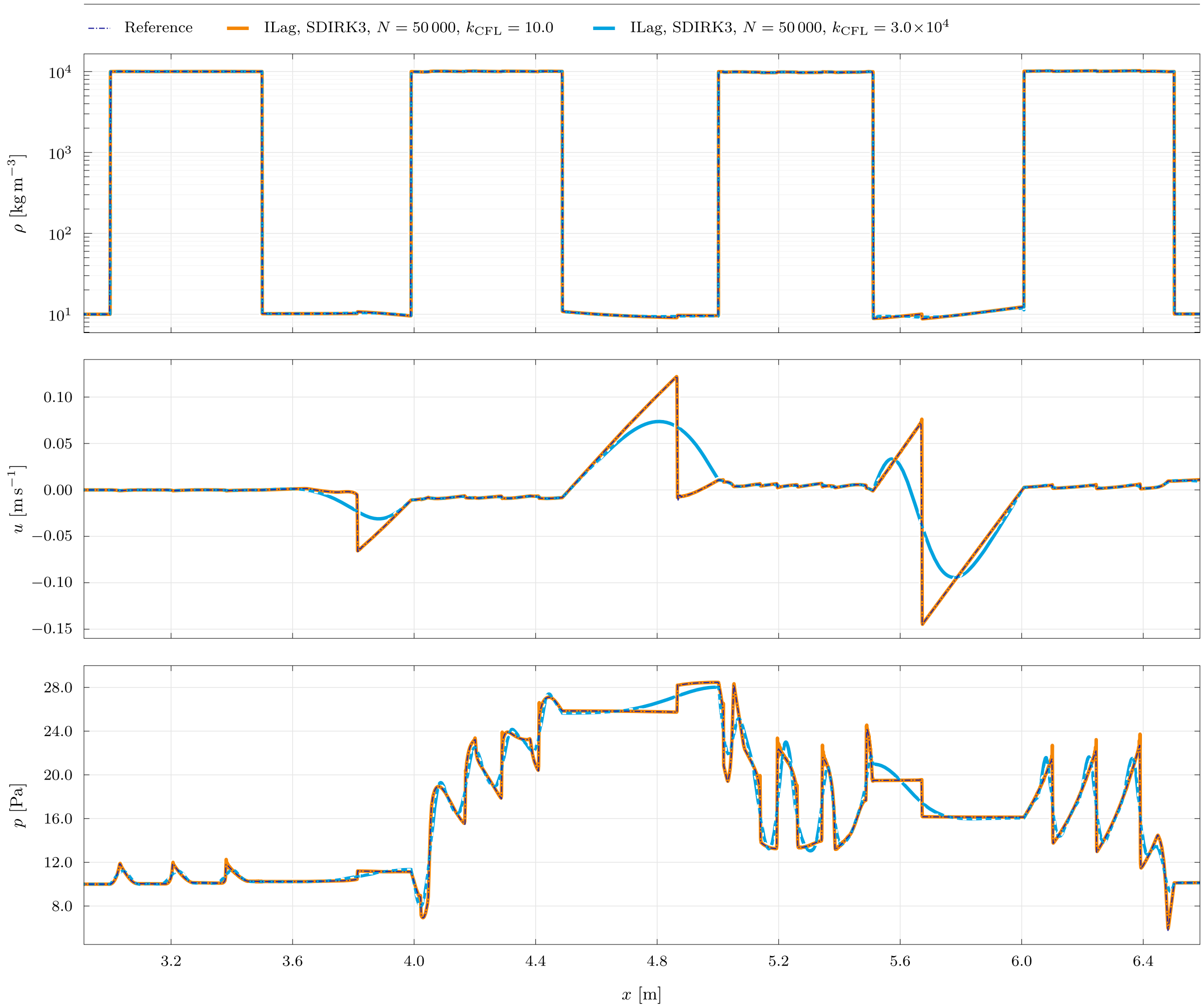

Fig. 15. Numerical results for the stratified medium problem SM2 (the density ratio is $\rho_1/\rho_2 = 1000$). For each flow variable, we show the solutions given by the proposed implicit Lagrangian method on a grid of $N = 50,000$ cells (2500 cells per layer) at $k_{\mathrm{CFL}} = 10.0$ and $k_{\mathrm{CFL}} = 30,000$. The first solution visually coincides with the reference, and with higher CFL the main flow structures are captured without introducing instabilities. The reference solution has been obtained by solving the Kapila two-phase flow model model with an explicit Eulerian method, on a fine grid of half a million cells.

While the numerical discretisation itself would allow for any distribution of layers (as in Section 5.4 for example), this setup with a constant layer width has been chosen as a matter of convenience when comparing the results with those of a homogenised model.

The test labelled SM1 is a configuration like the one originally shown by Phan et al., with mild density and compressibility ratios, which nevertheless yield a sizeable mismatch of the wavespeeds in the two media, due to the Lagrangian framework.

Test SM2 introduces a new element of difficulty by increasing the density ratio from 2 to 1000. The lower density has been kept as $\rho_2 = 10.0$ while we increased ρ_1 to $\rho_1 = 10^4$, so to explore different regimes while changing only one parameter of the problem with respect to the original data given in Phan et al. [10], keeping in mind that the scaling of the parameters has to be considered with respect to each other.

A third variant, SM3 modifies one more parameter with respect to SM2, to obtain a density ratio of 1000 and at the same time increase the material pressure parameter Π_1 from $\Pi_1 = 100.0$ to $\Pi_1 = 10^8$, giving raise to a challenging situation in which the mismatch between the wavespeeds in the two media warrants the use of CFL numbers as high as $k_{\mathrm{CFL}} = 10^9$. Due to the density ratio and low compressibility of the heavy phase, this test can be seen as a proxy for air-water configurations.

A final fourth alternative configuration, SM4 is a slightly stiffened version of SM1, where the pressure parameter Π_1 is increased to $\Pi_1 = 10^4$ and the number of layers is also increased to $N_1 = 200$. This variant is intended to show how the stratified media presented in this section behave if the number of layers is very high.

The results in Fig. 14, relative to the base configuration SM1, show that The solution given by the method using $N = 10^4$ cells (500 per layer) and $k_{\mathrm{CFL}} = 10$ matches the converged reference solution given by a semi-implicit Finite Volume solver for Kapila's

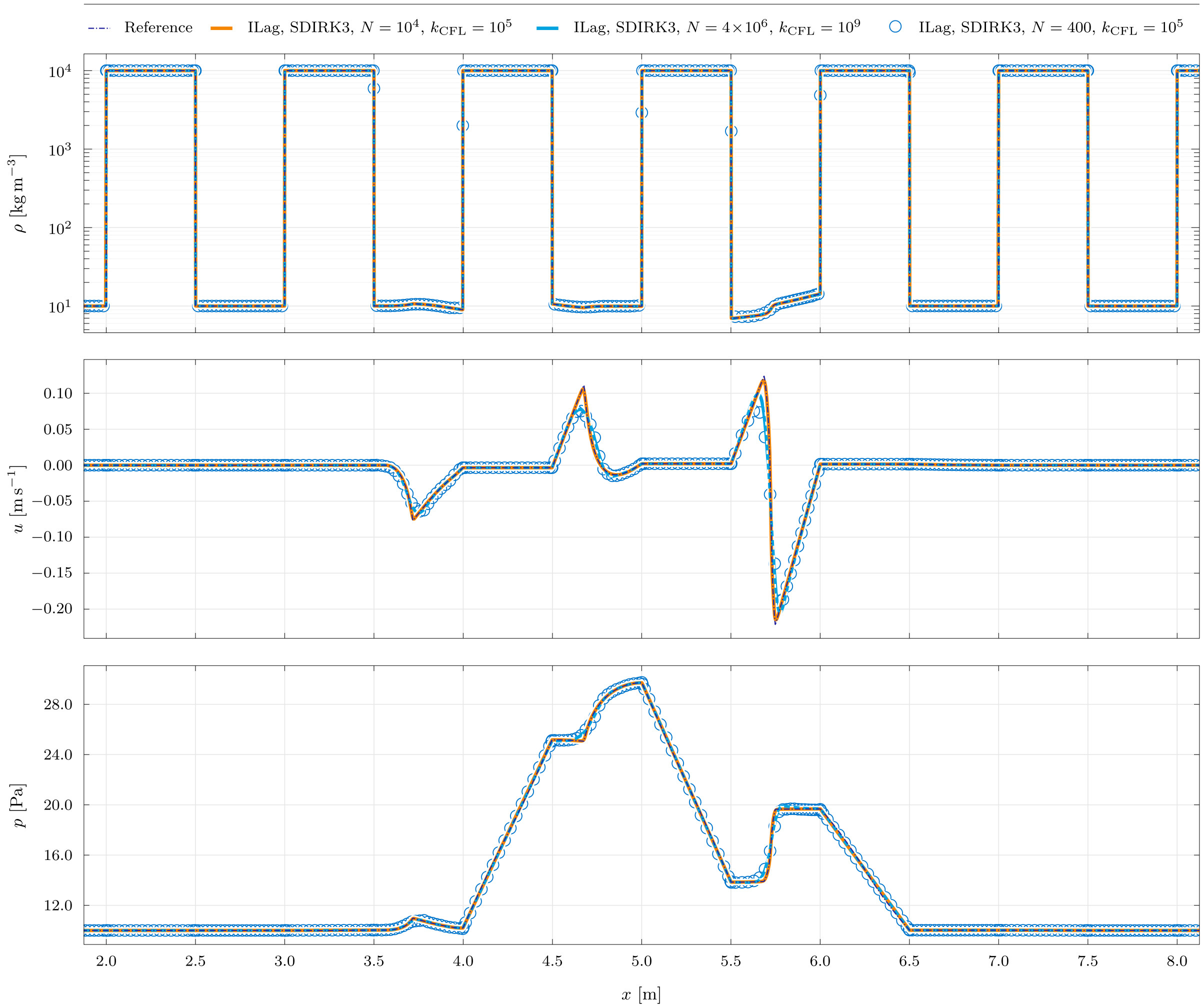

Fig. 16. Numerical results for the stratified medium problem SM3 (the density ratio is $\rho_1/\rho_2 = 1000$ and $\Pi_1 = 10^8$). For each flow variable, we show the solution given by the proposed implicit Lagrangian method on different grids and at different CFL values. A well-resolved run employing $N = 10,000$ cells and $k_{\mathrm{CFL}} = 100,000$ is visually identical to the reference solution. A second run with four million cells and $k_{\mathrm{CFL}} = 10^9$ shows that if very fine meshes are to be used, then correspondingly high CFL values can be adopted. A third run with $N = 400$ cells and $k_{\mathrm{CFL}} = 10^5$ shows that the main flow features can be captured using modest grid sizes.

reduced Baer–Nunziato model, and that increasing the timestep size by setting $k_{\mathrm{CFL}} = 1000$ preserves the structure of the solution, while filtering out the higher frequencies, as ordinarily expected.

In Fig. 15, the same behaviour is observed for the problem with a higher density ratio SM2, the solution using $N = 50,000$ cells (2500 per layer) matches the converged reference from an independent solver/model and the increasing the timestep by setting $k_{\mathrm{CFL}} = 3 \times 10^4$ maintains the structure of the solution, smoothing out the sharper features.

In Fig. 16, it is shown that the scheme can perform well, particularly in extremely stiff regimes, also if the number of cells is decreased. The solution using $N = 10^4$ cells (500 per layer) matches the converged reference from the semi-implicit multiphase solver, and the same holds for a finer mesh of $N = 10^6$ cells, using $k_{\mathrm{CFL}} = 10^9$. Additionally, a coarser simulation using $N = 400$ total cells (20 per layer) and $k_{\mathrm{CFL}} = 10^5$, can also capture the reference solution with relatively small deterioration in the accuracy of the results. This test represents a particularly challenging scenario for explicit solvers, due to heavy low-Mach effects and stringent timestep restrictions. The low-Mach or quasi-incompressible behaviour of the system can be clearly observed in Fig. 16, which features linearly varying pressure in the heavy stiff medium, while slightly more complex profiles are observed in the lighter gas phase. The reference solution has been computed by means of a semi-implicit Eulerian, second order, path-conservative [94,95] Finite Volume applied to Kaplia's multiphase flow model, specifically the one presented in Chiocchetti and Dumbser [96].

In Fig. 17, the results of the physical system SM4 and of the proposed numerical method show that systems with many layers, when dynamics are fully resolved, exhibit an emergent oscillatory behaviour, which visually averages out to the physics captured by mixture models like the reduced Baer–Nunziato model by Kapila (red line), in which the fluid is modeled as a homogeneous one with an internal energy which is a volume-weighted average of the internal energy of the two adjacent layers, assuming pressure

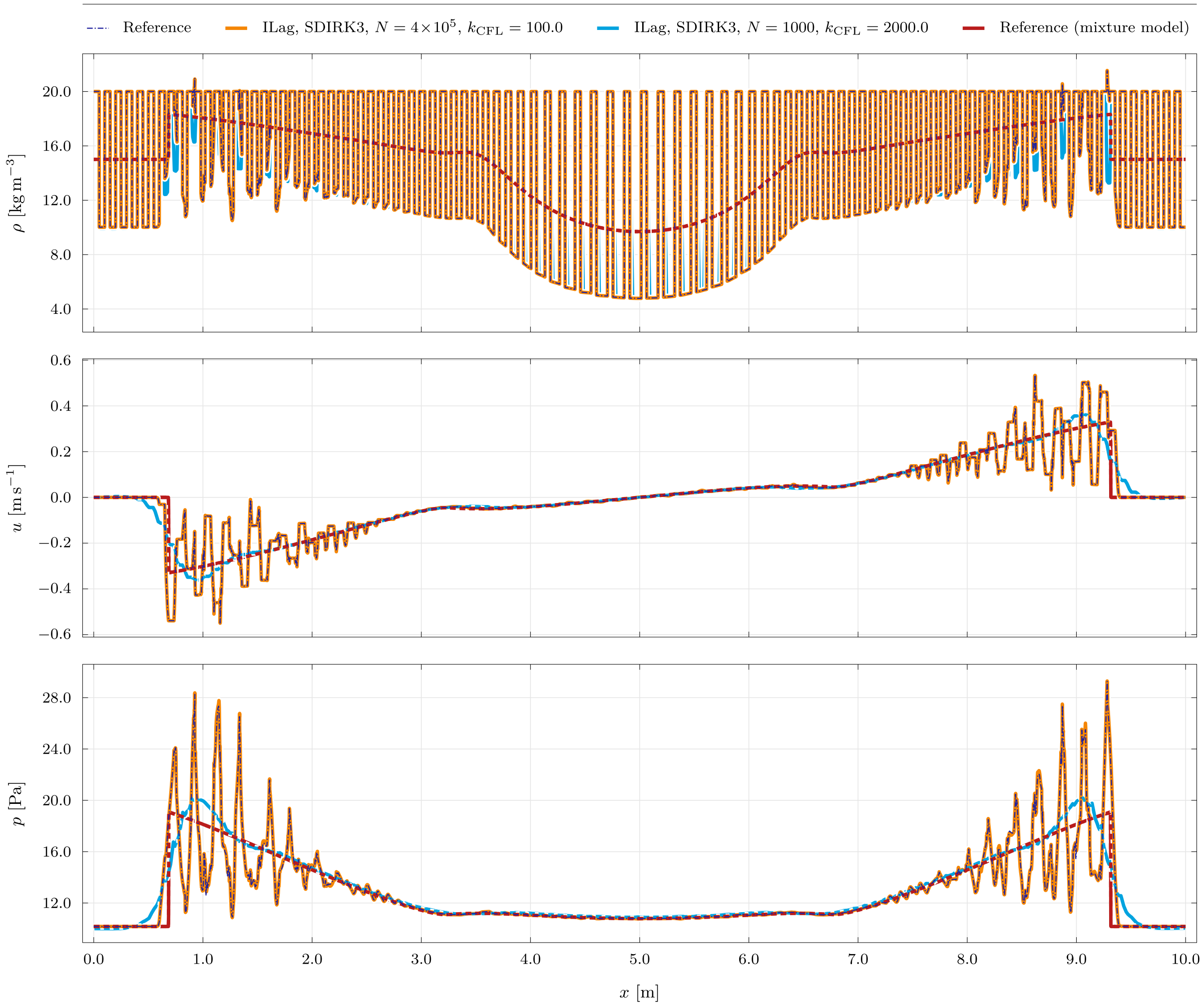

Fig. 17. Numerical results for the stratified medium problem SM4 (the layer count is $N_l = 200$). For each flow variable, we show the solution given by the proposed implicit Lagrangian method on different grids and at different CFL values. A well-resolved run employing $N = 400,000$ cells (2000 per layer) and $k_{\text{CFL}} = 100.0$ matches the reference solution. A second run using $N = 1000$ cells (5 per layer) and $k_{\text{CFL}} = 2000$ (that is, under-resolved in both space and time) yield a solution that tends towards that given by the multiphase model for the fluid mixture.

equilibrium of the two phases. The same volume weighting defines the density of the mixture. The propagation speed of the shock front is the same in both configurations, while the detailed solution of the stratified system also shows strong physical oscillations. The physical nature of the oscillations and their accuracy has been verified by comparing the solution given by the proposed scheme using $N = 4\times10^5$ cells (2000 per layer) and $k_{\text{CFL}} = 100$ with a reference obtained with a semi-implicit solver for the Kapila model (also resolving each layer separately) and $N = 2\times10^6$ cells, showing that the solutions match, while using different model equations and different numerical methods. The reference scheme was also employed to obtain the reference solution for the system by treating the domain as if filled with a uniform mixture of the two fluids. As mentioned, this mixture solution can be observed to match the space-averaged behaviour of the stratified medium, and appears to be also captured by the proposed implicit Lagrangian method if the flow is under-resolved in space and time, here taking $N = 1000$ cells (5 per layer) and $k_{\text{CFL}} = 2000$.

6. Conclusions

In this paper we introduced an original fully implicit finite volume scheme for the numerical solution of layered multifluid in Lagrangian mass coordinates.

The method is based on a simple non-conservative (possibly oscillatory) predictor, and a quasi-conservative, non-oscillatory corrector, which is stable for arbitrarily large CFL numbers. It is second order accurate in space, while it can be made arbitrarily high order accurate in time using SDIRK time integrators. We implement and test second and third order accurate schemes in time.

Given that the method is stable for large CFL numbers, the time step can be set based on just accuracy requirements. This means that when solutions are expected to be sufficiently accurate, the use of a third order method in time may be more efficient than a second order one, as it is shown in the error-CPU plot (see Fig. 11).

Indeed, when using implicit time discretization, the time step restriction is no longer based on acoustic speeds. This means that some time step control would be useful to assess the optimal time step, which is therefore based on accuracy requirements, rather than stability ones. Although several time-step controllers have been widely adopted for both explicit and implicit numerical solvers of systems of ordinary differential equations (see the books by Hairer and Wanner for example [97,98], as well as a recent application to RANS simulations with large timesteps [99]), it would be interesting to explore time step controllers suitable for the present implicit step, which makes use of the peculiar features of the novel scheme. This subject is currently under investigation.

The method is very flexible and robust, and is validated on a large battery of tests, which includes all the problems in Toro's book on the Euler equations [91], the tests on multifluids by Abgrall and Karni [69], the tests on a finely stratified multilayer systems [10], and other much harder variations on these, in which the two fluids have a large ratio in the standard density and in the stiffness, such as, for example, a sequence of several air-water pairs.

With the proposed method it is possible to observe interesting physical phenomena. For example, in a sequence of water-air pairs, with layers of approximately the same thickness, the internal energy variation with respect to a rest configuration is larger in the air regions, as expected. Kinetic energy appears larger in the water layers, for smooth flow, while in presence of shocks the kinetic energy may appear to be larger in the air layers.

The efficiency and robustness of the method suggests several applications, which constitute current work in progress:

Shock impact resilience. A screen made of composite material formed by several layers of two different materials may offer better protection from the impact of a projectile than a screen of a single material with the same thickness. The optimal distribution of layers that guarantees the best protection is still an open problem. The method developed in this paper may help designing optimal shields made out of suitable layers of two (or more) materials (see Verreault and van der Voort [100]). Note that to find the optimal (or a good) layering strategy is an optimization problem that may require several accurate solutions of the direct problem, and for this reason it is extremely important to rely on a fast and accurate method.

Singularity formation in stratified material in slab geometry. In a remarkable paper by Zababakhin [101] it is stated that it is possible to produce a singularity in the solution of compressible Euler equations, similar to the ones obtained with implosive shocks in a single gas in cylindrical or spherical symmetry, just in slab geometry, provided a shock propagates into suitable sequence of layers of two different fluids. The method developed in the current paper could be used to actually compute such kind of solution, and perhaps to formulate conjectures about possible layer distributions that lead to singularity formation in the multifluid system.

Metamaterials composed by layers of several different constituents. In this paper we show that the numerical solutions obtained by our method for a stratified multifluid are in excellent agreement with a detailed numerical solution of the Kapila model in which the two phases are never really mixed (except numerically near an interface between the two fluids), so that in most of the computational domain the mass fractions of each fluid is either zero or one. Kapila model is more general than the multifluid solver developed in this paper for the treatment of fluid mixture, since it deals with intermediate states, however it is much less efficient for the specific case of immiscible multilayer. Furthermore, our method, like any Lagrangian method, can seamlessly deal with a multilayer system composed by an arbitrary number of different materials, while in its current form Kapila's model can handle only a mixture of two fluids. This opens enormous possibilities in exploring nonlinear wave propagation in metamaterials composed of several different media, and in the numerical simulation of new layered multimaterials.

In conclusion, the new scheme opens new perspectives in the study of layered multimaterial, with promising applications in science and technology.

CRediT authorship contribution statement

Simone Chiocchetti: Writing - review & editing, Writing - original draft, Visualization, Validation, Software, Resources, Methodology, Investigation, Funding acquisition, Formal analysis, Data curation, Conceptualization; **Giovanni Russo:** Writing - review & editing, Writing - original draft, Visualization, Validation, Software, Resources, Methodology, Investigation, Funding acquisition, Formal analysis, Conceptualization.

Data availability

Data will be made available on request.

Declaration of competing interest

The authors declare that they have no known competing financial interests or personal relationships that could have appeared to influence the work reported in this paper.

Acknowledgments

G. Russo and S. Chiocchetti would like to thank the Italian Ministry of University and Research (MUR) to support this research with funds coming from PRIN Project 2022 (No. 2022KA3JBA entitled "Advanced numerical methods for time dependent parametric partial differential equations with applications"), and from the European Union's NextGenerationUE—Project: Centro Nazionale HPC, Big Data e Quantum Computing, "Spoke 1" (CUP E63C22001000006).

S. Chiocchetti acknowledges the support obtained by the Deutsche Forschungsgemeinschaft (DFG) via the project DROPIT, grant no. GRK 2160/2, and from the European Union's Horizon Europe Research and Innovation Programme under the Marie Skłodowska-Curie Postdoctoral Fellowship MoMeNTUM (grant agreement no. 101109532).

S. Chiocchetti would also like to thank M. Dumbser for his encouragement and to acknowledge the fundamental insights he provided during the early development of the scheme presented in this work.

Appendix A. Additional diffusion

In this appendix, we report the details concerning an additional diffusion step applied selectively to address strong oscillations encountered in a two of the shock tube problems of Toro. Whenever such more aggressive diffusion is needed, for example in tests involving extremely strong shock waves (see Section 5.1, problems *Toro1* and *Toro6* for the only two test cases in which this addition to the diffusion operator has been applied), then the target value $V_i^{n+1,*}$ for specific volume is further modified with a second filtering procedure. To do so, we operate a second pass over the list of corrected specific volume values $V_i^{n+1,*}$, using a four cell window spanning from cell $i-1$ to cell $i+2$, and computing further corrected values for i and $i+1$, the two central cells of the window:

$$\begin{aligned} V_i^{n+1,**} &= (1-w_i)\,V_i^{n+1,*} + w_i\left[V_{i-1}^{n+1,*} + \frac{m_i - m_{i-1}}{m_{i+2}-m_{i-1}}\left(V_{i+2}^{n+1,*} - V_{i-1}^{n+1,*}\right)\right],\\ V_{i+1}^{n+1,**} &= (1-w_i)\,V_{i+1}^{n+1,*} + w_i\left[V_{i-1}^{n+1,*} + \frac{m_{i+1} - m_{i-1}}{m_{i+2}-m_{i-1}}\left(V_{i+2}^{n+1,*} - V_{i-1}^{n+1,*}\right)\right]. \end{aligned} \tag{A.1}$$

Eq. (A.1) states that these second-pass corrected values $V_i^{n+1,**}$ and $V_{i+1}^{n+1,**}$ are weighted averages of 1. the previous corrected values $V_i^{n+1,*}$ and $V_{i+1}^{n+1,*}$ and 2. a simple linear interpolation between the two cell centers of the outer cells of the four cell window. The weight is computed as a function of the linear regression slopes a_i (associated with cells $i-1$, i, and $i+1$) and a_{i+1} (associated with cells i, $i+1$, $i+2$). Specifically we set

$$w_i = \min\left(1,\ r_{i,i}\,r_{i,i+1} + \frac{2\left|a_i - a_{i+1}\right|}{\left|a_i\right| + \left|a_{i+1}\right| + \epsilon}\right), \qquad \epsilon = 10^{-14} \tag{A.2}$$

with the linear regression coefficients being

$$a_i = \frac{\sum_{k=-1}^{1}\left(m_{i+k} - m_{i,\mathrm{m}}\right)\left(V_{i+k}^{n+1,*} - V_{i,\mathrm{m}}^{n+1,*}\right)}{\sum_{k=-1}^{1}\left(m_{i+k} - m_{i,\mathrm{m}}\right)^2}, \qquad b_i = V_{i,\mathrm{m}}^{n+1,*} - a_i\, m_{i,\mathrm{m}}, \tag{A.3}$$

while having denoted

$$m_{i,\mathrm{m}} = \frac{1}{3}\sum_{k=-1}^{1} m_{i+k}, \qquad V_{i,\mathrm{m}}^{n+1,*} = \frac{1}{3}\sum_{k=-1}^{1} V_{i+k}^{n+1,*}, \tag{A.4}$$

and having defined the normalised residuals of each one of the linear regression lines over three cells as

$$r_{i,i} = \frac{\sum\limits_{k=-1}^{1}\left|b_i + a_i\left(m_{i+k} - m_{i-1}\right) - V_{i+k}^{n+1,*}\right|}{\left|V_{i+1}^{n+1,*} - V_{i-1}^{n+1,*}\right| + \epsilon}, \qquad r_{i,i+1} = \frac{\sum\limits_{k=0}^{1}\left|b_{i+1} + a_{i+1}\left(m_{i+k} - m_i\right) - V_{i+k}^{n+1,*}\right|}{\left|V_{i+2}^{n+1,*} - V_i^{n+1,*}\right| + \epsilon}. \tag{A.5}$$

Each four-cell stencil spanning from cell $i-1$ to cell $i+2$ will generate a filtered value for both the central cells i and $i+1$. Since each cell is considered twice in this four-cell-stencil filtering procedure, once as the center-left cell and once as the center-right cell in the stencil, the specific volume $V_i^{n+1,**}$ that will be used to replace $V_i^{n+1,*}$ is taken to be the arithmetic average of the two. We finally remark that this second step of artificial diffusion is in general not used for the results presented in this paper, unless as clearly indicated in two of the shock tube problems of Toro [91] in Section 5.1.

Appendix B. Automatic computation of the mesh parameter

In this appendix we provide the details concerning the automatic procedure used for the selection of the parameters adopted to construct the meshes used in this work. These parameters can in principle be set manually, but removing such a need is beneficial A manual selection of the mesh parameters β and especially z_0 might be a bother for the user, and the range of selectable values (constrained by positivity requirements on Δm_i) is not immediately apparent. For this reason we adopted a simple procedure that eliminates this issue and always yields valid well-graded meshes.

The procedure starts by defining $\rho^*_{\mathrm{L}} = \min(\rho_{\mathrm{L}},\ \rho_{\mathrm{R}})$ and $\rho^*_{\mathrm{R}} = \max(\rho_{\mathrm{L}},\ \rho_{\mathrm{R}})$ so that the left layer is less dense than the right on and aims at computing a value for the nondimensional parameter β and a corresponding optimal value for the shift z_0, such that, together with the mass conservation constraints (67), the induced spacings Δm_{L} and Δm_{R} are both positive and their ratio $\Delta m_{\mathrm{L}}/\Delta m_{\mathrm{R}}$ is as similar as possible as the density ratio $\rho^*_{\mathrm{L}}/\rho^*_{\mathrm{R}}$.

Formally this corresponds to finding β and z_0 that minimize a cost function of the type

$$q = \left| \frac{\Delta m_{\mathrm{L}}\left(\beta,\ z_0\right) \rho^*_{\mathrm{R}}}{\Delta m_{\mathrm{R}}\left(\beta,\ z_0\right) \rho^*_{\mathrm{L}}} - 1 \right| + \max\left\{0,\ H \,\mathrm{sign}\left[\Delta m_{\mathrm{L}}\left(\beta,\ z_0\right) \Delta m_{\mathrm{R}}\left(\beta,\ z_0\right)\right]\right\}, \tag{B.1}$$

with $H = 10^{20}$ a penalty coefficient that excludes invalid meshes containing negative values for the spacing. In practice, we find a value for β in the interval between $\beta = 0$ (which corresponds to a uniform spacing mesh) and a larger initial value $\beta_0 = 1/4$ (corresponding to a rather gradual transition between the two meshes), starting from $\beta = \beta_0$ and bisecting the interval towards the largest admissible β. At each iteration of the bisection procedure, for a fixed iteration value of β, the value of z_0 that minimizes (B.1) is found through a nested grid search.

At the end of the procedure, if ρ^*_{L} and ρ^*_{R} do not correspond to ρ_{L} and ρ_{R} respectively, that is, if they had to be switched, the sign of z_0 is switched, restoring the original orientation of the two layers. This allow to define a stopping criterion for the bisection process, saying that it can terminate as soon as q falls below a certain threshold $q_{\mathrm{f}} = 0.25$, which states that the ratio between the mesh spacing $\Delta m_{\mathrm{L}}/\Delta m_{\mathrm{R}}$ and the density ratio $\rho^*_{\mathrm{L}}/\rho^*_{\mathrm{R}}$ are allowed to differed by $q_{\mathrm{f}} = 0.25$ if the initial choice of β was so large that the bisection procedure had to be entered. For low to moderate density ratios, usually β_0 is accepted immediately without requiring to be reduced by the bisection process.

Once the parameters z_0 and β are fixed, the formula for computing the final mesh spacing can be applied regardless of the orientation of the density jump, generating for any given number of cells n in the half-layer pair, a well-graded variable spacing mesh that satisfies the mass constraints of the initial condition. In Fig. 2 we give an illustration of the procedure, showing a comparison with the uniform Eulerian grid in the reference space z and in the Eulerian coordinate system x (in which the mesh appears completely different), together with an example of how several half-layer pairs can be mirrored and concatenated to form the grid of a many-layer system. In a final note it must be specified that when concatenating many half-layer pairs, a single half-layers must be added at each one of the domain extremities: to do so, we simply replicate the mesh spacing of the last cell generated by the above procedure and then rescale each Δm_i, in the single half-layers at the extremities and in their directly neighbouring half-layers, by a constant factor to match the mass conservation constraints. The effect of this rescaling is clear in the rightmost panel of Fig. 2.

References

[1] S.A. Cummer, J. Christensen, A. Alù, Controlling sound with acoustic metamaterials, Nat. Rev. Mater. 1 (3) (2016) 1–13.
[2] D. Torrent, J. Sánchez-Dehesa, Acoustic metamaterials for new two-dimensional sonic devices, New J. Phys. 9 (9) (2007) 323.
[3] G. Ma, P. Sheng, Acoustic metamaterials: from local resonances to broad horizons, Sci. Adv. 2 (2) (2016) e1501595.
[4] S.H. Lee, O.B. Wright, Origin of negative density and modulus in acoustic metamaterials, Phys. Rev. B 93 (2) (2016) 024302.
[5] I. Peshkov, E. Romenski, M. Dumbser, Continuum mechanics with torsion, Contin. Mech. Thermodyn. 31 (5) (2019) 1517–1541. https://doi.org/10.1007/s00161-019-00770-6
[6] R.J. LeVeque, D.H. Yong, Solitary waves in layered nonlinear media, SIAM J. Appl. Math. 63 (2003) 1539–1560.
[7] M. Quezada de Luna, D.I. Ketcheson, Two-dimensional wave propagation in layered periodic media, SIAM J. Appl. Math. 74 (6) (2014) 1852–1869.
[8] D.I. Ketcheson, L. Lóczi, G. Russo, A multiscale model for weakly nonlinear shallow water waves over periodic bathymetry, 2023. ArXiv preprint arXiv:2311.02603
[9] M. Quezada de Luna, D.I. Ketcheson, Solitary water waves created by variations in bathymetry, J. Fluid Mech. 917 (2021) A45.
[10] D.T.M. Phan, S.L. Gavrilyuk, G. Russo, Numerical validation of homogeneous multi-fluid models, Appl. Math. Comput. 441 (2023) 127693.
[11] A. Chiapolino, R. Saurel, Extended Noble–Abel stiffened-gas equation of state for sub-and-supercritical liquid-gas systems far from the critical point, Fluids 3 (3) (2018). https://doi.org/10.3390/fluids3030048
[12] D. Bresch, C. Burtea, F. Lagoutière, Mathematical justification of a compressible bifluid system with different pressure laws: a continuous approach, Appl. Anal. 101 (12) (2022) 4235–4266. https://doi.org/10.1080/00036811.2022.2103679
[13] D. Bresch, C. Burtea, F. Lagoutière, Mathematical justification of a compressible bi-fluid system with different pressure laws: a semi-discrete approach and numerical illustrations, J. Comput. Phys. 490 (2023) 112259. https://doi.org/10.1016/j.jcp.2023.112259
[14] M.R. Baer, J.W. Nunziato, A two-phase mixture theory for the deflagration-to-detonation transition (ddt) in reactive granular materials, Int. J. Multiph. Flow 12 (6) (1986) 861–889. https://doi.org/10.1016/0301-9322(86)90033-9
[15] Richard Saurel, F. Petitpas, R.A. Berry, et al., Simple and efficient relaxation methods for interfaces separating compressible fluids, cavitating flows and shocks in multiphase mixtures, J. Comput. Phys. 228 (5) (2009) 1678–1712. https://doi.org/10.1016/j.jcp.2008.11.002
[16] M. Pelanti, K.-M. Shyue, et al., A mixture-energy-consistent six-equation two-phase numerical model for fluids with interfaces, cavitation and evaporation waves, J. Comput. Phys. 259 (2014) 331–357. https://doi.org/10.1016/j.jcp.2013.12.003
[17] A.K. Kapila, R. Menikoff, J.B. Bdzil, S.F. Son, D.S. Stewart, Two-phase modeling of deflagration-to-detonation transition in granular materials: reduced equations, Phys. Fluids 13 (10) (2001) 3002–3024.
[18] M. Petrella, R. Abgrall, S. Mishra, (2023). A Monte–Carlo ab-initio algorithm for the multiscale simulation of compressible multiphase flows, arXiv preprint arXiv:2303.16540
[19] R. Saurel, R. Abgrall, A multiphase godunov method for compressible multifluid and multiphase flows, J. Comput. Phys. 150 (2) (1999) 425–467. https://doi.org/10.1006/jcph.1999.6187
[20] E. Romenski, A.D. Resnyansky, E.F. Toro, Conservative hyperbolic formulation for compressible two-phase flow with different phase pressures and temperatures, Q. Appl. Math. 65 (2007) 259–279.
[21] E. Romenski, D. Drikakis, E.F. Toro, Conservative models and numerical methods for compressible two-phase flow, J. Sci. Comput. 42 (2010) 68–95.
[22] E. Romenski, A.A. Belozerov, I.M. Peshkov, Conservative formulation for compressible multiphase flows, Q. Appl. Math. 74 (1) (2016) 113–136. https://www.jstor.org/stable/26835281.
[23] F. Thein, E. Romenski, M. Dumbser, et al., Exact and numerical solutions of the Riemann problem for a conservative model of compressible two-phase flows, J. Sci. Comput. 93 (3) (2022) 83. https://doi.org/10.1007/s10915-022-02028-x
[24] L. Río-Martín, M. Dumbser, et al., High-order ADER discontinuous Galerkin schemes for a symmetric hyperbolic model of compressible barotropic two-fluid flows, Commun. Appl. Math. Comput. 6 (4) (2024) 2119–2154. https://doi.org/10.1007/s42967-023-00313-6

[25] M. Sussman, P. Smereka, S. Osher, A level set approach for computing solutions to incompressible two-phase flow, J. Comput. Phys. 114 (1) (1994) 146–159. https://doi.org/10.1006/jcph.1994.1155

[26] N. Favrie, S.L. Gavrilyuk, R. Saurel, et al., Solid-fluid diffuse interface model in cases of extreme deformations, J. Comput. Phys. 228 (16) (2009) 6037–6077. https://doi.org/10.1016/j.jcp.2009.05.015

[27] F. Kemm, E. Gaburro, F. Thein, M. Dumbser, A simple diffuse interface approach for compressible flows around moving solids of arbitrary shape based on a reduced Baer–Nunziato model, Comput. Fluids 204 (2020) 104536. https://doi.org/10.1016/j.compfluid.2020.104536

[28] M. Dumbser, A simple two-phase method for the simulation of complex free surface flows, Comput. Methods Appl. Mech. Eng. 200 (9) (2011) 1204–1219. https://doi.org/10.1016/j.cma.2010.10.011

[29] E. Gaburro, M.J. Castro, M. Dumbser, A well balanced diffuse interface method for complex nonhydrostatic free surface flows, Comput. Fluids 175 (2018) 180–198. https://doi.org/10.1016/j.compfluid.2018.08.013

[30] D. Ferrari, M. Dumbser, A semi-implicit finite volume scheme for incompressible two-phase flows, Commun. Appl. Math. Comput. 6 (4) (2024) 2295–2330. https://doi.org/10.1007/s42967-024-00367-0

[31] R. Courant, K.O. Friedrichs, H. Lewy, Über die partiellen differenzgleichungen der mathematische physik, Math. Ann. 100 (1928) 32–74.

[32] A. Reinarz, D.E. Charrier, M. Bader, L. Bovard, M. Dumbser, K. Duru, F. Fambri, A.-A. Gabriel, J.-M. Gallard, S. Köppel, L. Krenz, L. Rannabauer, L. Rezzolla, P. Samfass, M. Tavelli, T. Weinzierl, ExaHyPE: an engine for parallel dynamically adaptive simulations of wave problems, Comput. Phys. Commun. 254 (2020) 107251. https://doi.org/10.1016/j.cpc.2020.107251

[33] M. Kurz, D. Kempf, M. Blind, P. Kopper, P. Offenhäuser, A. Schwarz, S. Starr, J. Keim, A. Beck, GALÆXI: Solving complex compressible flows with high-order discontinuous Galerkin methods on accelerator-based systems, Comput. Phys. Commun. (2024) 109388. https://doi.org/10.1016/j.cpc.2024.109388

[34] C.W. Hirt, A.A. Amsden, J.L. Cook, An arbitrary Lagrangian–Eulerian computing method for all flow speeds, J. Comput. Phys. 14 (3) (1974) 227–253. https://doi.org/10.1016/0021-9991(74)90051-5

[35] F. Duarte, R. Gormaz, S. Natesan, Arbitrary Lagrangian–Eulerian method for Navier–Stokes equations with moving boundaries, Comput. Methods Appl. Mech. Eng. 193 (45) (2004) 4819–4836. https://doi.org/10.1016/j.cma.2004.05.003

[36] M. Berndt, J. Breil, S. Galera, M. Kucharik, P.-H. Maire, M. Shashkov, Two-step hybrid conservative remapping for multimaterial arbitrary Lagrangian–Eulerian methods, J. Comput. Phys. 230 (17) (2011) 6664–6687. https://doi.org/10.1016/j.jcp.2011.05.003

[37] A.J. Barlow, P.-H. Maire, W.J. Rider, R.N. Rieben, M.J. Shashkov, Arbitrary Lagrangian–Eulerian methods for modeling high-speed compressible multimaterial flows, J. Comput. Phys. 322 (2016) 603–665. https://doi.org/10.1016/j.jcp.2016.07.001

[38] R. Loubère, P.-H. Maire, M. Shashkov, J. Breil, S. Galera, ReALE: a reconnection-based arbitrary-Lagrangian–Eulerian method, J. Comput. Phys. 229 (12) (2010) 4724–4761. https://doi.org/10.1016/j.jcp.2010.03.011

[39] M. Kucharik, J. Breil, S. Galera, P.H. Maire, M. Berndt, M.J. Shashkov, Hybrid remap for multi-material ALE, Comput. Fluids 46 (2011) 293–297.

[40] M. Dumbser, Arbitrary-Lagrangian–Eulerian ADER–WENO finite volume schemes with time-accurate local time stepping for hyperbolic conservation laws, Comput. Methods Appl. Mech. Eng. 280 (2014) 57–83. https://doi.org/10.1016/j.cma.2014.07.019

[41] W. Boscheri, R. Loubère, M. Dumbser, Direct arbitrary-Lagrangian–Eulerian ADER-MOOD finite volume schemes for multidimensional hyperbolic conservation laws, J. Comput. Phys. 292 (2015) 56–87. https://doi.org/10.1016/j.jcp.2015.03.015

[42] E. Gaburro, W. Boscheri, S. Chiocchetti, C. Klingenberg, V. Springel, M. Dumbser, High order direct arbitrary-Lagrangian–Eulerian schemes on moving Voronoi meshes with topology changes, J. Comput. Phys. 407 (2020) 109167. https://doi.org/10.1016/j.jcp.2019.109167

[43] W. Barsukow, P.V.F. Edelmann, C. Klingenberg, F. Miczek, F.K. Röpke, et al., A numerical scheme for the compressible low-Mach number regime of ideal fluid dynamics, J. Sci. Comput. 72 (2) (2017) 623–646. https://doi.org/10.1007/s10915-017-0372-4

[44] P. Bruel, S. Delmas, J. Jung, V. Perrier, A low Mach correction able to deal with low Mach acoustics, J. Comput. Phys. 378 (2019) 723–759. https://doi.org/10.1016/j.jcp.2018.11.020

[45] F. Rieper, A low-Mach number fix for Roe's approximate Riemann solver, J. Comput. Phys. 230 (13) (2011) 5263–5287. https://doi.org/10.1016/j.jcp.2011.03.025

[46] C.-D. Munz, S. Roller, R. Klein, K.J. Geratz, The extension of incompressible flow solvers to the weakly compressible regime, Comput. Fluids 32 (2) (2003) 173–196. https://doi.org/10.1016/S0045-7930(02)00010-5

[47] J.H. Park, C.D. Munz, Multiple pressure variables methods for fluid flow at all Mach numbers, Int. J. Numer. Methods Fluids 49 (8) (2005) 905–931. https://doi.org/10.1002/fld.1032

[48] M. Dumbser, V. Casulli, A conservative, weakly nonlinear semi-implicit finite volume scheme for the compressible Navier–Stokes equations with general equation of state, Appl. Math. Comput. 272 (2016) 479–497. Recent Advances in Numerical Methods for Hyperbolic Partial Differential Equations, https://doi.org/10.1016/j.amc.2015.08.042

[49] P. Degond, M. Tang, All speed scheme for the low Mach number limit of the isentropic Euler equations, Commun. Comput. Phys. 10 (1) (2011) 1–31.

[50] F. Cordier, P. Degond, A. Kumbaro, An asymptotic-preserving all-speed scheme for the Euler and Navier–Stokes equations, J. Comput. Phys. 231 (17) (2012) 5685–5704. https://doi.org/10.1016/j.jcp.2012.04.025

[51] S. Boscarino, G. Russo, L. Scandurra, All Mach number second order semi-implicit scheme for the Euler equations of gas dynamics, J. Sci. Comput. 77 (2018) 850–884.

[52] S. Avgerinos, F. Bernard, A. Iollo, G. Russo, Linearly implicit all Mach number shock capturing schemes for the Euler equations, J. Comput. Phys. 393 (2019) 278–312.

[53] W. Boscheri, G. Dimarco, R. Loubère, M. Tavelli, M.-H. Vignal, A second order all Mach number IMEX finite volume solver for the three dimensional Euler equations, J. Comput. Phys. 415 (2020) 109486.

[54] S. Boscarino, J.-M. Qiu, G. Russo, T. Xiong, A high order semi-implicit IMEX WENO scheme for the all-Mach isentropic Euler system, J. Comput. Phys. 392 (2019) 594–618.

[55] S. Boscarino, J. Qiu, G. Russo, T. Xiong, High order semi-implicit WENO schemes for all-Mach full Euler system of gas dynamics, SIAM J. Sci. Comput. 44 (2) (2022) B368–B394.

[56] S. Busto, L. Río-Martín, M.E. Vázquez-Cendón, M. Dumbser, A semi-implicit hybrid finite volume/finite element scheme for all Mach number flows on staggered unstructured meshes, Appl. Math. Comput. 402 (2021) 126117. https://doi.org/10.1016/j.amc.2021.126117

[57] M. Lukáčová-Medvid'ová, G. Puppo, A. Thomann, An all Mach number finite volume method for isentropic two-phase flow, J. Numer. Math. 31 (3) (2023) 175–204.

[58] M. Lukáčová-Medvid'ová, I. Peshkov, A. Thomann, An implicit-explicit solver for a two-fluid single-temperature model, J. Comput. Phys. 498 (2024) 112696. https://doi.org/10.1016/j.jcp.2023.112696

[59] U.M. Ascher, S.J. Ruuth, R.J. Spiteri, Implicit-explicit Runge–Kutta methods for time-dependent partial differential equations, Appl. Numer. Math. 25 (2–3) (1997) 151–167.

[60] L. Pareschi, G. Russo, Implicit–explicit Runge–Kutta schemes and applications to hyperbolic systems with relaxation, J. Sci. Comput. 25 (2005) 129–155.

[61] S. Boscarino, F. Filbet, G. Russo, High order semi-implicit schemes for time dependent partial differential equations, J. Sci. Comput. 68 (2016) 975–1001.

[62] W. Boscheri, S. Chiocchetti, I. Peshkov, A cell-centered implicit-explicit Lagrangian scheme for a unified model of nonlinear continuum mechanics on unstructured meshes, J. Comput. Phys. 451 (2022) 110852. https://doi.org/10.1016/j.jcp.2021.110852

[63] S. Chiocchetti, C. Müller, A solver for stiff finite-rate relaxation in Baer–Nunziato two-phase flow models, in: G. Lamanna, S. Tonini, G.E. Cossali, B. Weigand (Eds.), Droplet Interactions and Spray Processes, Springer International Publishing, Cham, 2020, pp. 31–44.

[64] F. Bassi, L. Botti, A. Colombo, A. Ghidoni, F. Massa, Linearly implicit Rosenbrock-type Runge–Kutta schemes applied to the discontinuous Galerkin solution of compressible and incompressible unsteady flows, Comput. Fluids 118 (2015) 305–320. https://doi.org/10.1016/j.compfluid.2015.06.007

[65] G. Puppo, M. Semplice, G. Visconti, Quinpi: integrating conservation laws with CWENO implicit methods, Commun. Appl. Math. Comput. 5 (1) (2023) 343–369. https://doi.org/10.1007/s42967-021-00171-0

[66] S. Boscarino, R. Bürger, P. Mulet, G. Russo, L.M. Villada, Linearly implicit IMEX Runge–Kutta methods for a class of degenerate convection-diffusion problems, SIAM J. Sci. Comput. 37 (2) (2015) B305–B331.

[67] A. Plessier, S. Del Pino, B. Després, Implicit discretization of Lagrangian gas dynamics, ESAIM 57 (2) (2023) 717–743.

[68] S.D. Pino, B. Després, A. Plessier, An implicit well-posed Lagrangian scheme for non viscous compressible fluids in high dimension, 2024. Preprint, https://cea.hal.science/cea-04492829.

[69] R. Abgrall, S. Karni, Computations of compressible multifluids, J. Comput. Phys. 169 (2) (2001) 594–623. https://doi.org/10.1006/jcph.2000.6685

[70] V.V. Rusanov, Calculation of interaction of non–steady shock waves with obstacles, USSR Comput. Math. Math. Phys. 1 (1961) 267–279.

[71] S. Busto, L. Río-Martín, M.E. Vázquez-Cendón, M. Dumbser, A semi-implicit hybrid finite volume/finite element scheme for all Mach number flows on staggered unstructured meshes, Appl. Math. Comput. 402 (2021) 126117. https://doi.org/10.1016/j.amc.2021.126117

[72] T. Barth, P. Frederickson, Higher order solution of the Euler equations on unstructured grids using quadratic reconstruction. https://doi.org/10.2514/6.1990-13

[73] M. Dumbser, M. Käser, Arbitrary high order non-oscillatory finite volume schemes on unstructured meshes for linear hyperbolic systems, J. Comput. Phys. 221 (2007) 693–723.

[74] I. Cravero, G. Puppo, M. Semplice, G. Visconti, CWENO: uniformly accurate reconstructions for balance laws, Math. Comput. 87 (312) (2018) 1689–1719.

[75] C.W. Shu, Essentially Non-Oscillatory and Weighted Essentially Non-Oscillatory Schemes for Hyperbolic Conservation Laws, Technical Report, Institute for Computer Applications in Science and Engineering (ICASE) (1997).

[76] D. Levy, G. Puppo, G. Russo, Central WENO schemes for hyperbolic systems of conservation laws, ESAIM 33 (3) (1999) 547–571.

[77] G.-S. Jiang, C.-W. Shu, Efficient implementation of weighted ENO schemes, J. Comput. Phys. 126 (1) (1996) 202–228. https://doi.org/10.1006/jcph.1996.0130

[78] I. Cravero, M. Semplice, G. Visconti, Optimal definition of the nonlinear weights in multidimensional central WENOZ reconstructions, SIAM J. Numer. Anal. 57 (5) (2019) 2328–2358. https://doi.org/10.1137/18M1228232

[79] M. Dumbser, M. Käser, V.A. Titarev, E.F. Toro, Quadrature-free non-oscillatory finite volume schemes on unstructured meshes for nonlinear hyperbolic systems, J. Comput. Phys. 226 (1) (2007) 204–243. https://doi.org/10.1016/j.jcp.2007.04.004

[80] M. Dumbser, W. Boscheri, M. Semplice, G. Russo, Central weighted ENO schemes for hyperbolic conservation laws on fixed and moving unstructured meshes, SIAM J. Sci. Comput. 39 (6) (2017) A2564–A2591.

[81] P.D. Lax, Weak solutions of nonlinear hyperbolic equations and their numerical computation, Commun. Pure Appl. Math. 7 (1) (1954) 159–193. https://doi.org/10.1002/cpa.3160070112

[82] F. Ducros, F. Laporte, T. Soulères, V. Guinot, P. Moinat, B. Caruelle, High-order fluxes for conservative skew-symmetric-like schemes in structured meshes: application to compressible flows, J. Comput. Phys. 161 (1) (2000) 114–139. https://doi.org/10.1006/jcph.2000.6492

[83] E. Gaburro, W. Boscheri, S. Chiocchetti, M. Ricchiuto, Discontinuous Galerkin schemes for hyperbolic systems in non-conservative variables: quasi-conservative formulation with subcell finite volume corrections, Comput. Methods Appl. Mech. Eng. 431 (2024) 117311. https://doi.org/10.1016/j.cma.2024.117311

[84] M. Crouzeix, Sur les Methodes de Runge–Kutta pour Lapproximations des Problemes Devolution, Springer-Verlag, Berlin, 1976, pp. 206–223.

[85] R. Alexander, Diagonally implicit Runge–Kutta methods for stiff O.D.E.s, J. Numer. Anal. 14 (1977) 1006–1021.

[86] C.A. Kennedy, M.H. Carpenter, Diagonally implicit Runge–Kutta methods for ordinary differential equations. A review, Tech. Memo. NASA/TM-2016-219173 (1954).

[87] C.D. Munz, On Godunov-type schemes for Lagrangian gas dynamics, SIAM J. Numer. Anal. 31 (1) (1994) 17–42. http://www.jstor.org/stable/2158150.

[88] S. Gottlieb, C.-W. Shu, E. Tadmor, Strong stability-preserving high-order time discretization methods, SIAM Rev. 43 (1) (2001) 89–112. https://doi.org/10.1137/S003614450036757X

[89] B. van Leer, Towards the ultimate conservative difference scheme. V. A second-order sequel to Godunov's method, J. Comput. Phys. 32 (1979) 101–136.

[90] A. Kurganov, E. Tadmor, New high-resolution central schemes for nonlinear conservation laws and convection–diffusion equations, J. Comput. Phys. 160 (1) (2000) 241–282. https://doi.org/10.1006/jcph.2000.6459

[91] E.F. Toro, Riemann Solvers and Numerical Methods for Fluid Dynamics. A Practical Introduction, third ed., Springer-Verlag, Berlin, 2009.

[92] V. Casulli, P. Zanolli, Iterative solutions of mildly nonlinear systems, J. Comput. Appl. Math. 236 (16) (2012) 3937–3947. 40 years of numerical analysis: "Is the discrete world an approximation of the continuous one or is it the other way around?", https://doi.org/10.1016/j.cam.2012.02.042

[93] J.J. Quirk, S. Karni, On the Dynamics of a Shock-Bubble Interaction, NASA CR 194978, ICASE Report 94–75 (1994) 241–282.

[94] C. Parés, Numerical methods for nonconservative hyperbolic systems: a theoretical framework, SIAM J. Numer. Anal. 44 (1) (2006) 300–321. https://doi.org/10.1137/050628052

[95] M. Castro, J.M. Gallardo, C. Parés, High order finite volume schemes based on reconstruction of states for solving hyperbolic systems with nonconservative products. applications to shallow-water systems, Math. Comput. 75 (255) (2006) 1103–1134. http://www.jstor.org/stable/4100267.

[96] S. Chiocchetti, M. Dumbser, An exactly curl-free staggered semi-Implicit finite volume scheme for a first order hyperbolic model of viscous two-Phase flows with surface tension, J. Sci. Comput. 94 (1) (2022) 24. https://doi.org/10.1007/s10915-022-02077-2

[97] E. Hairer, S.P. Nørsett, G. Wanner, Solving Ordinary Differential Equations I: Nonstiff Problems, Springer Series in Computational Mathematics, Springer, second revised ed. edition, 1993. https://doi.org/10.1007/978-3-540-78862-1

[98] E. Hairer, G. Wanner, Solving Ordinary Differential Equations II: Stiff and Differential-Algebraic Problems, Springer Series in Computational Mathematics, Springer, second revised ed., 1996. https://doi.org/10.1007/978-3-642-05221-7

[99] A. Ghidoni, F.C. Massa, G. Noventa, S. Rebay, Assessment of an adaptive time integration strategy for a high-order discretization of the unsteady RANS equations, Int. J. Numer. Methods Fluids 94 (12) (2022) 1923–1963. https://doi.org/10.1002/fld.5131

[100] J. Verreault, M.M. van der Voort, Optimization of layered material configuration for shock attenuation, in: 16th ISIEMS International Symposium for the Interaction of the Effects of Munitions with Structures, Destin, Florida, USA, 9–13 November 2015, 2015.

[101] E.I. Zababakhin, Shock waves in layered systems, Zh. Eksp. Teor. Fiz. 49 (1966) 446–448.